This is to certify that the
dissertation entitled

WOOD-CEMENT PARTICLEBOARD: IMPROVED MANUFACTURING, MATERIAL CHARACTERIZATION AND POTENTIAL APPLICATION IN CONCRETE CRASH BARRIERS

presented by

AN GONG

has been accepted towards fulfillment
of the requirements for the

Ph.D. degree in Civil Engineering

P. Hirichandran
Major Professor's Signature

July 21, 2005
Date

WOOD-CEMENT PARTICLEBOARD: IMPROVED MANUFACTURING, MATERIAL CHARACTERIZATION AND POTENTIAL APPLICATION IN CONCRETE CRASH BARRIERS

By

An Gong

A DISSERTATION

Submitted to
Michigan State University
in partial fulfillment of the requirements
for the degree of

DOCTOR OF PHILOSOPHY

Department of Civil and Environmental Engineering

2005

ABSTRACT

WOOD-CEMENT PARTICLEBOARD: IMPROVED MANUFACTURING, MATERIAL CHARACTERIZATION, AND POTENTIAL APPLICATION IN CONCRETE CRASH BARRIERS

By

An Gong

Recycling waste wood into wood composite products is increasingly attractive to reduce environmental problems associated with disposal and promote sustainable development. For use in engineering applications, in addition to developing suitable manufacturing methods, the material and load bearing characteristics of wood-cement particle composites must be thoroughly investigated. This research focuses on wood-cement particleboard (WCPB). An improved manufacturing process that yields superior wood-cement particleboard is developed; material properties required for engineering design are experimentally determined; and the potential application of wood-cement particleboard to enhance the impact characteristics of concrete highway crash barriers is investigated.

A pressure controlled, fully saturated curing process is developed to enhance the bond between wood particles and the cement matrix to produce a superior wood-cement particleboard. The bending, compressive and impact characteristics of wood-cement

particleboard produced using this process are experimentally determined. The optimum cement/wood ratio also is determined.

The experimental results indicate that WCPB is able to absorb a significant amount of energy by undergoing large nonlinear deformations. With the aim of taking advantage of its energy absorbing capability, the potential application of WCPB to enhance the impact characteristics of concrete highway crash barriers is investigated.

Computational simulation is performed using the LS-DYNA finite element analysis code. The FE simulation agrees reasonably well with impact test results obtained in the laboratory. This suggests that the LS-DYNA material models can be effectively applied to model concrete and wood-cement particleboard.

Subsequently, vehicle crash simulations are performed on a concrete crash barrier and a concrete crash barrier with WCPB facades to determine whether WCPB can enhance the impact characteristics. It is found that a flat WCPB facade is too stiff relative to the flexibility of the vehicle bumper system and does not yield a significant reduction in the impact deceleration force on the vehicle. However, a tubular facade made of WCPB yields reasonable reductions in impact force. A triple tube facade appears to yield the best impact characteristics, assures controllable deformations and provides optimal safety to the vehicle occupants.

To my mother

ACKNOWLEGEMENTS

The author would like to thank Professors Ronald Harichandran and Pascal Kamdem for their academic guidance and financial support in seeing the project through to completion. The author would like to thank Professors Rigoberto Burgueño, Zhengfang Zhou and Parviz Soroushian for their academic guidance. Thanks also to Siavosh Ravanbakhsh for his support in laboratory experiments.

TABLE OF CONTENTS

LIST OF TABLES

LIST OF FIGURES

CHAPTER 1

OVERVIEW AND RESEARCH OBJECTIVES

1.1 Wood-Cement Particleboard

Wood-cement particleboard is composed of wood particles, Portland cement (Type I) and water. Besides having higher material strength, good plasticity, good durability and better energy dissipation properties, it also has low cost, is lightweight and simple to manufacture (Kurfiel, 1995; Wolfe, 1996). It has been shown in practice that the wood-cement particleboard has advantages over conventional wood composites.

At present, approximately 10,000 cubic meters of treated wood are removed from service in the United States and Canada every year. This figure is expected to increase in the next decade (Copper, 1993). However, only a small part of this large amount of waste wood is recycled into products, and most of the waste wood is discarded producing a negative effect on the environment. Therefore, recycling waste into wood composite products is highly beneficial.

The tensile strength of wood-cement particleboard (WCPB) is about 3 times higher than normal concrete (Won, 1995, Moslemi and Pfister, 1987) and the compressive strength of WCPB is comparable to that of normal concrete (Blankenhor, 1994; Sorfa, 1984).

Because WCPB has high porosity due to the presence of soft wood particles, it is capable of dissipating much more energy than concrete. The first toughness index of

WCPB for both bending and compression is six times higher than normal concrete (Wolfe, 1996).

WCPB has advantages over conventional resin-bonded wood particle composites with respect to durability and fire resistance. WCPB meets the requirements for fire resistance and durability for outdoor applications (Wolfe, 1999). However, conventional resin-bonded wood particle composites do not meet the requirements of outdoor applications for either durability or fire resistance.

Because WCPB is mainly made from waste wood removed from service, there is no cost for acquiring the raw material, and the manufacturing process for WCPB is quite simple. Use of waste wood to produce WCPB is environmentally friendly and beneficial to society.

Even though WCPB technology was introduced about 40 years ago, it has not been rigorously investigated, especially in North America (Moslemi, 1989). As the use of WCPB material increases in The United States, more effort is being directed to research.

Recent studies (Won, 1995; Wolfe, 1999; Zhou and Kamdem, 2000; Horne, 1997) on wood cement particle composites have focused on manufacturing methods, material properties, durability and potential applications in engineering. The manufacturing method can significantly impact the material properties of wood-cement particleboards. The development of improved methods that yield WCPB with higher strength and stiffness and reduce variability in material properties would be beneficial.

With the increasing applications of wood-cement particleboard in construction

purposes, more and more research has focused on the study of the strength of the composite material and the effect of the cement/wood ratio on its material strength (Zhou and Kamdem, 2000; Eltomation, 2003).

Perhaps of most relevance is the development of new high volume applications for the large amount of waste wood that is generated in the U.S. Successful applications of using wood-cement particle composites as exterior walls in houses (Horne, 1997) and as sound barriers on highways (Wolfe, 1999) have begun a potential bright future for the application of this material in engineering.

At present, WCPB products have been widely used in construction engineering as both structural and nonstructural members (Kurpiel, 1995; Horne, 1997). Because WCPB has energy dissipating properties, it could also have special applications in structures where impact and dynamic load are a design consideration (Wolfe, 1999).

1.2 Concrete Crash Barriers

Highway engineers are facing a significant challenge to improve the impact characteristics of concrete crash barriers to make the roads safer. Concrete crash barriers are used in the longitudinal direction of roads. Because the deflection of concrete barriers during impact is very small, the impact deceleration forces on vehicles impacting them are much higher than those on vehicles impacting other kinds of barriers such as guardrails. Therefore, enhancements to concrete barriers that reduce deceleration forces on impacting vehicles are highly desirable to improve safety for vehicle occupants.

1.3 Research Objectives

The objectives of this research are to:

- Develop a new manufacturing method to improve the engineering properties of wood-cement particleboard.
- Characterize the response of WCPB under bending, compressive and impact loads.
- Assess the applicability of material models available in the LS-DYNA finite element package to simulate impact on WCPB.
- Use finite element simulations to investigate the feasibility of using wood-cement particleboard facades to enhance the impact characteristics of concrete crash barriers.

CHAPTER 2

INTRODUCTION AND LITERATURE REVIEW

2.1 Introduction

Wood cement particle composites have been used in the manufacturing of building materials for more than 60 years (Wolfe, 1997). As a construction material, the composite products have primarily been used as nonstructural members, and applications have mainly been based on the non-structural advantages of the composite: cost effectiveness, resistance to decay and insects, fire resistance, and thermal insulation. In the last decade, the composite has been successfully used for structural members in construction, and research on its material properties and its potential in engineering applications has increased (Kurfiel, 1995; RBAC Newsletter, 2002).

The literature review presented in this chapter focuses mainly on the description of the development of the technology of wood-cement composites, and is followed by some concrete crash barriers and finite element simulation in highway crash barrier engineering.

2.2 History and Development of Wood-Cement Composites

The concept of combining inorganic binders with wood or agricultural biomass can be traced back several thousands of year to ancient ancient time. Incorporating wheat or rice straw with mud to produce bricks has it roots in prehistory. Such inorganic-bonded composites are still used in many parts of the world. Mixing straw with mud

improves workability, impact resistance and reduces fracture development by providing reinforcing fibers (Won, 1995).

The timeline for the development of inorganic-bonded wood composites in modern times is shown in Table 2.1. The term "inorganic-bonded wood composites" generally refers to mineral-bonded wood products where the minerals mainly include magnesite, gypsum and cement.

Table 2.1 Industrial Production of Inorganic-Bonded Wood Composites (Moslemi, 1988)

Year	Production
1900	Magnesite-bonded boards
1905	Gypsum-bonded excelsior board
1915	Magnesite-bonded excelsior board
1915	Cement-bonded excelsior board
1927	Molded wood-cement products
1937	Resin-bonded particleboards
1942	Cement-bonded wood composite panels
1965	Gypsum fiberboards (shredded paper)
1972	Magnesite-bonded wood composite panel
1982	Gypsum particleboard

Wood-cement particle composites are a special type of wood-cement composites. There are three main types of wood-cement composites: (1) wood-wool cement composites (WWCC), (2) wood-fiber cement composites (WFCC) and (3) wood-cement particleboard (WCPB).

The WWCC was first developed in Europe in the 1920s (Moslemi and Hamel, 1989) and it is manufacturated in many countries around the world. The WFCC were developed primarily as a substitute for asbestos-cement and have a history of about 25 to 30 years (Wolfe, 1997). Research in Europe in the 1920s led to the common practice of

using wood chips in cement to make building blocks (Wolfe, 1997). This application is perhaps the origin of WCPB. However, as a product in commercial industry, WCPB was developed in the 1960s. The industry was stimulated in Europe by lumber shortages and in the United States by large quantities of waste softwood from wood manufacturing industries. The technology of making wood cement composites has many similarities to that used to manufacture resin-bonded wood particleboard (Moslemi and Hamel, 1989).

2.3 Environmental Risk of CCA-Treated Wood

Chromated copper arsenate (CCA) is a water-borne preservative containing arsenic, chromium and copper. It is used for the long-term protection of wood against attack by fungi, insects and marine borers. Applying wood preservatives extends the productive life of wood and helps reduce demand for forest resources. Prior to the wood being treated, small cuts are made into the wood surface to help the penetration of the CCA preservative solution. The wood is stacked and loaded into a sealed chamber where the wood's natural moisture is removed by vacuum. Then the chamber is pressurized, forcing the CCA solution into the wood. A vacuum is then used to extract any excess solution. The wood is removed from the chamber and dried (Health Canada, 2003).

Waterborne preservatives today account for the vast majority of chemicals used in building applications. These waterborne chemicals are used in pressure treating only include chromated copper arsenate (CCA), ammoniacal copper zinc arsenate (ACZA), and several others. CCA accounted for 94% of the waterborne chemicals used in 1995. While the primary chemicals in CCA are highly toxic and are regulated as pesticides by the Environmental Protection Agency (EPA), they are bonded quite tightly to the wood

during fixing, so leaching from the wood is minimal under normal usage conditions (EBN, 1997).

There are some important benefits of treating wood with CCA, the most significant of which is increasing the life of wood for outdoor applications. Older preservatives, such as pentachlorophenal and creosote, pose considerable health risk to users of the wood, but new waterborne preservatives, such as CCA, are safer. They are safer in part because the toxins have a strong chemical bond with wood and are fixed in the wood. However, disposing of treated wood at the end of its life has become a serious problem (ENB, 1997).

CCA-treated wood is used primarily for structures intended for outdoor settings and is commonly used in residential construction such as playground structures, fences, gazebos and decks. It is also used for industrial uses such as utility and construction poles, marine timbers and pilings.

In 1993, an estimated 5 billion board feet, or 6.5 million tons, of wood were CCA treated and will be removed from service after approximately 27 years in 2020. This figure does not include the 72 million utility poles or 15 million ties treated annually with creosote or pentachlorophenol or other oilborne preservatives (Stalker, 1993; Mickleright, 1993). A major challenge facing the wood preservative industry today is how to deal with this massive quantity of waste wood in the coming decade.

Based on a 30-year service-life, researchers at the Forest Products Laboratory (FPL) in Madison, Wisconsin estimate that 2.5 billion board feet per year (6 million m^3/year) of treated-wood products (all types of preservative treatments) are currently

entering the solid-waste stream, and that level will increase to 8 billion board feet per year (19 million m^3/yr) by the year 2020 (EBN, 1997).

The environmental hazards of CCA-treated wood are related to the high toxicity of copper, chromium and arsenic to non-target organisms in freshwater and marine environments. The potential risk depends on the exposure, i.e., the amount of CCA being leached from treated wood into the aquatic ecosystem, directly or indirectly. In general, small ground-based structures made from CCA-treated wood that are properly treated and fixed are unlikely to cause any environmental hazard. There is some data that indicates that some sealants can reduce surface dislodgeability and leachability of the preservative chemicals. This data is being considered as part of the CCA reevaluation. The environmental risk of CCA-treated wood coming into contact with freshwater and marine environments (including wetlands) is greater than in terrestrial environments and possible restrictions on aquatic use are currently being assessed.

Recently, the U.S. Consumer Product Safety Commission (CPSC) released a risk assessment of CCA-treated wood on playground structures. This assessment concluded that children playing on playground equipment built with CCA-treated wood might have a slightly increased risk of developing cancer. However, at this time, no further action has been recommended by the CPSC (Health Canada, 2003).

For the general public, on the one hand, disposal in landfills may produce environmental problems. It is increasingly difficult to dispose solid wood in landfills because it is a high volume material and deterioration is questionable when necessary requirements for biodegradation are not met. On the other hand, Stalker (1993) reported a quoted cost by landfill operators of $150 US per utility pole. The cost of disposal and

the current level of environmental awareness will reduce land filling as an attractive alternative for disposal of treated wood (Cooper, 1994; Marer and Grimes, 1992).

In addition, CCA-treated wood should never be burned because the heavy metals in CCA are not destroyed; the chromium and copper become concentrated in the ash, while the arsenic becomes a vapor that will escapes into air (ENB, 1997). NBC10.com (2003) reported that a single 12-foot, 2 (in.) x 6 (in.) piece of lumber contains about 27 grams of arsenic – enough to kill 250 adults. Burning CCA releases the strong chemical bond that holds the arsenic bound to the wood.

As a result, the disposal of preservative-treated wood products removed from service is problematic. Therefore an attractive solution for the after service disposal of treated wood is reconstituted wood products. Recycled treated wood or urban wood, if properly managed, can be a good source of lumber or of fiber for engineered wood products such as hardboard, fiberboard, particleboard and cement-bonded particleboard. Recycling waste into wood composite products becomes increasingly attractive because it not only benefits the environment but also has economic value.

2.4 Wood and Cement

2.4.1 Wood

Wood is divided into two broad classes, usually refered to as "hardwood" and "softwood". Needle-like leaves characterize softwood trees. Such trees are known commonly as evergreens. In contrast, hardwood trees have broad leaves, which generally change color and drop in the fall in cold climatic zones.

Hardwood species grow in every major region of the United States. On the worldwide basis, hardwood is dominant. They are found in most areas of the world

(Table 2.2). In total, hardwood growing stock has been estimated to exist in volumes almost double that of softwoods. However, North America and the former USSR softwood are dominant in total volume.

Table 2.2 Area of Forestland in the World by Geographic Location and Species Group–1980 (Haygreen, 1989)

Area	Total	Softwoods	Hardwoods
		(thousand ha)	
North America	807,092	533,075	274,017
Latin America	915,019	20,474	894,545
Europe	158,902	97,989	60,913
Africa	743,713	13,891	729,822
Asia	468,230	102,238	365,992
USSR	928,600	679,900	248,700
Pacific area	298,947	15,995	282,952
World	4,320,503	1,463,562	2,856,941

Source: FAO (1985).

Wood is composed principally of carbon, hydrogen, and oxygen. Table 2.3 shows the chemical composition of a typical North American wood and shows carbon to be the dominant element on a weight basis.

Table 2.3 Elemental Composition of Wood (Haygreen, 1989)

Element	Percent of Dry Weight
Carbon	49
Hydrogen	6
Oxygen	44
Nitrogen	slight amounts
Ash	0.1

The elemental constituents of wood are combined into a number of organic polymers: cellulose, hemicellulose, and ligin. Table 2.4 shows the aproximate percent of dry weight of each in hardwood and softwood.

Table 2.4 Organic Constituents of Wood (Haygreen, 1989)

Wood Type	Cellulose	Hemicellulose (% dry weight)	Lignin
Hardwood	40-44	15-35	18-25
Softwood	40-44	20-32	25-35

Softwoods have a uniform arrangement of a few cell types and therefore usally do not have a distinctive appearance. Hardwoods, on the other hand, are composed of widely varying proportions of markedly different kinds of cells and thus often have a unique appearance. The physical differences between hardwood and softwood are listed in Table 2.5. Figure 2.1 and Figure 2.2 show the cell types of softwood and hardwood.

Table 2.5 Physical Differences Between Hardwood and Softwood (Haygreen, 1989)

Hardwood	Softwood
Many types of cells	few types of cells
Contain vessels	no vessels
Wide rays (30% of wood volume)	narrow rays (5-7% of wood volume)
Not aligned in straight radial rows	Straight radial rowsof cells

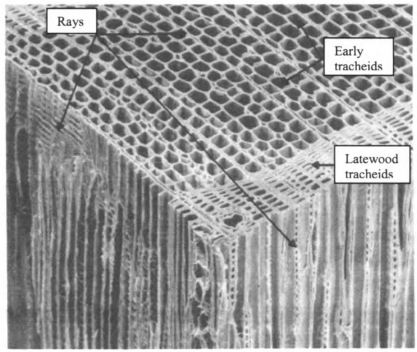

Figure 2.1 Softwood: Sitka sprue (× 75), (Haygreen, 1989)

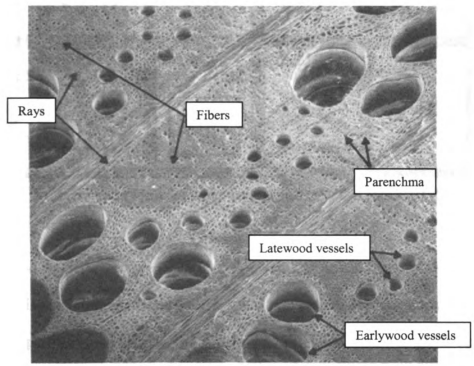

Figure 2.2 Hardwood: Red oak (× 50), (Haygreen, 1989)

(Scaning electron micrograph by Josefina Gonzalez, Forintek Canada Corp. Vancouver, B.C.)

Currently, the wood used in wood-cement composites are generally from softwood. Figure 2.3 (Marra, 1972) shows the various sizes and shapes of wood elements included in wood composites. For wood-cement composites, the wood materials in the second and third rows in Figure 2.3 are generally used.

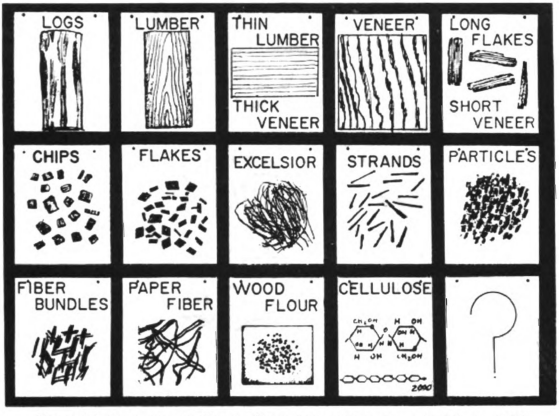

Figure 2.3 Most common forms of wood composites elements (Marra, 1972)

The wood particles are produced by a special cutting machine. A variety of machines including refiners, hammers, flakers, and waferizers can be used to produce the type of furnish (particles used to make the board) desired. These machines grind, cut, or tear the wood into a range of particle sizes. Figure 2.4 illustrate the parts of a ring flaker.

This machine has knives that cut thin particles from whatever kind of wood is fed to it. A general disk refiner is shown in Figure 2.5 and is used to prepare small fiberlike particles.

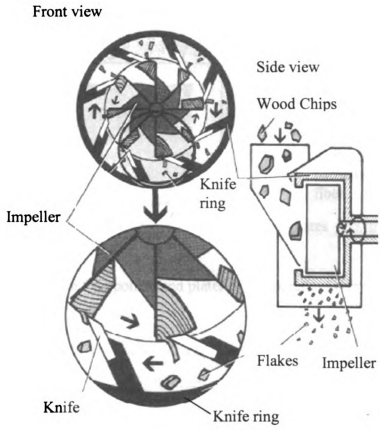

Figure 2.4 Element of a knife-ring flaker (Haygreen, 1989)

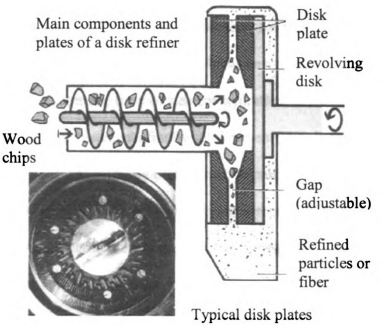

Figure 2.5 Main Component and plates of a disk refiner (Haygreen, 1989)

2.4.2 Cement

An inorganic binder which has found commercial use in the field of certain wood particle panels is Portland cement. This binder is used in the manufacture of products intended for service in structural applications which may or may not be load bearing. Portland cement contains four basic chemical elements, silicon, aluminum, iron, and calcium, usually in oxidized forms (Moslemi, 1974).

Portland cement is a gray powder that consists of angular particles typically in the size range of 1 to 50 μm. It is produced by pulverizing a clinker with calcium sulfate. The clinker is a heterogeneous mixture of several minerals produced by high-temperature reactions between calcium oxide and silica, alumina, and iron oxide. When Portland

cement is dispersed in water, the calcium sulfate and the high-temperature compounds of calcium go into solution, and the liquid phase becomes rapidly saturated with various ionic species. As a result of combinations between calcium, sulfate, aluminate, and hydroxyl ions within a certain time of cement hydration, different crystals of calcium chemical compounds are created and finally solid cement paste is formed.

Portland cement was formally used in manufacturing wood cement composites in 1928 (Maloney, 1977). Nowadays, in wood cement composites, Portland cement (Type I) is generally used as a binder in the wood cement composites.

2.4.3 Wood cement compatibility

In wood-cement composites, the compatibility between wood and cement is a major concern. Wood species are not compatible with cement because soluble carbohydrates and certain extracts in the wood inhibit the setting and hardening of cement. In fact, in some instances, the influence of such substances is so severe that the cement binder is inhibited from setting at all regardless of the amount of time allowed. This inhibitory effect appears to be more pronounced in hardwood compared to softwoods due to the existence of the type of constituents that retard or prohibit element setting (Moslemi, 1974).

To reduce the inhibitory effects of wood on cement setting, various measures have been taken. One of these consists of extracting sugars and other water soluble materials with hot water. The wood particles are soaked in hot water for a period of time. The soak duration depends on a number of factors such as the temperature of the hot water and the amount of inhibitory extractives present. The addition of various chemical

additives also have been found useful in reducing setting time. A major compound used in this connection is calcium chloride. Clare (1956) states that calcium chloride solutions of 1 – 3 percent are necessary to neutralize the effect of 0.1 percent sugar in the soil cement mixtures. Further increases in the level of calcium chloride, however, have been found to reduce strength in such mixtures.

Miller (1987) studied the effects of carbohydates on the tensile strength and hydration characteristics of Portland cement. He concluded that sugars and other compounds in wood are detrimental to cement hydration and strength. When wood is mixed with cement, the setting time of cement increases and the cement strength decreases. However, if wood particles are treated with special chemicals, the compatibility between wood and cement may be dramatically improved.

Several studies have suggested that mechanical properties of wood based composites made of CCA treated fiber or particles are lower than those of untreated furnish (Vicks, 1990; Gertjejansen et al., 1988; Suzuki, 1993). The reduction in mechanical and physical properties was attributed to the surface modification of the woody materials by preservative treatment or the interaction between the preservatives and the resin. However, for cement-bonded particleboard, Schmidt et al. (1994) reported that CCA treated red pine particles produced strong wood-cement composites compared to untreated wood. Generally the CCA treated wood has a better compatibility with cement, while, untreated wood has a poor compatibility with cement during cement hydration.

Most wood waste generated by manufacturing industries is treated with CCA. Consequently, in present-day wood-cement particleboard, the wood particles are

generally made from wood treated with CCA. Previous studies indicate that CCA-treated wood has improved compatibility with cement (Schmidt, 1994; Hsu, 1994).

2.5 Bending Strength of Wood-Cement Particleboard

Most previous research on the mechanical characteristics of wood-cement composites has focused on bending strength. Through bending tests, the modulus of rupture (MOR) and modulus of elasticity (MOE) are investigated. In general, the MOR is the primary measure of the quality of wood-cement particleboard.

Wolfe (1997) reported that the maximum MOR of wood-cement particleboard is typically less than 10 MPa.

2.5.1 Elasto-degrading plastic behavior

In general, wood-cement particleboard displays an elasto-degrading plastic behavior under flexural loadings due to the bridging action of wood particles (Wolfe, 1999). Figure 2.6 shows the characteristics of the load-deformation curve of wood-cement particleboard under a three-point bending test. The response is elastic until the first crack forms, then displays a reduction in stiffness until the peak load. The load carrying capability degrades after the peak load but large deformations are sustained before failure.

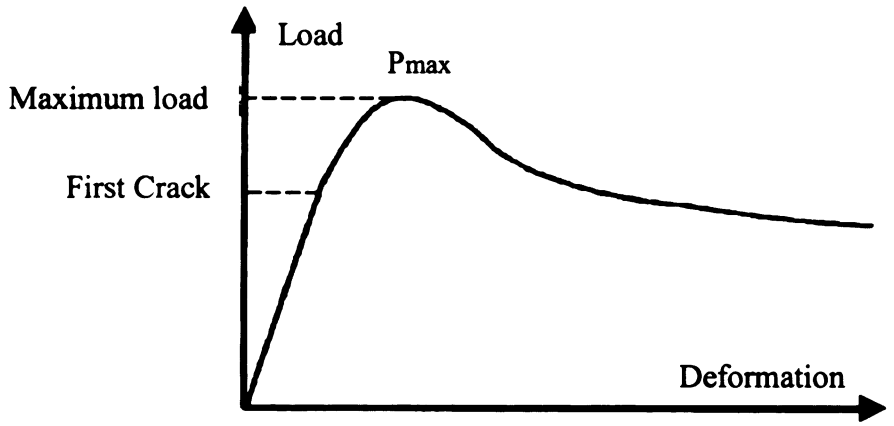

Figure 2.6. Typical load-deformation curve of wood-cement particleboard under bending (Wolfe, 1999)

Won (1995) reported that the load-deflection curves of WCPB under bending loads show elasto-plastic behavior both for specimens cured in air and those with accelerated curing using CO_2. Figure 2.7 shows typical flexural stress-deflection curves.

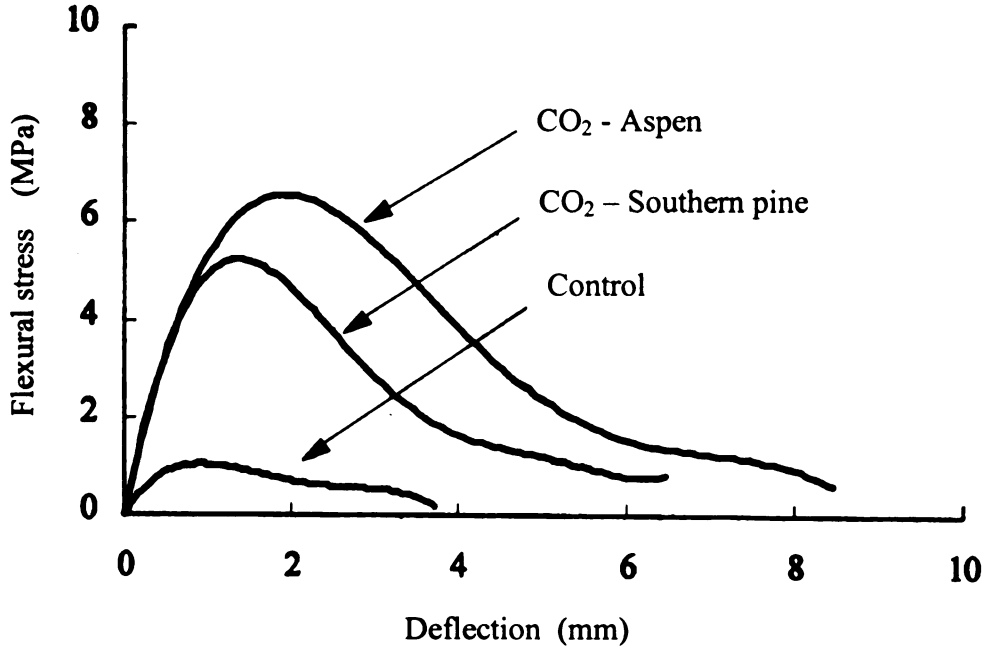

(a) Wood/cement Ratio = 0.28 (Cement/wood ratio = 3.57)

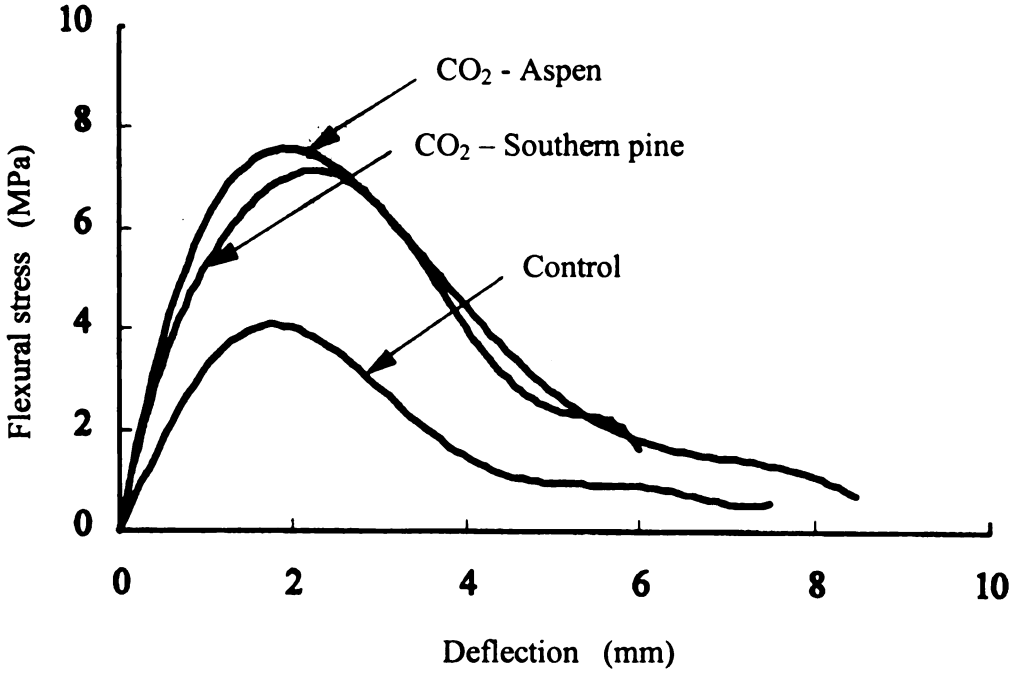

(b) Wood/cement Ratio = 0.35 (Cement/wood ratio = 2.86)

Figure 2.7 Flexural stress vs. deflection curves for WCPB with normal and accelerated curing (Won, 1995)

2.5.2 Effect of cement/wood ratio

The cement/wood ratio is an important parameter in the manufacturing of wood-cement particleboard because it impacts the weight to strength ratio and the cost. At present, commercially manufactured boards are produced in the range of 2.75 to 3.0 parts of cement to 1.0 part of wood (Bison and Creten, 1977).

Prestemon (1976) indicated that WCPB had higher bending strength properties when the cement/wood ratio was increased from 0.75 to 1.5.

Moslemi and Pfister (1987) reported that the MOR of wood-cement flakeboard increased as the cement/wood ratio was lowered from 3.0 to 1.5. In their study, the wood particles were wood flakes with a thickness of 0.56 mm and length and width from 12 to 25 mm. They used Portland cement types III and I. Their test results are summarized in Figure 2.8.

Lee (1985) reported that an increase of the cement/wood ratios above 2.0 had an adverse effect on bending stiffness and strength of wood excelsior board.

Oyagade (1990) conducted bending tests with cement/wood ratios of 1.55, 2.33 and 3.10. This study indicated that at a constant board density, a decrease in cement/wood ratio generally improved the bending properties.

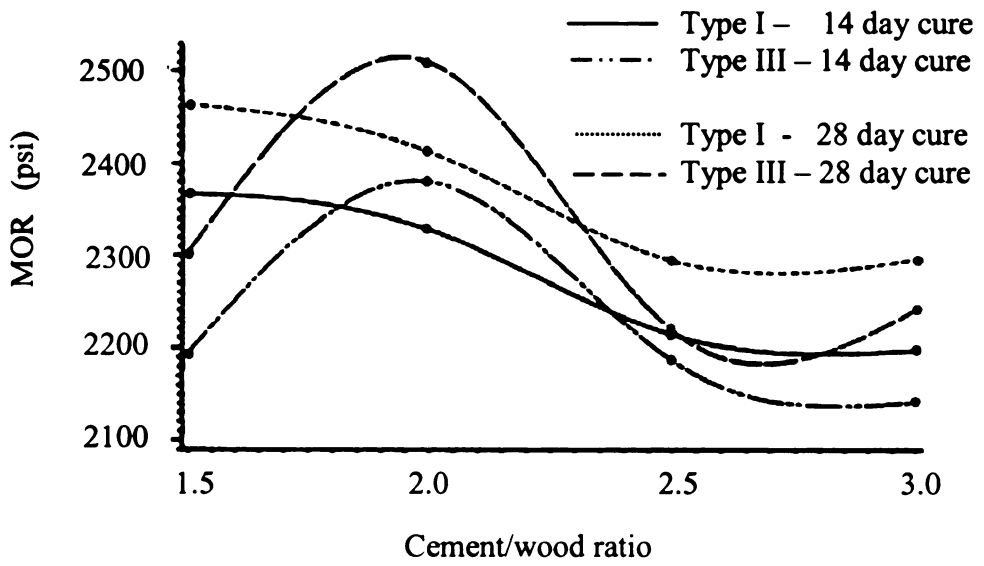

Figure 2.8. Variation of MOR with cement-wood ratio

(Moslemi and Pfister, 1987)

2.5.3 Effect of manufacturing method on strength

The manufacturing method for WCPB is being continually improved. Different manufacturing methods can lead to significant changes in the material properties of WCBP, such as strength and durability. The following two major of manufacturing methods are general used for WCPB:

a. Thickness control and laboratory curing at 65 % relative humidity.

b. Thickness control and CO_2 accelerated curing.

Thickness control means that the specimen is manufactured to a predetermined thickness by pressing specimens in a hydraulic press.

Laboratory curing is the most common curing method. In this method, specimens are cured at a temperature of 20 °C and 65% relative humidity for 28 days after they are removed from the press.

In the accelerated CO_2 curing method, after a few hours of setting under pressure, the specimens are steamed with CO_2 for 5 to 8 hours for accelerated curing. This method dramatically shortens the manufacturing period.

Won (1995) reported that the bending strength of wood cement particleboard cured with CO_2 is much higher than those cured in air. Figure 2.7 shows the differences in flexural stress between CO_2-cured and air-cured (control) specimens.

Zhou and Kamdem (2001) reported that air curing at 20C° and 100% relative humidity for 28 days produced specimens with higher bending strength than those cured at 65 % relative humidity.

2.6 Compressive Strength of Wood-Cement Particle Composites

Studies on the compressive strength of WCPB have been much fewer than those on flexural strength. With the application of wood-cement particle bricks in loading bearing walls, the compressive strength has recently received more attention.

Wolfe (1997 and 1999) reported that the characteristics of the compressive load-deformation curve are similar to those for the bending test shown in Figure 2.6. In his study, the load displacement plots exhibited linear behavior up to 60 to 75% of the maximum load, at which point the rigid cement matrix began to crack. As the material began to fail, the material exhibited plastic behavior.

Research on hardwood-cement particle composites (Blankenhor, 1994) indicated that as the amount of red maple and hardwood pulp increased, the compressive strength decreased. Figure 2.9 shows the compressive test results.

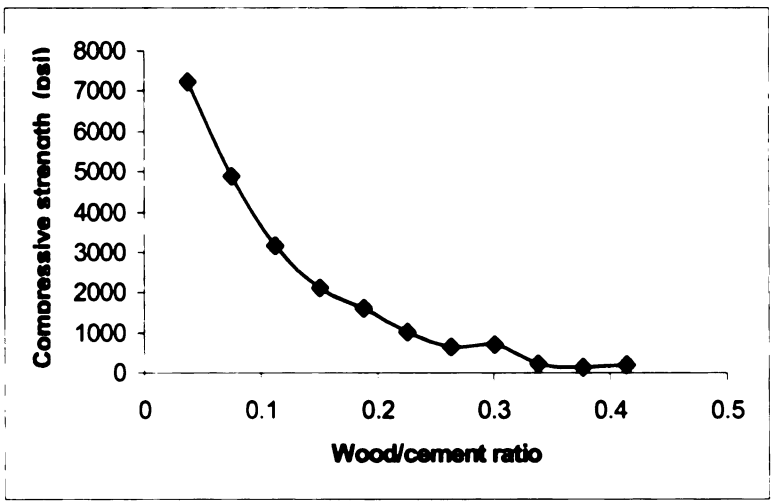

Figure 2.9. Compressive strength vs. wood/cement ratio (Blankenhor, 1994)

Sorfa (1984) reported that WCPB bricks developed for use as supports in mines exhibited compression properties similar to those of wood loaded perpendicular to the grain. The load-deformation curves were initially linear until matrix cracking, after which they softened (Figure 2.10).

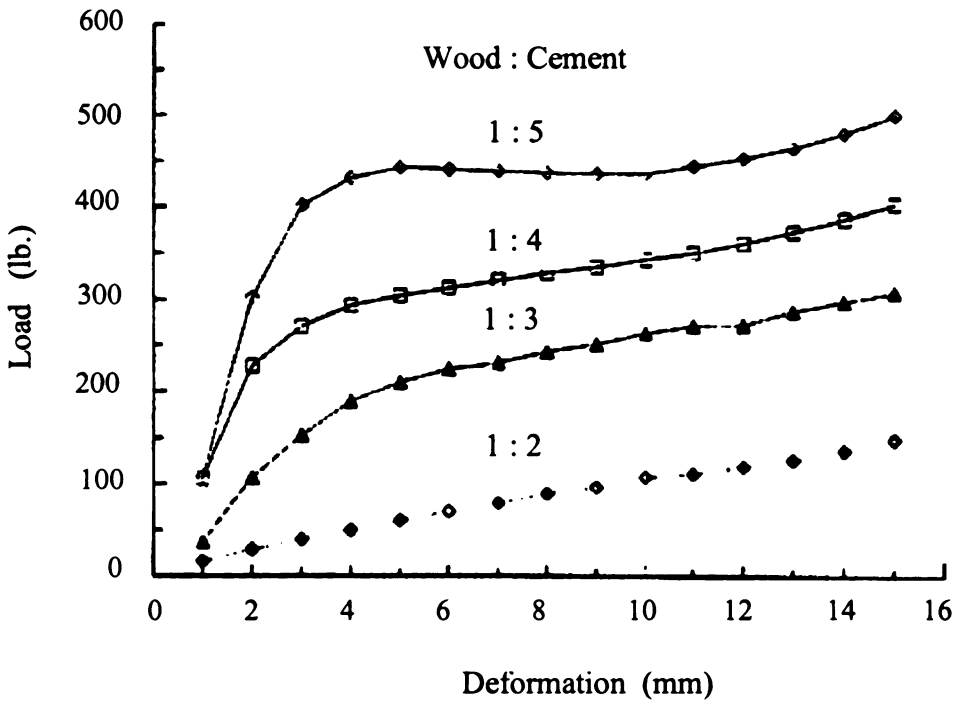

Figure 2.10. Compressive load vs. deformation for WCP bricks (Sorfa, 1984)

2.7 Durability

The major advantage of WCPB over resin bonded wood particleboard is that WCPB can be used for either indoor or outdoor applications, while resin bonded wood particleboard can only be used as interior material because it is sensitive to moisture and susceptible to damage by fire and insects.

Won (1995) conducted flexural tests on WCPB subjected to 25 cycles of accelerated wetting-drying. He found that in general, repeated wetting-drying cycles led to increased stiffness and reduced toughness of WCPB, and the effects on flexural strength were mixed. Figure 2.11 shows the wetting-drying test results.

Won (1995) also reported that repeated freezing-thawing cycles led to increased stiffness and reduced toughness values, and the effects on flexural strength were mixed. Figure 2.12 shows the freezing-thawing test results.

Wolfe (1999) reported that freezing-thawing tests on the wood-cement particleboard support the premise that these composites can be designed to meet the durability requirements for highway sound barriers.

Simatupang (1990) studied the durability of conventional (air curing) and rapidly curing (using CO2) cement-bonded wood particleboard. He concluded that conventionally made cement-bonded wood particleboards have higher bending strength and are also more durable. However, the properties of the rapidly setting boards fulfill the requirements of existing standards.

Dinwoodies (1991) and Karam (1992) demonstrated that wood-cement particleboard could be fabricated to resist cyclic moisture and temperature effects.

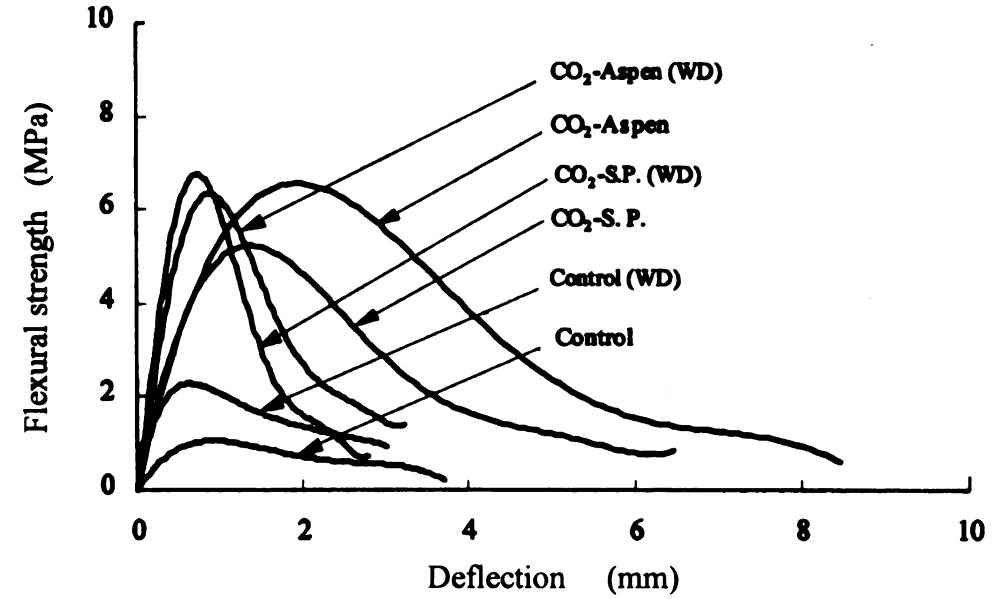

Figure 2.11 Flexural strength vs. deflection under wetting and drying for wood/cement ratio of 0.28 (Won, 1995)

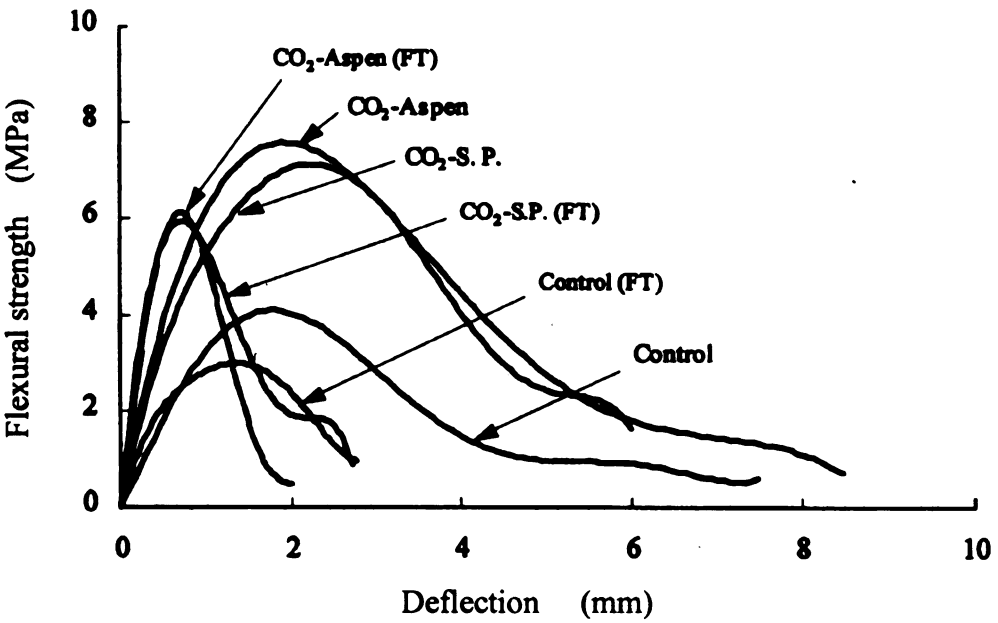

Figure 2.12 Flexural strength vs. deflection under freezing and thawing for wood/cement = 0.28 (Won, 1995)

2.8 Insulation Properties

Wood cement composites provide very good insulation, both thermally and acoustically. The advantageous insulation properties make these composites attractive for building applications.

2.8.1 Thermal properties

The thermal property of composite materials is generally related to the porosity of the composites. Composites with higher porosity usually have higher thermal resistance. Because of its relatively low density, wood-cement particleboard has good thermal properties. As reported by Eltomation Corporation (2003), the thermal resistance R-value for 2.5 cm thick wood-wool cement boards is 5. The R-value is the resistance of one square meter of the material subject to a one degree temperature difference. The equation of thermal resistance R-value can be expressed as:

$$R = \frac{A\Delta T}{W} \tag{2.1}$$

where R is the thermal resistance value in units of m^2k/W , A is the surface area of the heat flows in units of square meter, $\triangle T$ is temperature difference between the warm and cold sides of the material, and W is the resultant heat flow in units of Watt.

Southern pine excelsior cement board with a thickness of 5 cm has an R-value of 4.0 (Concrete Products, 1984). Lee (1985) reported that wood excelsior cement board with a thickness of 5 cm has an R-value (thermal resistance) of 3.5. Lee (1985) concluded that the thermal conductivity or thermal resistant value is related to the density of the board and the density of the wood. For a given density of the board, lower density wood aggregate yields aboard with higher thermal resistance.

2.8.2 Acoustic properties

Wood-cement composites are considered to have good sound absorption ability. Wolfe (1997) reported that natural fiber cement composites have good sound absorption properties, and can be used to reduce noise. Wolfe (1999) reported that the Wisconsin DOT has used WCPB for highway sound barriers.

Neithalath (2003) reported an experimental test on the acoustic performance of wood fiber cement composites. The test results indicate that wood fiber cement composites have a strong potential for absorbing sound. He further concluded that the sound absorption coefficient of the wood fiber-cement composites increases with an increase of wood fiber volume due to the generation of an increased number of porous channels by wood fibers in the cement matrix.

Eltomation, the world's largest wood-cement composites supplier, reported the following sound absorption data for wood-wool cement boards (Eltomation, 2003):

- Resistance of a plastered wall of 5 cm wood wool cement boards is 36-40 decibel.
- Resistance of a plastered double wall with air space between WWCBs is 53-57 decibel.
- Noise reduction coefficient for a 2.5 cm thick board is 0.7.

In comparison, the acoustic resistance of a permanent shuttered wall with 12 cm concrete core is 54-56 decibel.

2.8.3 Fire resistance

According to Eltomation (2003) a 5 cm thick wood-wool cement board has a 1-hour fire resistance and a 10 cm thick board has a 2-hour fire resistance. Kurfiel and

Moslemi (1995) reported that wood cement particleboard is in a class A fire rating. To have a class A fire rating, a material should be able to withstand severe exposure to fire.

2.9 Theoretical Studies

Information concerning theoretical treatment of the behavior of cement-bonded wood composites is very limited. Linear elastic fracture mechanics, the discipline concerned with failure by crack initiation and propagation, is often used to evaluate the failure mechanism in fiber reinforced concrete material. Fiber bridging is generally accepted as the enhancing mechanism in wood-cement composites. Figure 2.13 shows a schematic representation of a cross section through a fiber-reinforced matrix. The diagram shows several possible failure modes occurring before fracture of the composites. In the high stress region near the crack tip, fibers may debond from the matrix (fiber 1). Also, sufficient stress may be transferred to a fiber (fiber 2) to ultimately fracture the fiber (fiber 4). When total debonding occurs, the debonded fiber can then be pulled out from the matrix and considerable energy is absorbed by the system in the form of frictional energy (fiber 3). It is also possible for a fiber to be left intact as the crack propagates. This process is called bridging action.

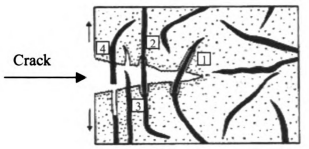

Figure 2.13 Schematic representation of cracking through a fiber reinforced matrix (Coutts, 1986)

Different theoretical approaches have been used to predict the strength of WCPB. Dinwoodie and Paxton (1988), Sorfa (1984) and Wolfe (1999) qualitatively related strength to density. Sarja (1988) presented the following empirical formulae for the modulus of elasticity, modulus of rupture and compressive strength of cement-bonded particleboard as a function of density:

$$\begin{aligned} f_c &= 4.5(\rho/1000) \\ f_{ct} &= \rho/500 \\ E_c &= 1500(\rho/1000)^4 \end{aligned} \tag{2.2}$$

where ρ = density at 40% humidity in kg/m^3

f_c = compressive strength in MPa

f_{ct} = tensile strength in MPa

E_c = modulus of elasticity in MPa

The composite mechanics approach has been used by several researchers (Laws, 1983; Balaguru, 1992; Bodig, 1982) in the form of 'rule of mixtures'. The rule of mixture stated in its most general form is:

$$\sigma_c = \sigma_m V_m + \sigma_f V_f \tag{2.3}$$

where σ_c is the strength of the composite, σ_m is the strength of the matrix, σ_f is the strength of the fibers, V_m is the volume fraction of the matrix, the V_f is the volume fraction of the fibers.

Similarly, for the modulus of elasticity in tension, E_c, the rule of mixture is written as:

$$E_c = E_m(1 - V_0)V_m + \eta E_f V_f \tag{2.4}$$

Where E_c, E_m and E_f are the modulus of elasticity of composite, matrix and fiber, respectively.

The rule of mixtures assumes that there is no effect from Poisson's ratio and that fibers are fully bonded to the matrix before the composite cracks, i.e. equal strain in fiber and matrix.

2.10 Applications of Wood-Cement Composites

The development and use of wood-cement particle composites attest to their suitability as construction materials. Wood-cement composites have been successfully used as roofing, cladding, interior wall, exterior wall, highway sound barriers, etc.

The photos in Figures 2.14 to 2.25 show applications of wood-cement composites (including particleboard, strand board and wood-wool board) in building construction.

Figure 2.14 Siding with WCPB in Japan

(Eltomation Company)

Figure 2.15 Siding with WWCB in the Phillipines

(Milligan, 2004)

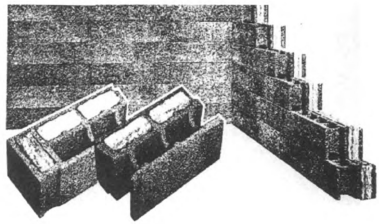

Figure 2.16a WCP Block for building walls (Hoene, 1997)

Figure 2.16b Exterior and interior walls with WCP blocks (Hoene, 1997)

Figure 2.17 Sound barrier of wood-cement particleboard in Czech Republic

(CETRIS, 2005)

Figure 2.18 Wood-wool cement board for roofing and walls in Phillippines

(Eltomation Company)

Figure 2.19 Wood strand cement board for all walls and sidings in Japan

(Eltomation Company)

Figure 2.20 Roof decking with wood excelsior cement composites (Moslemi, 1974)

Figure 2.21 Wood fiber cement board as exterior-wall cladding of the Sandoz Laboratory in Basel, Switzerland, (Deppe, 1974).

2.11 Highway Barriers

2.11.1 Introduction

At a number of locations on existing highways there are physical conditions that cannot be readily modified to eliminate or minimize the hazard they present to out-of-control vehicles. These include brigde piers, abutments, and parapet noses; heavy, nonbreakway sign supports; and high embankment slopes. At these locations, barriers are used to reduce the hazard.

The term "barriers" refers to longitudinal barriers and crash cushions. Longitudinal barriers function primarily by containing and redirecting errant vehicles. Crash cushions function primarily by decelerating errant vehicles to a stop or by redirection.

Longitudinal barriers, including bridge railings, are generally denoted as one of three types: (a) flexible, (b) semi-rigid and (c) rigid. Figures 2.22 to 2.24 show three types of longitudinal barriers.

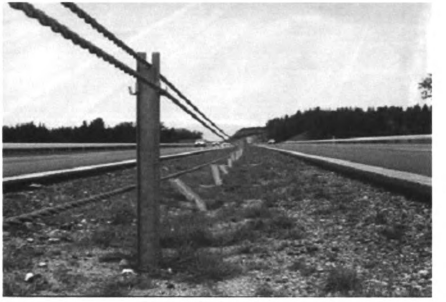

Figure 2.22 Flexible cable barrier

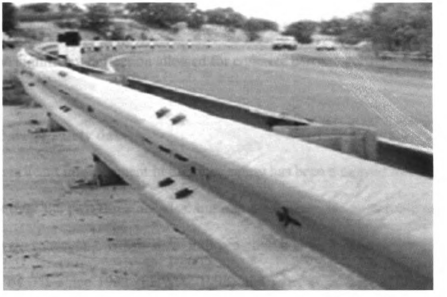

Figure 2.23 Semi-rigid guardrail

Figure 2.24 Rigid concrete barrier

Flexible barriers generally consist of cable barriers, which are primarily designed to contain the crashing vehicle by deforming a large amount rather than redirecting a vehicle. These are generally used in local roads. Semi-rigid barriers are usually guardrails, which are required to contain and redirect vehicles in major highways. The guardrail is allowed to have a certain amount of deflection during vehicle impact. Rigid barriers are concrete barriers required to contain and redirect vehicles in major highways. There is no significant deflection allowed for concrete barriers during vehicle impact.

2.11.2 Barrier safety data

Significant improvement in highway safety has been achieved through a multitude of actions over the past three decades, but one area where serious problems still exist is the highway roadside. Crash data indicate that highway fatalities nationwide have increased by 7% since 1992 (FHWA, 1998) and more than 40% of highway fatalities involve vehicles hitting objects on the roadside, including concrete barriers. Data from

the U.S. Department of Transportation's Fatality Analysis Reporting System, and the Insurance Institute for Highway Safety (Roadside hazards, 2001) provide the following facts:

- 12,311 people died in roadside hazard crashes in 2000, 2% more than in 1999 and about 12% more than in 1975.
- 96% of roadside hazard crash deaths in 2000 occurred in single-vehicle crashes.
- The percent of single vehicle roadside hazard crash deaths involving rollover, in 2000 (Roadside hazards, 2001) is tabulated in Table 2.6.

Table 2.6 Rate of crash death on vehicle-barrier crash

Barrier Type	Rate of Crash Death
Bridge Rail	41%
Guardrail	50%
Concrete /other barrier	41%

The accident data shows that a large number of deaths occur as a result of vehicles impacting concrete barriers. Therefore, enhancing the impact characteristics of concrete barriers can be benificial to the motoring public.

2.11.3 Crash performance of concrete barriers

Concrete Median Barriers are widely used structures on the roadways of North America. The design of concrete median barriers has been evolving since 1950's (Marine, M. C., 1999). As a crash safety device, concrete median barriers play an important role to contain and redirect crashing vehicle. Numerous crash test research programs on concrete median barriers have been conducted from late 1960's through

early 1990's (Marine, M. C., 1999). The concrete barrier's shape plays an important role in vehicle-barrier crashes. In general, there are three major types of concrete barriers with different shapes (Figure 2.25): 1) New Jersey (NJ) shape concrete barriers, 2) constant slope concrete barriers, and 3) vertical concrete parapets.

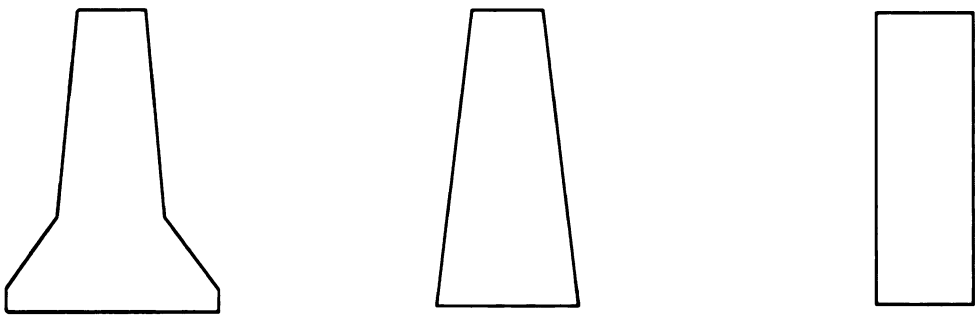

a. NJ Shape Barrier b. Constant slope barrier c. Vertical concrete parapet

Figure 2.25 Major shapes of concrete barriers

For NJ shape concrete barriers, when a vehicle's front bumper impacts the lower sloped face and slides upwards, the vehicle is lifted and part of the kinetic energy is converted to potential energy. This potential energy is converted back into kinetic energy as the vehicle returns to the ground.

Vertical concrete parapet walls do not have the energy management feature of the NJ barrier, but crash tests have demonstrated that they can perform adequately (McDevitt, 2002). All of the energy absorption in an impact with a rigid vertical wall is due to crushing of the vehicle. Bumpers usually do not slide up vertical concrete walls and lift the vehicle and all four wheels tend to stay on the ground. This minimizes the potential for vehicle rollover (McDevitt, 2002).

On March 22, 1990, the Texas Transportation Institute conducted a field crash test of a vehicle crashing onto a portable concrete barrier. The vehicle was a Honda Civic (820C), and the barrier was a longitudinal concrete temporary barrier. Figures 2.26 to 2.27 show the barrier's geometry, plan view of the field test demonstration. This field test indicated that the New Jersey shape barrier successfully contained and redirected the crashing vehicle.

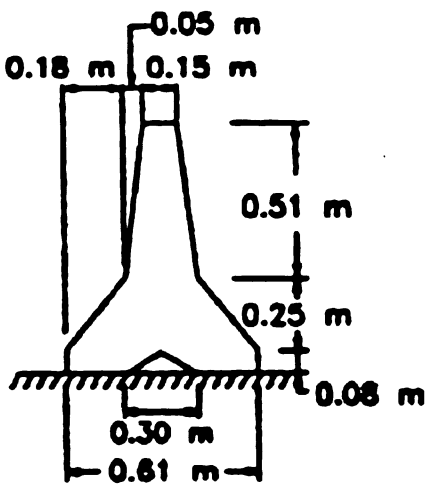

Figure 2.26 Geometry of concrete barrier (NCHRP350 Report, 1993)

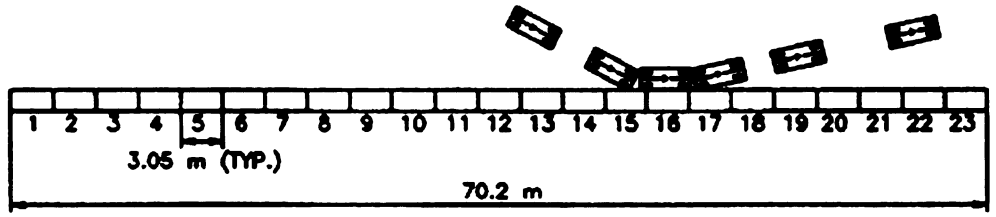

Figure 2.27 Demonstration of field test -plan view (NCHRP350 Report, 1993)

2.12 Concrete Material Model

The response of a reinforced concrete structure, such as concrete crash barrier, is partly determined by the material response of the plain concrete of which it is composed. Therefore, analysis of structural behavior to static or dynamic loading requires prediction of the concrete response to load histories. The fundamental characteristics of concrete behavior are based on the results of experimental testing of plain concrete specimens under specific, relatively simple loading histories. Elasticity and plasticity theories provide a framework for establishing a material model that describes these fundamental characteristics. Experimental data provide additional information for validating and calibrating the material model.

2.12.1 Biaxial and Triaxial Behavior

There is a large amount of research that has been done on the behavior of concrete under biaxial loading. The biaxial strength envelope of concrete obtained by Kupfer et al. is quite famous. Kupfer *et al.* (1969) conducted a series of tests to investigate the response of plain concrete subjected to two-dimensional loading. In the investigation, concrete plates (approximately 200 mm by 200 mm by 50 mm in dimension) were loaded to failure at prescribed ratios of σ_1:σ_2 with σ_3 equal to zero (where σ_i is the *ith* principal stress). Two directional loads were applied using steel brushes to minimize stresses induced through friction at the specimen boundaries. The failure surfaces obtained through the testing are presented in Figure 2.28.

Tasuji et al. (1978) also conducted a series of biaxial tests on concrete. They obtained a strength envelope similar to that reported Kupfer (1969). In addition to the failure surface, they also obtained the concrete's elastic limit surface. Both surfaces are shown in Figure 2.29. The elastic limit surface has a shape similar to but smaller than the failure surface.

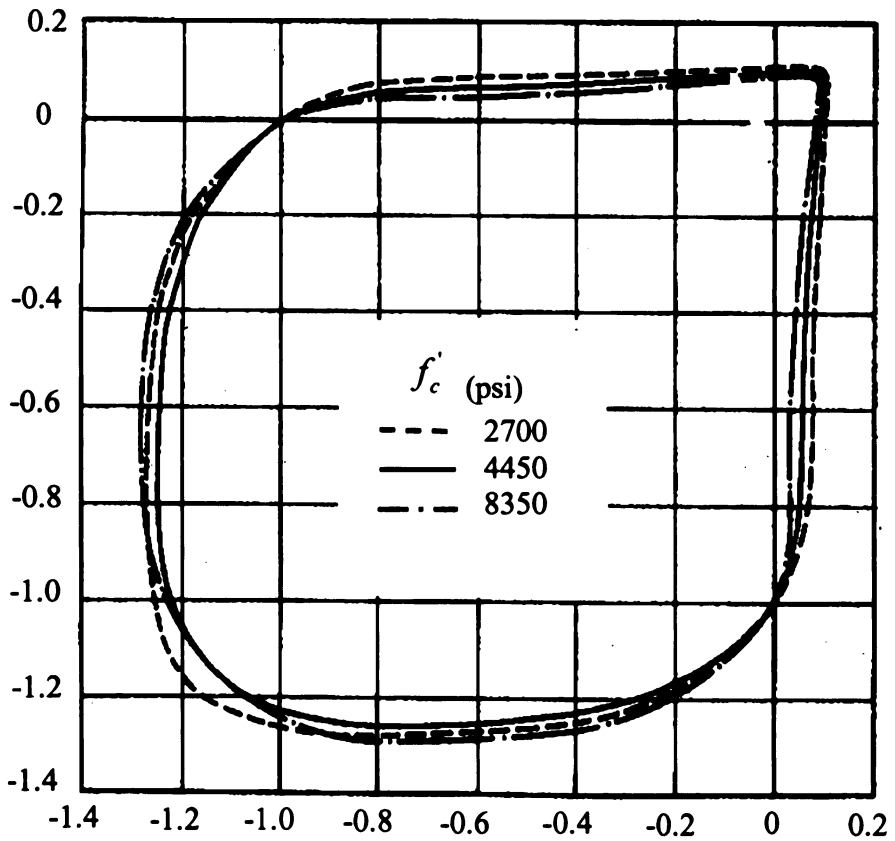

Figure 2.28 Biaxial strength envelope of concrete (Kupfer et al., 1969)

As shown in Figure 2.29, the maximum strength increases under a biaxial compression state. A maximum strength increase of approximately 25% is obtained at a stress ratio of $\frac{\sigma_2}{\sigma_1} = 0.5$ and of 16% at an equal biaxial compression stress state ($\frac{\sigma_2}{\sigma_1} = 1.0$). Under biaxial compression-tension, the compressive strength decreases almost linearly as the applied tensile stress is increased. Under biaxial tension, the strength is nearly the same as that under uniaxial tension.

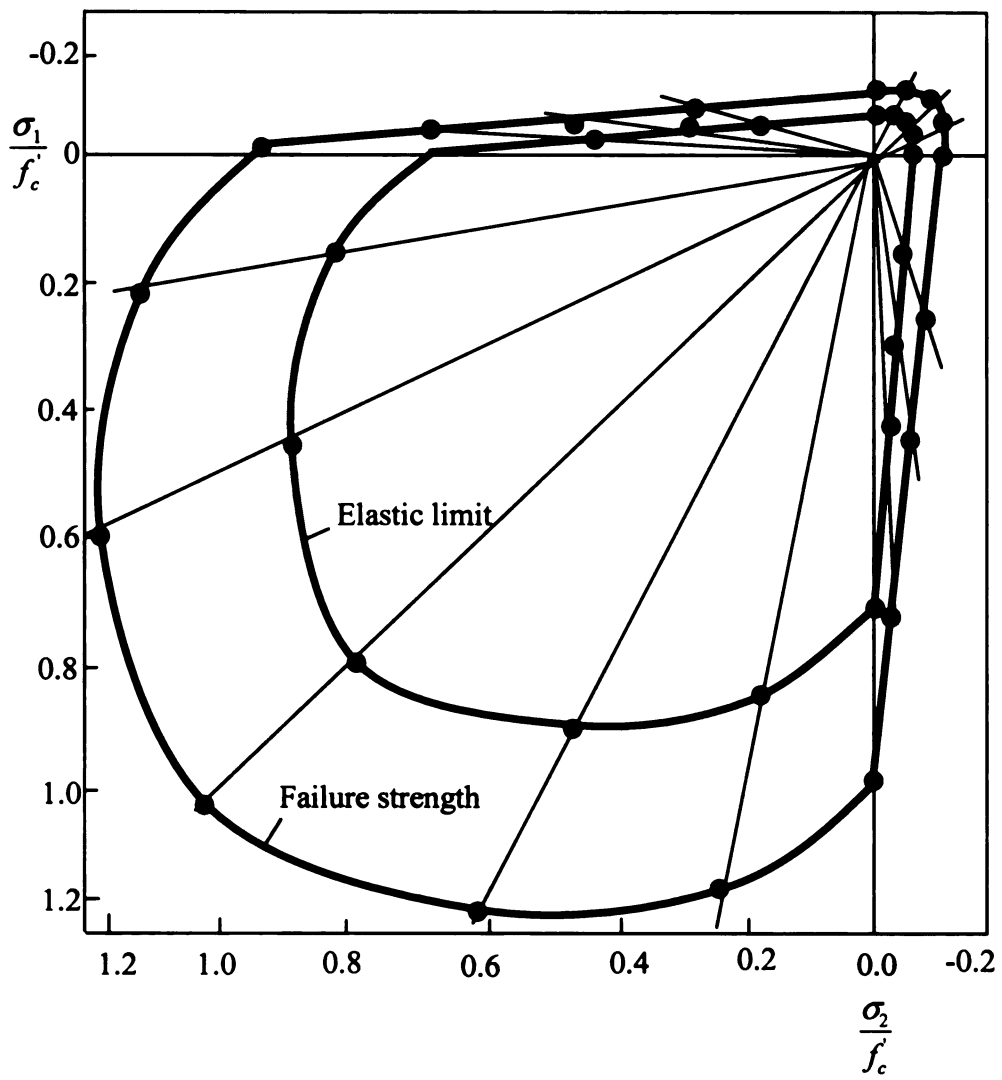

Figure 2.29 Elastic limit and maximum strength envelopes of concrete under biaxial loading (Tasuji, 1976).

Green and Swanson (1973) conducted hydrostatic compression tests on concrete. The tests indicated that concrete exhibits nonlinear behavior under hydrostatic compression, as shown in Figure 2.30. The stress-strain curve of Figure 2.30 shows a reversal in curvature on loading. Upon unloading, the slope of the curvature is almost constant and approximately equal to the slope of the initial tangent for the loading curve.

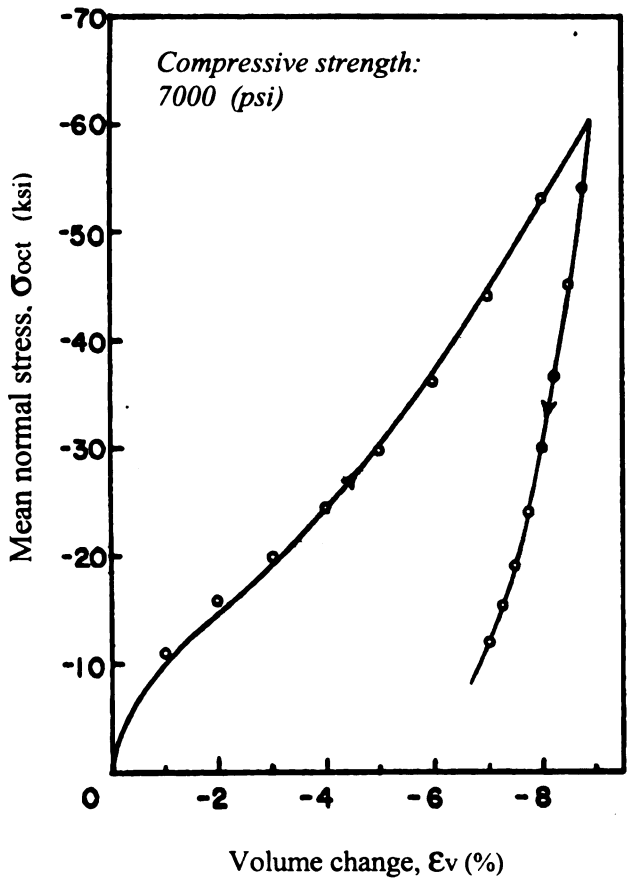

Figure 2.30 Behavior of concrete under hydrostatic compression (Green and Swanson, 1973).

Under triaxial loading, experiments indicate that concrete has a fairly consistent failure surface that is a function of the three principal stresses (Gerstle et al., 1978). If it is assumed that concrete is isotropic, the elastic limit (onset of stable crack propagation), the onset of unstable crack propagation, and the failure limit all can be represented as surfaces in three-dimensional principal stress space. The shape of the elastic limit surface and failure surface are shown schematically in Figure 2.31.

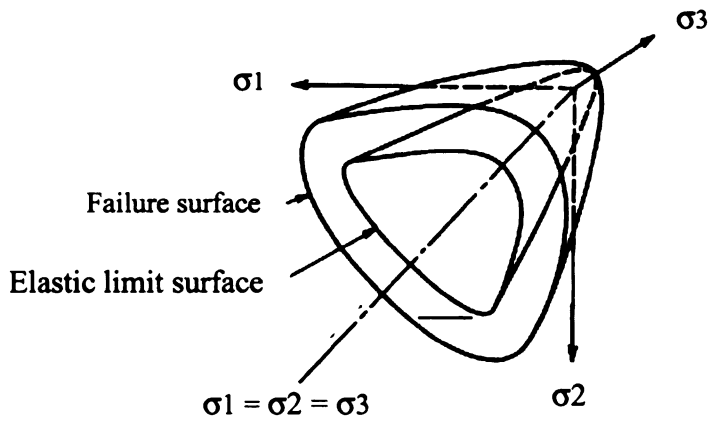

Figure 2.31 Schematic representation of the elastic limit and failure surface of concrete

2.12.2 Characteristics of yield surface

The general characteristics of the yield surface of concrete have been determined through experiments. The experimental results are used to develop mathematical failure models.

The general shape of the failure surface in the principal stress space can be best described by its cross-sectional shapes in the deviatoric planes and its meridians in the meridian planes. The cross sections of the failure surface are the intersection curves between the failure surface and a deviatoric plane which is perpendicular to the hydrostatic axis with ξ = constant. The meridians of the failure surface are the intersection curves between the failure surface and a plane (the meridian plane) containing the hydrostatic axis with θ = constant. Figure 2.32 shows a geometric representation of the stress state in the principal stress space. The straight line ON which has equal angles with the three coordinate axes is the hydrostatic axis. Deviatoric planes

are the planes that are perpendicular to the hydrostatic axis. Meridian planes are the planes that contain the hydrostatic axis.

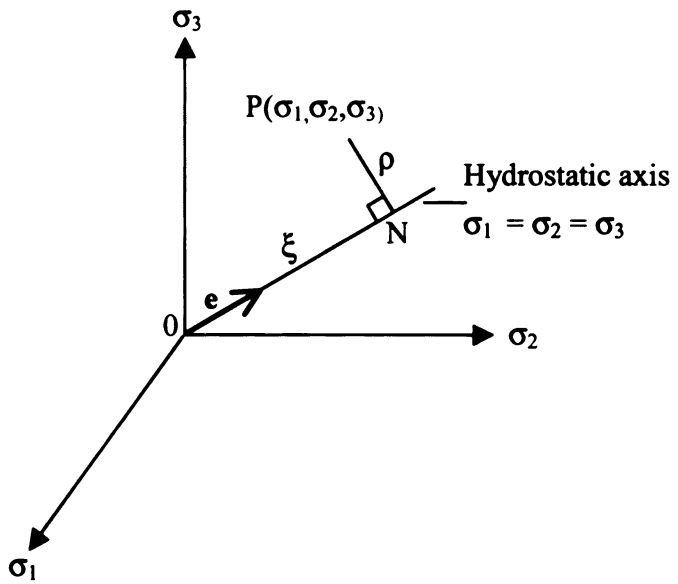

Figure 2.32 Geometric representation of the stress state in the principal stress space.

2.12.3 Failure surface of concrete under different stress states

The actual behavior and strength of concrete is complicated. This behavior depends on the geometric and material properties of the aggregate and cement paste, as well as the concrete curing condition and the nature of loading. Even though no one mathematical model can be expected to completely describe the strength properties of real concrete material, simpler models or criteria must be used in representing only those characteristics that are essential to the problem at hand.

Under tensile stresses concrete fails by a cleavage type of brittle fracture. Under high hydrostatic pressure, concrete can yield and flow as a ductile material on the failure or yield surface (Chen and Saleeb, 1982).

Under tensile loading, concrete failure can be described by Rankine's the maximum tensile stress criterion:

$$\sigma_1 = f_t', \qquad \sigma_2 = f_t', \qquad \sigma_3 = f_t' \tag{2.5}$$

where σ_i are principal stresses, and f_t' is the tensile strength.

Under high hydrostatic pressure, shearing stress criteria, such as the Tresca and Von Mises criteria, are used to predict the ductile fracture.

Tresca

$$\max[\frac{1}{2}|\sigma_1 - \sigma_2|, \frac{1}{2}|\sigma_1 - \sigma_2|, \frac{1}{2}|\sigma_1 - \sigma_2|] = k \tag{2.6}$$

Von Mises

$$f(J_2) = J_2 - k^2 = 0 \tag{2.7}$$

where k is the failure (yield) stress in pure shear. For concrete k is determined from a simple compression test (with f_c' used as the yield stress). In this case, k is equal to $\frac{1}{2} f_c'$ or $\frac{1}{\sqrt{3}} f_c'$ for the Tresca and Von Mises criteria, respectively. J_2 is the second invariant of the stress deviator tensor, and is

$$J_2 = \frac{1}{6}[(\sigma_1 - \sigma_2)^2 + (\sigma_2 - \sigma_3)^2 + (\sigma_3 - \sigma_1)^2], \quad \rho = \sqrt{2J_2} \tag{2.8}$$

In the intermediate compressive stress range, failure criteria of concrete are sensitive to the hydrostatic state of stress. The simple one-parameter models described above are not adequate for describing failure in the fracture-ductile state under this intermediate level of compressive stresses, and therefore pressure-dependent failure models must be used. The simplest and most commonly used models of this type are the

Mohr-Coulomb and Drucker-Prager failure criteria. These are two-parameter models whose meridians depend linearly on the hydrostatic stress component, I_1 or ξ

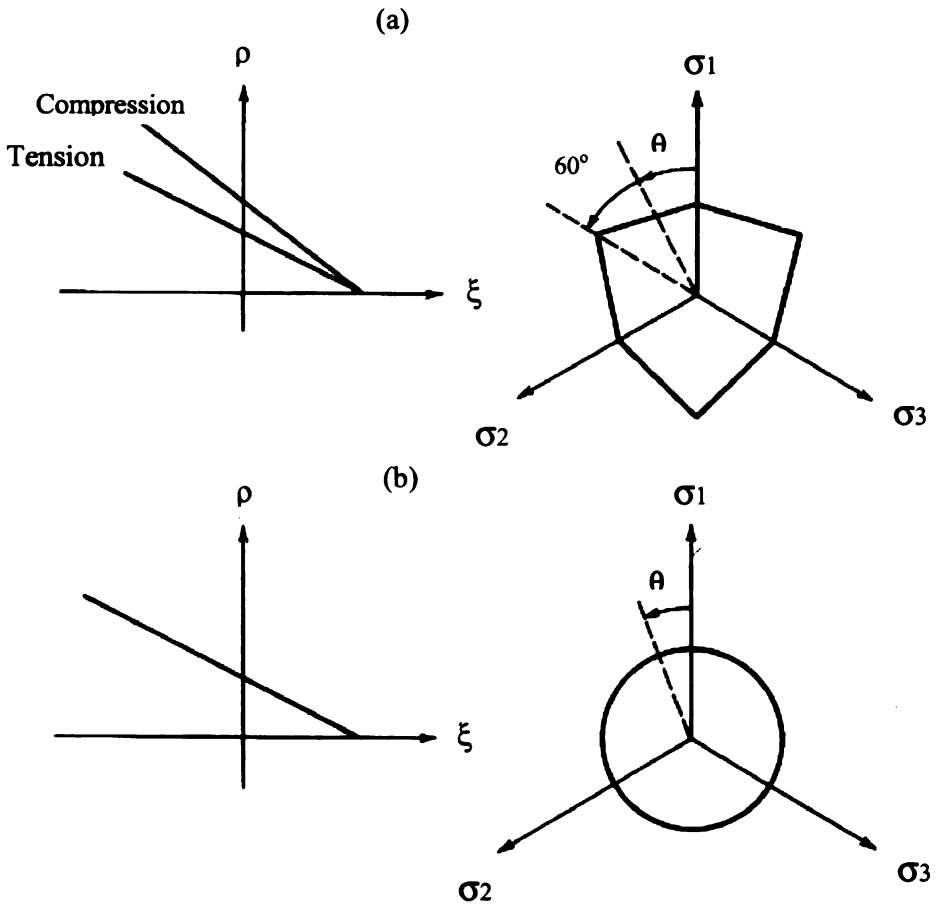

Figure 2.33 Meridian and deviatoric sections for two parameter failure models: (a) Mohr-Coulomb criterion, and (b) Drucker-Prager criterion.

In the Mohr-Coulomb criteria, failure is assumed to occur when the shear stress, τ, on any plane at a point in a concrete material reaches a value that depends linearly upon the normal stress, σ, in the same plane. Mathematically, this is expressed as

$$|\tau| = c - \sigma \tan\phi \tag{2.9}$$

where c and ϕ are material constants that represent the cohesion and angle of internal friction, respectively.

The Mohr-coulomb failure surface has sharp corners (Figure 2.33). These corners are not mathematically convenient because the slope discontinuity at these corners can cause many difficulties and complications in numerical solution schemes.

Drucker and Prager (1952) proposed a smooth approximation to the Mohr-Coulomb surface by the following simple modification of the von Mises criterion:

$$f(I_1, J_2) = \alpha I_1 + \sqrt{J_2} - k = 0 \tag{2.10}$$

or in term of ξ and ρ as

$$f(\xi, \rho) = \sqrt{6}\alpha\xi + \rho - \sqrt{2}k = 0 \tag{2.11}$$

where k and α are (positive) material constants. I_1 is the first principal stress invariant given by,

$$I_1 = \sigma_1 + \sigma_2 + \sigma_3 \tag{2.12}$$

There are two shortcomings of the Drucker-Prager criterion in modeling concrete material: the linear relation between I_1 and $\sqrt{J_2}$ (or ξ and ρ), and the independence with respect to the angle of similarity θ. Experiments on concrete show that relation between I_1 and $\sqrt{J_2}$ (or ξ and ρ) is nonlinear or curved, and the trace of the failure surface on deviatoric sections is not circular, but depends on the angle of similarity θ.

Bresler and Pister (1958) suggested a three-parameter failure criterion with a parabolic relation between τ_{oct} and σ_{oct} and with circular deviatoric sections. The relation between τ_{oct} and σ_{oct} can be expressed in the form of

$$\frac{\tau_{oct}}{f_c'} = a - b\left(\frac{\sigma_{oct}}{f_c'}\right) + c\left(\frac{\sigma_{oct}}{f_c'}\right)^2 \qquad (2.13)$$

Hsieh et al (1982) developed a four-parameter criterion in terms of I_1, J_2 and maximum principal stress σ_1:

$$f(I_1, I_2, \sigma_1) = a\frac{J_2}{f_c'^2} + b\frac{\sqrt{J_2}}{f_c'} + \frac{\sigma_1}{f_c'} + d\frac{I_1}{f_c'} - 1 = 0 \qquad (2.14)$$

where *a*, *b*, *c* and *d* are material constants. The nonlinear meridian trace and deviatoric sections of this failure model are shown in Figure 2.34.

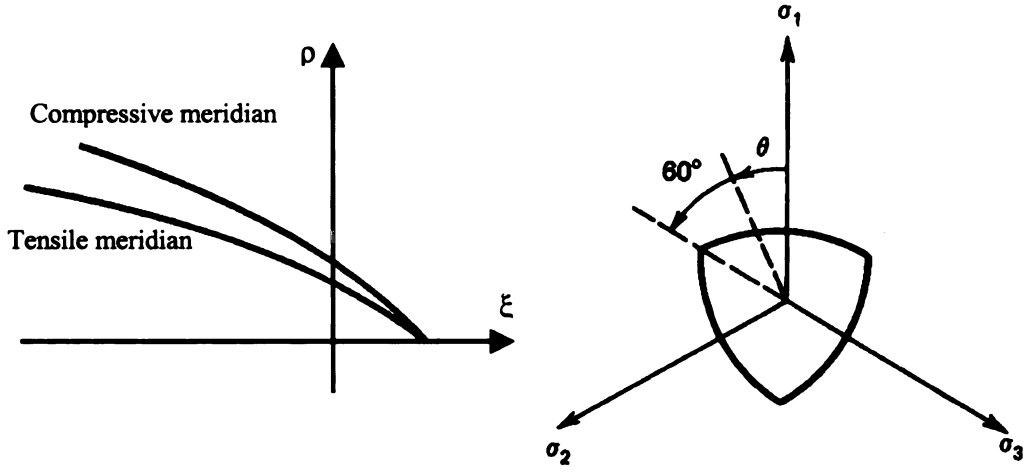

Figure 2.34 Hsieh-Ting-Chen criterion

A large number of concrete models have been published in the literature. Most of the modified models give a better agreement with relevant experimental data. However, the more accurate models generally involve many parameters that are difficult to obtain

experimentally. In practice, the Mohr-Coulomb and Drucker-Prager failure criteria are the most commonly used models.

2.12.4 Evolution of the yield surface of concrete under multi-dimensional loading

There are few investigations that have considered the evolution of the yield surface of concrete from the initial inelastic response through complete loss of strength. The concept of the evolution of the yield surface of concrete is cited from the theory of plasticity. In plasticity theory, a change of yield surface is always described by a hardening rule. There are two common hardening rules: 'isotropic hardening' in which a change occurs in the size of the yield surface only (all dimensions being scaled by the same constant); and 'kinematic hardening' in which a change occurs in the location of the yield surface. 'Isotropic hardening' is the more appropriate hardening rule for concrete.

Chen and Han [1988] proposed a more detailed evolution of the yield surface of concrete under a variable load history (Figure 2.35). This model proposes that at the maximum load, the yield surface may appropriately be defined by the recommendations of any of several researchers [Ottosen, 1977; Hsieh *et al.*, 1982; Willam and Warnke, 1975].

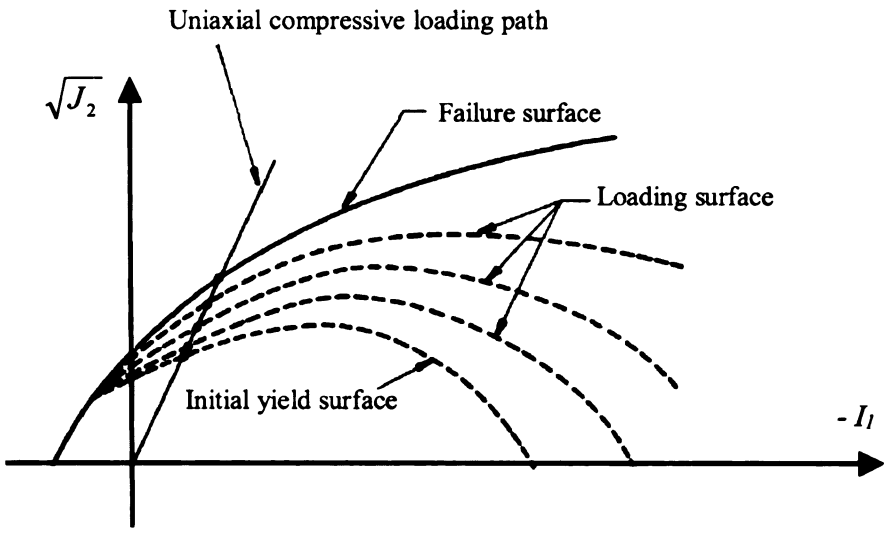

Figure 2.35 Evolution of concrete yield surface as proposed by Chen and Han [1988].

2.13 Finite Element Modeling for Vehicle Crash Analysis

In the last four decades, the finite element method (FEM) has become the dominant technique for analyzing physical phenomena in the field of structural, solid, and fluid mechanics.

The nonlinear, explicit, three-dimensional finite element analysis code DYNA3D developed in the 1970s has made it possible to analyze contact impact problems. The first full vehicle car crash model was built and analyzed in the mid-1980s (Du Dois, 1999). Nowadays, crash simulation has become a routine task in vehicle design. However, making a high quality finite element (FE) model that can match actual vehicle behavior is still a formidable challenge for engineers. A high quality FE model should not only have good geometry with high quality elements, but also have good material modeling, contact modeling and control commands.

2.13.1 Brief summary of formulations

LS-DYNA (Hallquist, 1999) is a nonlinear, dynamic, three-dimensional finite element analysis code that evolved from DYNA3D. It is being widely used from the automotive to the biomechanics fields.

LS-DYNA uses a Lagrangian formulation in which the mesh moves with the material. Formulation in fluid dynamics is, in contrast, Eulerian, and the FE mesh remains fixed in space. In LS-DYNA, conditions of equilibrium are derived by the principle of virtual work and are expressed by the following equation:

$$M_{ijkl}\,\ddot{x}^{n}_{kl} = F^{n}_{ij} \tag{2.15}$$

where

M_{ijkl} is the diagonal (lumped) mass matrix;

$\ddot{x}^{n}_{kl}$ is the acceleration at node k with respect to degree of freedom l;

F_{ij} is the sum of the internal and external forces; and the superscript n refers to the n-th integration time step.

The diagonal mass matrix enables equation (2.14) to be solved easily for the accelerations. The velocities and displacements are then obtained through the explicit central difference method:

$$\begin{aligned}
\dot{x}_{ij}^{n+\frac{1}{2}} &= \dot{x}_{ij}^{n-\frac{1}{2}} + \Delta t^{n}\ddot{x}_{ij}^{n} \\
\dot{x}_{ij}^{n+1} &= \dot{x}_{ij}^{n} + \Delta t^{n+\frac{1}{2}}\ddot{x}_{ij}^{n+\frac{1}{2}} \\
\Delta t^{n+\frac{1}{2}} &= \frac{1}{2}(\Delta t^{n+1} + \Delta t^{n})
\end{aligned} \tag{2.16}$$

where Δt is the integration time step.

2.13.2 Time integration

The central difference method is an explicit integration method that is conditionally stable. If Δt is too large, the method becomes unstable. If Δt is much smaller than necessary, computations become expensive. Therefore, it is necessary to choose the time step Δt so that the method is stable and effective. The stability condition is given by the Courant, Friedrichs, and Lewy condition.

$$\Delta t \leq \frac{L}{c} \tag{2.17}$$

where $c = \sqrt{E/\rho}$ is the speed at which information travels in the element, E is the modulus of elasticity of the material, and ρ is the density of the material. L is the characteristic length of elements.

The physical interpretation of this condition is that Δt must be small enough so that information does not propagate across more than one element per time step.

2.13.3 Contact algorithm

The general contact approach taken in LS-DYNA is referred to as the "penalty method." When a node penetrates a surface, it is opposed by a linear spring force that acts normal to the surface. This force is calculated using plate theory based on the depth of the penetration and the stiffness of the surface element. If friction is specified, then the friction force is calculated from the normal force. A node trying to penetrate the surface is usually referred to as the "slave" node, and the surface it is trying to penetrate is the

"master segment." These terms appeared in the finite difference literature when most contact algorithms were not symmetric.

2.13.4 Force and displacement field quantities

The LS-DYNA analysis mainly outputs force field quantities and displacement field quantities. The force field quantities mainly include stresses and strains, and the displacement field quantities mainly include displacements, velocities and accelerations.

In LS-DYNA analysis, force field quantities vary over the element. To reduce the CPU time, it is assumed that the stress and strain are constant over the element and equal to the values calculated at the center of the element (or at the integration point). However, the displacement field quantities (acceleration, velocity and displacement) are evaluated at the nodal points.

2.13.5 Simulation of barrier crash tests using LS-DYNA

Designing safer roadside crash barriers in highway systems is a primary goal of the state DOTs and the Federal Highway Administration (FHWA). The crashworthiness of some roadside barriers has been evaluated through full-scale field-testing. Crash testing has been carried out for many years but at considerable expense. If accurate computational models can be developed and then used to predict the effects of vehicle-barrier collisions, enhanced designs of such hardware systems can be achieved more efficiently.

Finite element analysis based upon the failure mechanics of traditional materials provides the best computational tool with which to undertake research that will lead to a

better understanding of the behavior of roadside safety structures. This will eventually lead to the formulation of improved designs, possibly utilizing new high-performance materials in the fabrication of roadside safety structures.

Previous simulation studies of vehicles impacting a guardrail (Plaxico, 1995) and a concrete barrier (Nilsson, 1998) show that the finite element simulations of vehicle-barrier impacts provide good agreement with the results of full-scale field tests. Figures 2.36 and Figure 2.37 show a crash simulation using LS-DYNA computer program conducted at Texas A&M University in 1999 and a crash field test conducted by the Washington State DOT in 1998 on a new portable concrete barriers.

Figure 2.36 Crash field test (front view) (Roger, 2002)

Figure 2.37 Crash Simulation (front view) (Roger, 2002)

Comparing Figure 2.36 with Figure 2.37, the vehicle's frontal right corner deformation and the shape of the deformed concrete barrier are almost identical. The computer crash simulation with LS-DYNA provides an excellent prediction of the vehicles motion during impact.

Figures 2.38 and 2.39 show the crash simulation and crash field test on a longitudinal concrete barrier conducted by the National Crash Analysis Center in 1995 (Zaouk, 1995). Again, the simulation predicts the motion of the vehicle quite well. The simulation also provide insights that are not available from field tests about the design parameters such as detailed material responses.

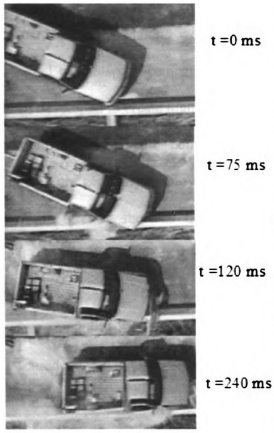

Figure 2.38 Crash field test (plan view)

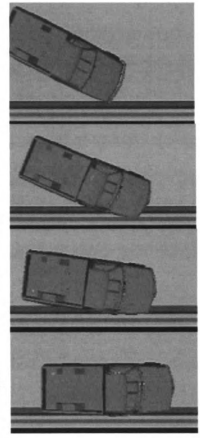

Figure 2.39 Crash simulation (plan view)

CHAPTER 3

IMPROVED MANUFACTURING PROCESS AND FLEXURAL PERFORMANCE

3.1 Introduction

The manufacturing of cement-bonded particleboard is similar to that of resin-bonded particleboard. Making wood-cement particleboard stronger and tougher is the primary goal of the wood-cement composite industry. Better manufacturing processes have been developed to create high quality wood-cement particleboards. Up to now, two major modifications of the conventional manufacturing process for wood-cement particleboard are generally employed. One of these is the accelerated process with CO_2 injection that greatly shortens the manufacturing time. Another is the addition of chemical additives to improve the bonding strength between wood particles and the cement matrix.

Simatupang (1990) studied the performances of conventional (air curing) and rapidly cured (using CO_2) cement-bonded wood particleboard. He concluded that conventionally cured cement-bonded wood particleboards have higher bending strength and are also more durable. However, the properties of the rapidly cured boards fulfill the requirements of existing standards (Hsu, 1995).

Chemical additives in wood cement composites does improve the bending strength of the composites, but the improvement is limited. And as with the CO_2 injection process, the chemical additive increases the manufacturing cost.

In the research reported herein, a pressure controlled and fully saturated curing process was investigated. This manufacturing process yields significant advantages over currently used manufacturing procedures. A total of 70 flexural specimens with different cement/wood ratios were fabricated using the fully saturated curing process and tested. In addition to the effect of the curing process the effect of the cement/wood ratio on the strength of wood-cement particleboard also was investigated.

3.2 Pressure Controlled and Fully Saturated Curing Process

In the pressure controlled and fully saturated curing process, the particleboard is pressed with a constant pressure and is fully saturated in water for a 28-day curing period.

3.2.1 Advantages of pressure controlled and fully saturated curing process

In the currently used accelerated and air curing methods, wood particles shrink during the curing period. The shrinkage induces some degree of debonding between the wood particles and the cement matrix before the cement is fully hardened. Further, the debonding action weakens the bond strength between wood particles and the cement matrix resulting in the particleboard having a lower material strength.

The fully saturated curing procedure improves bond strength between wood particles and the cement matrix. The bond strength between wood particles and cement is related to the interlock between the irregular surfaces of wood particles and the cement matrix. Because wood particles do not shrink in water during the 28-day curing period due to the fully saturated condition, the interface between wood particles and the cement

matrix provides considerable bond strength. Pressure controlled manufacturing with fully saturated curing should therefore produce superior wood-cement particleboard.

In addition, in the pressure controlled manufacturing process specimens with different cement/wood ratios experience the same pressure during the setting period and the cement and wood particles in the specimens develop the same internal prestresses. Therefore, specimens made by this process yield stronger correlations between material properties and cement/wood ratios.

3.2.2 Materials

The materials used in this research are soft wood (southern yellow pine) particles, Portland cement (Type I) and water. The particles were made from waste wood treated with chromated copper arsenate (CCA).

In this study, CCA-treated wood (southern yellow pine) removed from service is used to produce wood particles. Figure 3.1 shows a typical cross section of CCA-treated southern yellow pine removed from service. The wood particles were produced through two steps. First, crushed wood is placed into a cutting machine (Figure 3.3) to produce raw wood particles. Second, the particles are separated by size by sieving with Tyler Screens (Figure 3.4). Particles (Figure 3.2) with size from 2 to 8 mm long x 1.0 mm in diameter are selected for making the particleboard.

All the wood particles used in this research were made at the Wood Technology Laboratory in the Department of Forestry at Michigan State University.

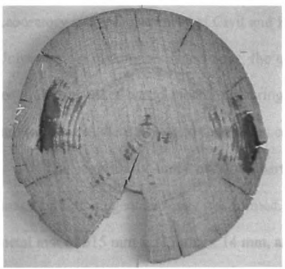

Figure 3.1. CCA-treated wood

Figure 3.2. Wood particles

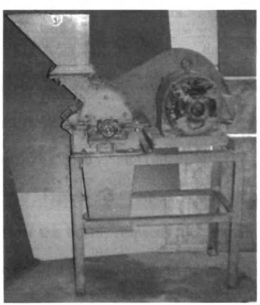

Figure 3.3. Wood particle cuting machine

Figure 3.4. Wood particle screener

3.2.3 Particleboard manufacturing

All wood-cement composite specimens were fabricated in the Concrete Material Laboratory in the Department of Civil and Environmental Engineering at Michigan State University. In making test specimens, the quantity of wood particles, water and cement required to produce particleboard measuring 315 mm (wide) by 315 mm (long) by 12~20 mm (thickness) were estimated for a given cement/wood ratio.

The required quantity of wood particles, cement and water were mechanically mixed until homogenous slurry was formed. The composite slurry was transferred onto a metal mat of 315 mm x 315 mm x 14 mm, and loaded onto a hydraulic press for pressing. The mat remained under pressure for 24 hours. After 24 hours of cold pressing, the particleboard was removed and put into a water container for 28 days of curing under the laboratory room environment.

After 28 days of curing, the particleboard was removed from the water and left to dry in the laboratory environment for two days. A table saw was then used to cut each particleboard into the test specimens with dimensions of 230 mm (long) by 100 mm (wide) by 10 to 22 mm (thick).

Figures 3.5 to 3.8 show the mixer, hydraulic press, curing container and saw used to cut the board, respectively. Figure 3.9 shows the flowchart of the manufacturing process for the wood-cement particleboard.

Figure 3.5. Cement wood particle mixer

Figure 3.6. Hydraulic press

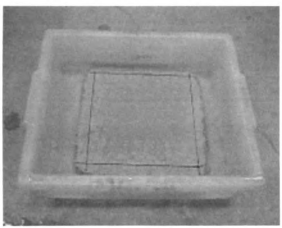

Figure 3.7. Curing in water

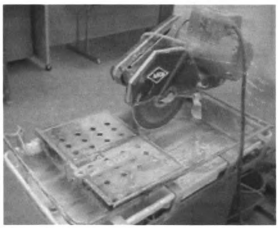

Figure 3.8. Saw used to cut board

Flowchart of Wood-Cement Particleboard Manufacturing Process

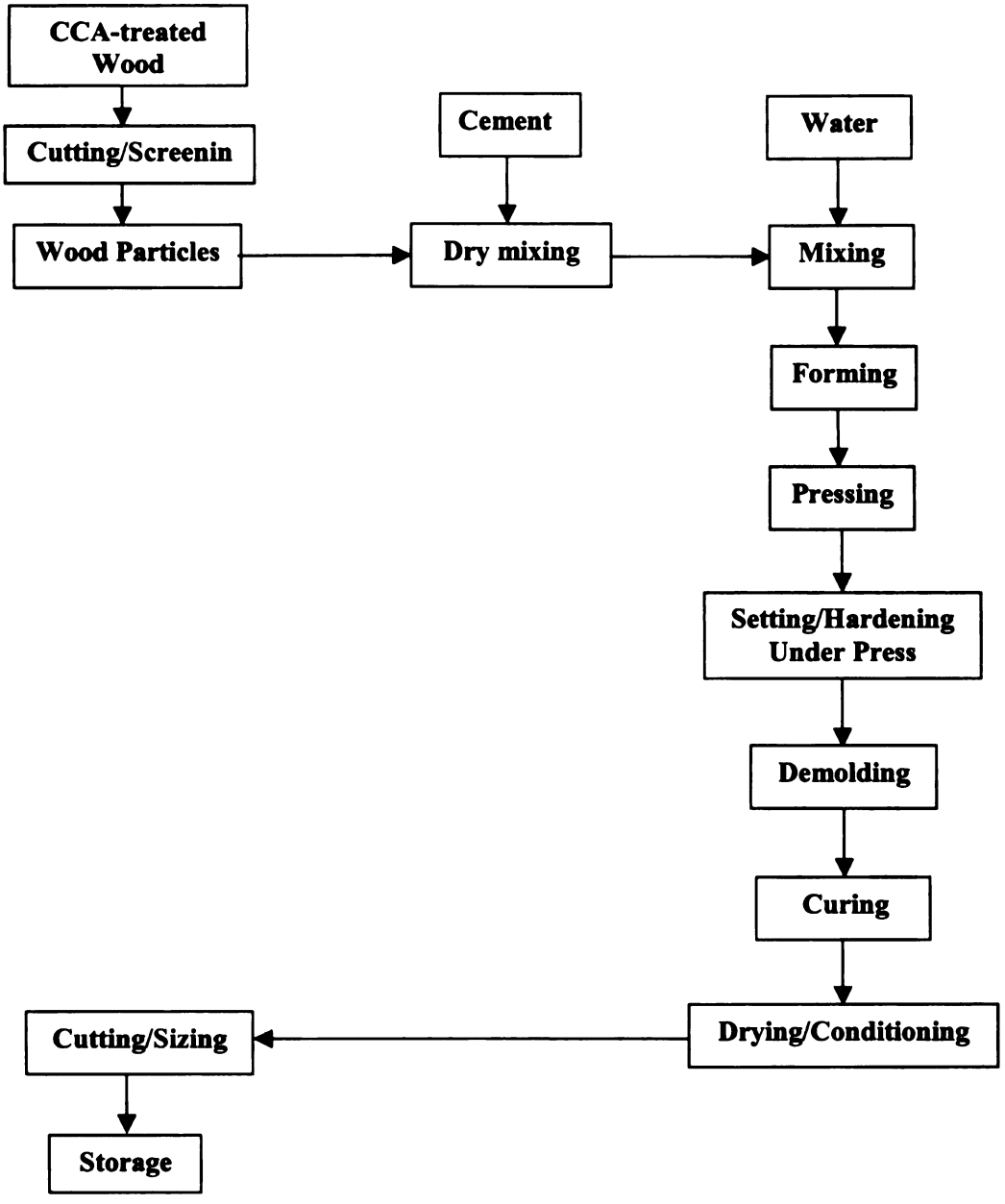

Figure 3.9 Flowchart of manufacturing process

3.3 Flexural Properties of Wood-Cement Particleboard

Wood-cement particleboard is presently used mainly as non-structural members in building construction. They are often subjected bending load (e.g. particleboard siding subjected to wind load). The bending strength of the wood-cement particleboard is generally used to evaluate the quality of the boards in the wood-cement composites industry and is an important property.

3.3.1 Experimental Design

Wood–cement particleboard using CCA-treated softwood particles, Portland cement (Type I), and water, were fabricated as described in Section 3.1.3. The test matrix for the bending test is given in Table 3.1. All specimens had a length of 230 mm, a width of 100 mm and a thickness that varied from 12 to 20 mm.

Table 3.1 Test Matrix for Bending Test

Cement/wood ratio	4.0	3.5	3.0	2.0	1.5	1.25	1.0
Number of specimens	10	10	10	10	10	10	10

3.3.2 Description of Test

Bending tests were conducted to determine material properties of the wood-cement particleboard. The American National Standards Institute Specifications for particleboard (ANSI A208.1-1993) and The American Society for Testing and Materials (standard method of evaluating the properties of wood based fiber and particle panel materials, ASTM D 1037-78, 1996) were used.

Three point bending tests were conducted on an INSTRON machine (Figure 3.10) to determine the modulus of rupture (MOR), modulus of elasticity (MOE) and the strain at peak load. The tests were conducted in the Department of Forestry at Michigan State University. Figure 3.11 shows the test set-up. The sizes of the test specimens is shown in Figure 3.12.

Figure 3.10. INSTRON Machine

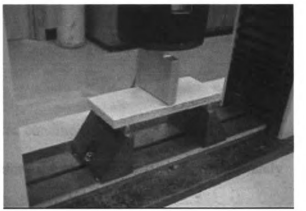

Figure 3.11. Bending test set-up

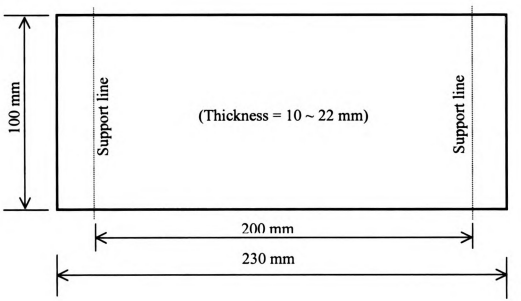

Figure 3.12 Specimen's size

The loading speed was based on ASTM D 1037-78 (1996). The loading rate of the moveable crosshead of the test machine calculated as follows:

$$N = zL^2/6d \tag{3.1}$$

where:

N = rate of motion of moving head, in./min (mm/min),

z = unit rate of fiber strain, in./in.(mm/mm) of outer fiber length per minute (0.005),

L = span, in. (mm) and

d = depth (thickness) of specimen, in. (mm).

The specimens to be tested in the soaked condition were submerged in water at a temperature of 20° ± 3° C for 24 hours before the test and were tested immediately upon removal from the water.

3.3.3 Test results and analysis

The typical failure characteristics of the specimens under bending are shown in Figures 3.13 and 3.14. Observation of the bending test showed that failure does not generally occurs due to a straight crack but due to a network of independent cracks as shown in Figure 3.13 that are most likely caused by the wood particle's bridging action. The cross sectional view of the particleboard's failure (Figure 3.14) further indicates that the wood particles play a bridging action role in resisting bending load.

Figure 3.13 and 3.14 show that the wood-cement particleboard failure under bending occurs after the wood particles pull out from the cement matrix. As the wood

particles were pulled out, the bridging action disappears and the board loses its bending capacity.

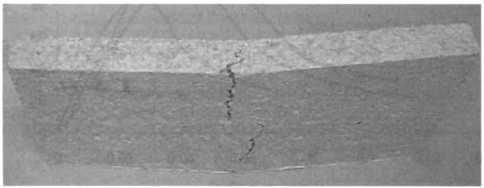

Figure 3.13. Bending failure

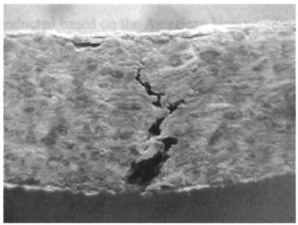

Figure 3.14. Cross-section view of failure

The typical load-deflection curves (Figure 3.15) show that the WCPB behaves as an elastic-degrading plastic material with significant loss of strength following the achievement of peak load.

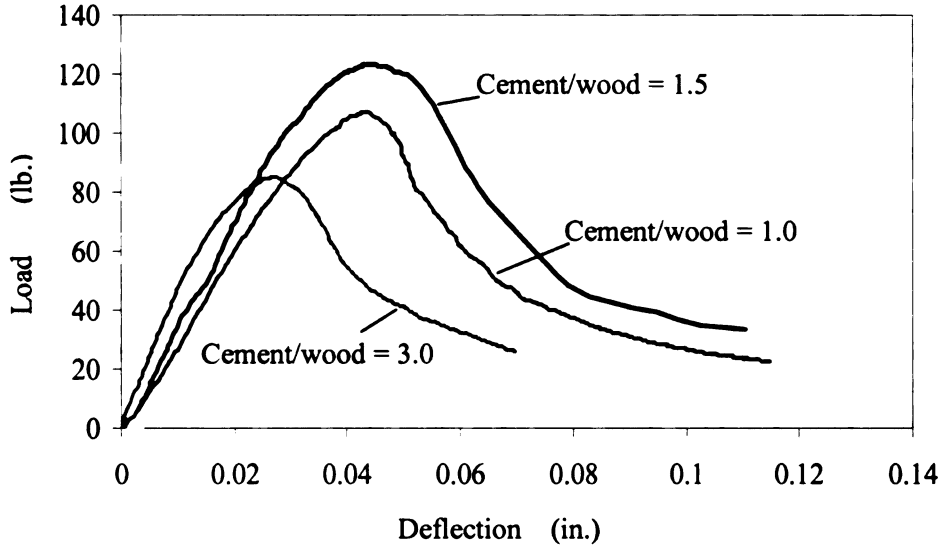

Figure 3.15. Load-deflection curves for varying cement/wood ratios

The test was conducted based on the American National Standard ASTM D 1037-78, (1996).

For the static bending test, the ASTM D 1037-78 defines the modulus of rupture and the modulus of elasticity as follows:

$$\text{MOR} = 3PL/2bd^2 \tag{3.2}$$

$$\text{MOE} = P_1L^3/4bd^3y_1 \tag{3.3}$$

where:

b = width of specimen, in. (mm),

d = thickness (depth) of specimen, in. (mm),

L = length of span, in. (mm),

P = maximum load, lbf (N),

P_l = load at proportional limit, lbf (N),

MOR = modulus of rupture, psi (kPa),

MOE = stiffness (aparent modulus of elasticity), psi (kPa),

y_l = center deflection at proportional limit load, in. (mm).

The measured flextural strength (modulus of rupture), modulus of elasticity and density of the wood-cement particleboard are presented in Table 3.2 and Figure 3.16 to Figure 3.18.

Table 3.2 Flexural Performence of Wood -Cement Particleboard Manufactured with Seven Different Cement/Wood Ratios

Test Results		Modulus of Rupture (MPa)		Modulus of Elasticity (MPa)		Density (kg/m^3)	
		Mean	St. Dev.	Mean	St. Dev.	Mean	St. Dev.
Cement/wood ratio	1.0	10.11	0.72	1670	180	967	52
	1.25	10.33	0.63	1980	186	978	49
	1.5	11.71	0.44	3027	305	1044	31
	2.0	9.53	0.68	3319	402	1151	34
	3.0	7.03	0.29	3606	414	1329	46
	3.5	7.4	0.65	4376	565	1468	67
	4.0	7.31	0.71	5026	637	1551	71

Figure 3.16 indicates that a cement/wood ratio of 1.5 yields the highest modulus of rupture and the largest strain at peak load. When the cement/wood ratio is large, there are insufficient wood particles to provide effective bridging action and hence the MOR is low. When the cement/wood ratio is too low, there is insufficient binder to fully bond the fibers with the matrix. A cement/wood ratio of 1.5 appears to be optimal. Figure 3.17 shows that the modulus of elasticity increases almost linearly with increasing cement/wood ratio. Figure 3.18 shows that the density of the board increases linearly

with increasing cement/wood ratio. The cement/wood ratios of 1.5 and 1.0 were used for all other tests.

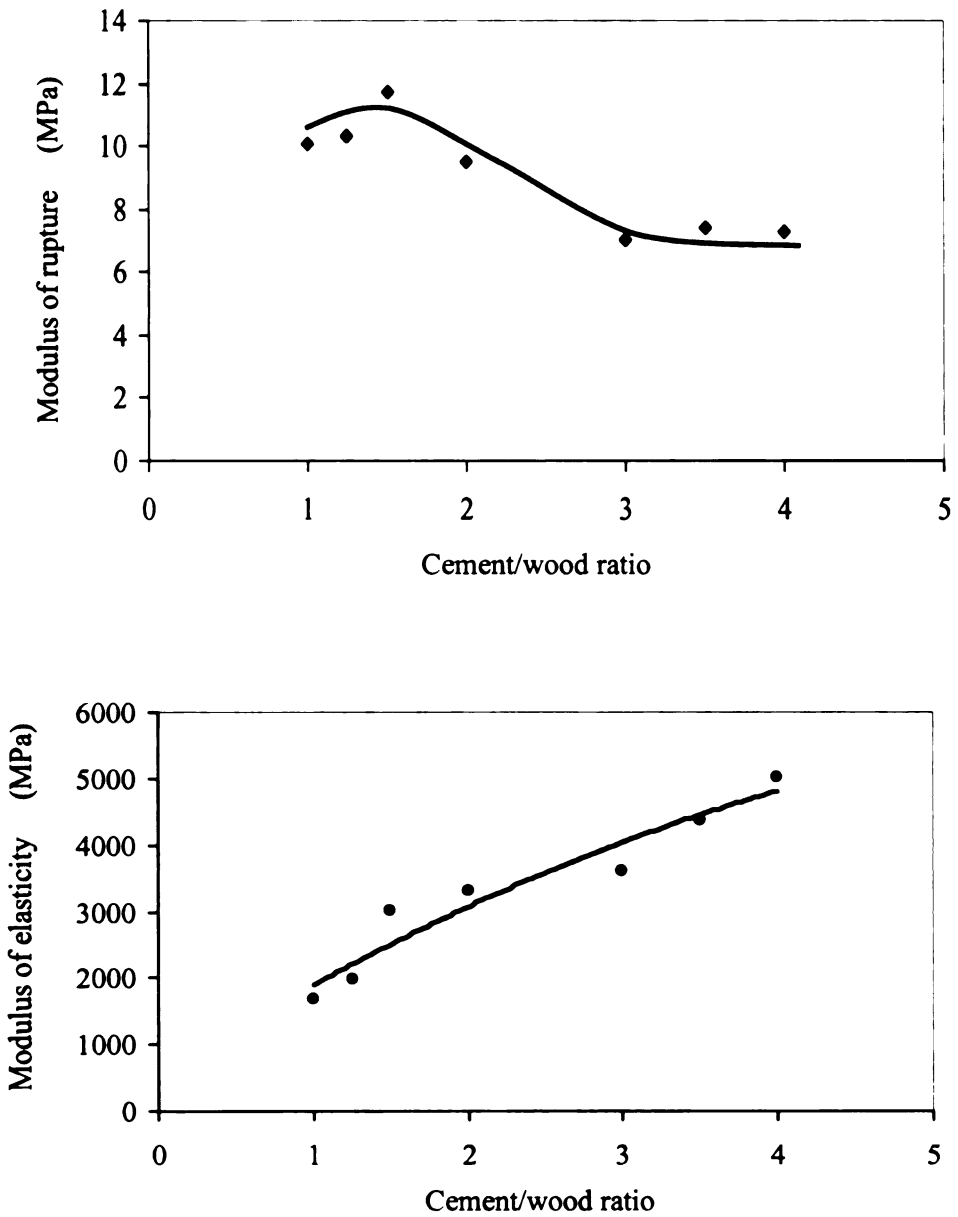

Figure 3.17. Correlation between MOE and cement/wood ratio

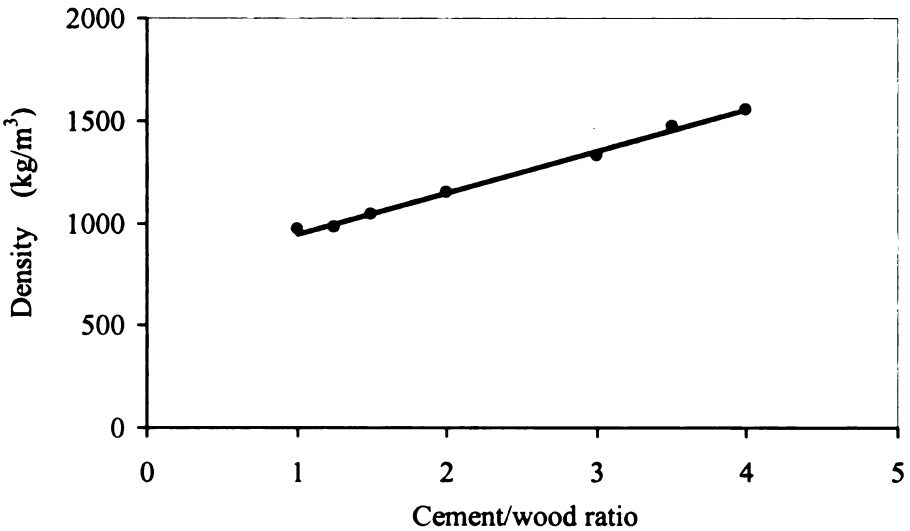

Figure 3.18. Correlation between density and cement/wood ratio

Toughness is generally used as a measure of energy dissipation for a material. The most common method to measure toughness is to use the load-deflection curve of a simply supported beam under bending. There are at least three procedures that are suggested to quantify toughness using the load-deflection curve obtained in static loading. As reported by ACI Committee 544 on Fiber Reinforced Concrete, the ideal way to define the toughness index I_t is by the following ratio:

$$I_t = \frac{\begin{array}{c}\textit{Area under the load}-\textit{deflection curve until the} \\ \textit{load reaches zero for fiber composite}\end{array}}{\begin{array}{c}\textit{Area under the load}-\textit{deflection curve until the} \\ \textit{load reaches zero for plain matrix}\end{array}} \qquad (3.4)$$

In equation (3.4), the energy absorbed by a fiber-reinforced composite beam is normalized by dividing it by the energy absorbed by an identical beam made with the plain matrix. While equation (3.4) is conceptually sound, it poses a number of practical difficulties (e.g., plain concrete often suddenly collapses.).

In practice, the ASTM C1018 procedure is more suitable for the toughness index I_t. In the ASTM C1018 procedure, the denominator in equation (3.4) is taken as the area under the load-deflection curve up to the first crack. The first crack is assumed to occur at the point where the load-deflection curve deviates from the initial linear portion. The numerator is taken as the area under the load-deflection curve up to a certain specified deflection. Three levels of deflection, namely, 3δ, 5.5δ and 10.5δ, are suggested for the numerator, where δ is the deflection at first crack. The three suggested indices, called I_5, I_{10}, and I_{20} are defined as:

$$I_5 = \frac{Area\ under\ the\ load-deflection\ curve\quad up\ to\ 3\delta}{Area\ under\ the\ load-deflection\ up\ to\ \delta} \tag{3.5}$$

$$I_{10} = \frac{Area\ up\ to\ 5.5\delta}{Area\ up\ to\ \delta} \tag{3.6}$$

$$I_{20} = \frac{Area\ up\ to\ 10.5\delta}{Area\ up\ to\ \delta} \tag{3.7}$$

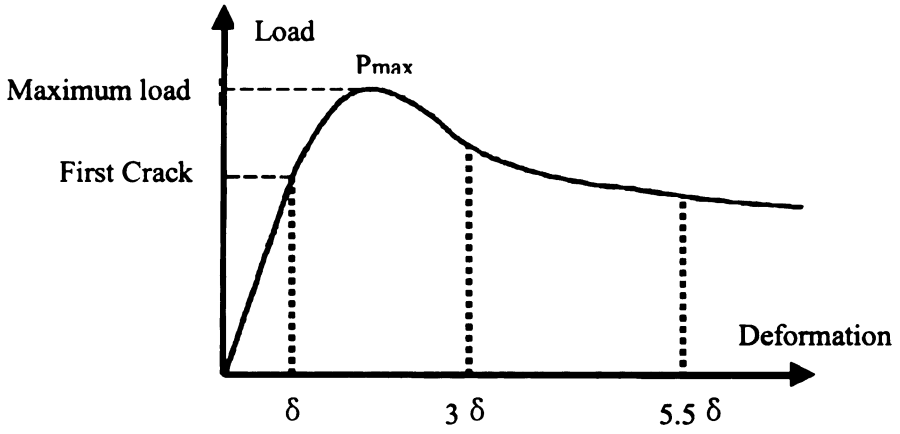

Figure 3.19 Toughness calculation curve (load-deformation curve)

The procedure is shown schematically in Figure 3.19. If a plain concrete beam is tested under load control, the beam would break into two pieces right after the first crack occurs, yielding a toughness index of 1.0.

In this research, the ASTM C1018 procedure was applied to calculate the toughness of wood-cement particle composites. Table 3.3 shows the calculated toughness index I_5 for wood cement particleboard with seven different cement/wood ratios under three-point bending tests. The calculated toughness indices (I_5) are roughly around 6.0.

Table 3.3 Flexural Toughness of Wood Cement Particleboard

Toughness Results		Cement/Wood Ratio						
		1.0	1.25	1.5	2.0	3.0	3.5	4.0
Toughness I_5	Mean	5.95	6.04	6.22	6.18	6.33	5.81	5.72
	St. Dev.	0.11	0.08	0.16	0.21	0.25	0.22	0.33

Statistical analysis of the test results confirmed that the fully saturated curing process yielded improved flexural performance at the 95 % level of confidence. The confidence interval level is calculated by the formula:

$$\overline{X} + 1.96\left(\frac{\sigma}{n}\right) \tag{3.8}$$

where, $\overline{X}$ is the mean value, σ is the standard deviation and n is the number of samples.

The modulus of rupture, modulus of elasticity, density and toughness index of wood-cement particleboards with seven different cement/wood ratios are shown in Figure 3.20, Figure 3.21, Figure 3.23 and Figure 3.25, respectively. The 95% confidence interval is shown using error bars.

Figure 3.22 and Figure 3.24 show the linear regression lines for modulus of elasticity (MOE) vs. cement/wood ratio and density vs. cement/wood ratio, respectively. The linear regression equations has the following form:

$$y = a + bx, \quad \text{with an estimate of } R^2 \tag{3.9}$$

where x is the explanatory variable, y is the dependent variable, and a and b are constant.

The a, b and R^2 are calculated from the equations:

$$\begin{cases} l_{xy} = \sum_{1}^{n} (x_i - \bar{x})^2 \\ l_{xy} = \sum_{1}^{n} (x_i - \bar{x})(y_i - \bar{y}) \\ l_{yy} = \sum_{1}^{n} (y_i - \bar{y})^2 \\ b = \dfrac{l_{xy}}{l_{xx}} \\ a = \bar{y} - \dfrac{l_{xy}}{l_{xx}} \bar{x} \\ R^2 = \dfrac{1}{n} l_{yy} \left(1 - \dfrac{l_{xy}^2}{l_{xx} l_{yy}}\right) \end{cases} \tag{3.10}$$

where n is the number of samples.

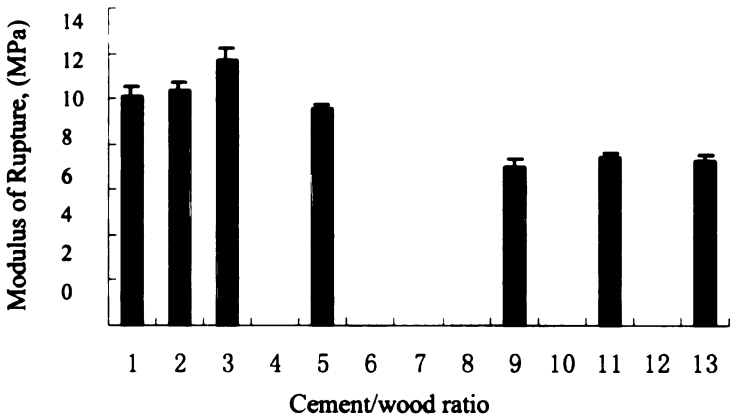

Figure 3.20 Variation of modulus of rupture vs. cement/wood ratio and 95% confidence interval

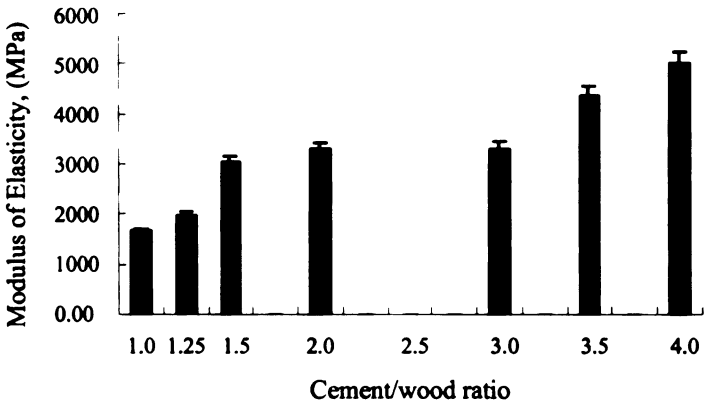

Figure 3.21 Variation of modulus of elasticity vs. cement/wood ratio and 95% confidence interval

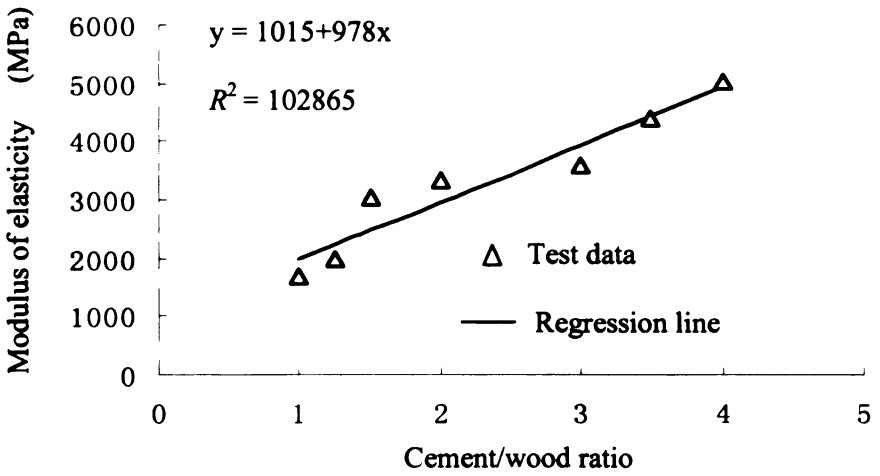

Figure 3.22 Modulus of elasticity vs. cement/wood ratio

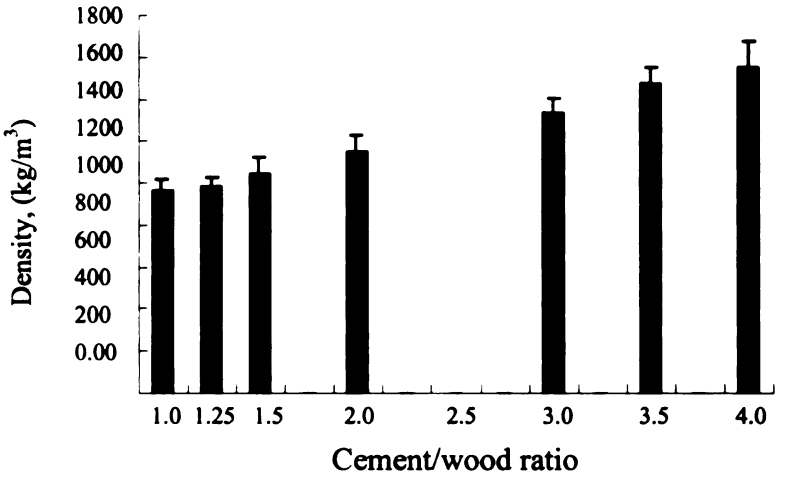

Figure 3.23 Variation of density vs. cement/wood ratio and 95% confidence interval

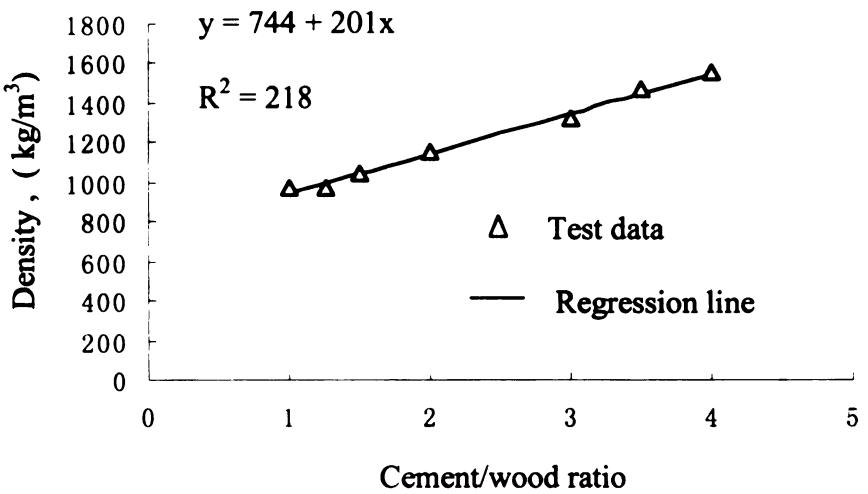

Figure 3.24 Density vs. cement/wood ratio

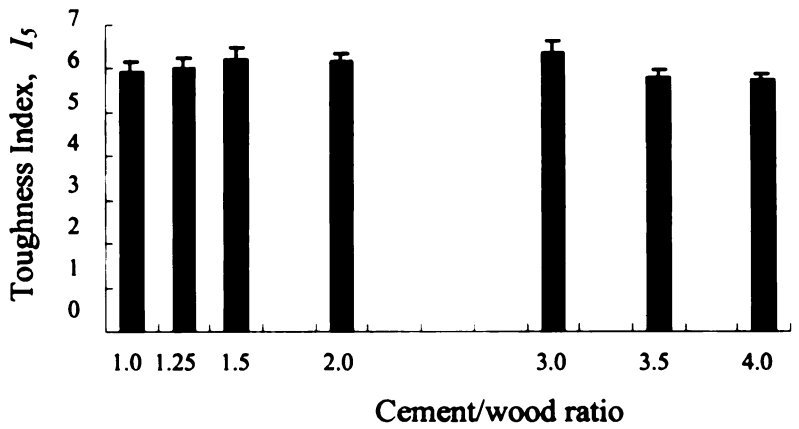

Figure 3.25 Variation of toughness index vs. cement/wood ratio and 95% confidence interval

3.4 Discussion

Flexural test results show that the pressure controlled and fully saturated curing process improves the bending strength of the wood-cement particleboard to 11.7 MPa which is higher than the commonly accepted limit of 10 MPa (Wolfe, 1996).

A more reliable relationship between bending strength and cement/wood ratio was found for wood-cement particleboards manufactured using the pressure controlled and fully saturated curing process. The test results show that wood-cement particleboard with a cement/wood ratio of 1.5 yields the maximum bending strength (or modulus of rupture). Consequently, the cement/wood ratio of 1.5 was considered as an optimum value for making wood-cement particleboard. The test results also indicate that the bending strength of the composite increases with the increase of cement/wood ratio from 1.0 to 1.5 and then decreases as the cement/wood ratio increases further from 1.5 to 4.0. The correlation between bending strength and the cement/wood ratio is consistent with test

results reported by Prestemon (1976) that wood-cement particleboard had higher bending strength properties when the cement/wood ratio was increased from 0.75 to 1.5, and also with the results reported by Moslemi and Pfister (1987) that the modulus of rupture of wood-cement flakeboard increased as the cement/wood ratio was lowered from 3.0 to 1.5.

The test results also show that the modulus of elasticity increases almost linearly as the cement/wood ratio is increased from 1.0 to 4.0. And the density of the wood cement particleboard increases linearly with the increase of cement/wood ratios.

The toughness indices derived from test results under bending test are around 6.0. And the results indicate that a cement/wood ratio has no significant influence on the toughness index of the particleboard. The toughness index (*I5*) of 6.0 indicates the wood cement particleboard has a higher energy dissipation capacity comparing with steel fiber reinforced concrete that has a toughness index of 5.0. Therefore, the wood–cement particleboard can be used where the energy dissipation property is desired.

CHAPTER 4

COMPRESSIVE BEHAVIOR OF WOOD-CEMENT PARTICLEBOARD

4.1 Introduction

Wood-cement particle composites used as structural members in building construction must often carry compressive loads. It is therefore necessary to characterize the properties of the composites under compression. The flexural properties of the wood-cement composites have been investigated extensively. Very little information is available on the compressive properties of cement bonded wood particle composites. The use of wood-cement particle bricks in load bearing walls requires information on compressive load-deformation and toughness. In most case, wood-cement composites were assumed to be isotropic, and the influence of particle orientation on mechanical properties has not been well characterized.

In this research, the compressive properties of the wood-cement particleboard in directions parallel and perpendicular to the wood fiber including the failure modes, stress-strain relations, and energy dissipation are investigated. A total of 22 specimens were manufactured using Portland cement (type I) and wood particles from CCA-treated southern yellow pine. The specimens were fabricated into rectangular short columns with different aspect ratios (width/height). The cement/wood ratios by weight of the specimens were 1.5 and 1.0.

4.2 Experimental Design

Wood-cement particleboard specimens with the aspect ratios shown in Table 4.1 were cut from thick particleboards (35 mm thick board with cement/wood ratio of 1.5 and 30 mm thick board with cement/wood ratio of 1.0). A schematic of the short column specimens is shown in Figure 4.1 and Figure 4.2 shows the loading directions. Table 4.1 shows the test matrix.

Table 4.1 Test Matrix for Determination of Properties

Cement/wood ratio		1.5		1.0
Aspect ratio (*h/d*)		2.0	3.0	2.0
Number of specimens	Parallel	4	4	3
	Perpendicular	4	4	3
Dimensions (mm)		17 x 17 x 34	11.7 x11.7 x 35	15 x15 x 30

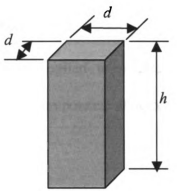

Figure 4.1 Short column specimens

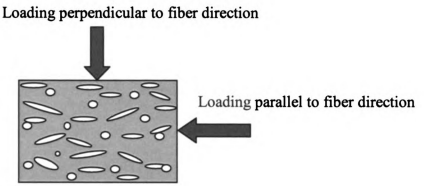

Figure 4.2 Loading directions

4.3 Compression Test

4.3.1 Test method

The compression tests were conducted at the Wood Technology Laboratory in the Department of Forestry at Michigan State University using an INSTRON machine (Figure 4.3). A photograph of typical specimens are shown in Figure.4.4. The specimens were tested with load parallel and perpendicular to the board thickness. The procedures in ASTM D1037-78 (1996) were applied to evaluate the material properties of the laboratory manufactured particle composites. The compressive loading rate was is 0.06 inch/minute.

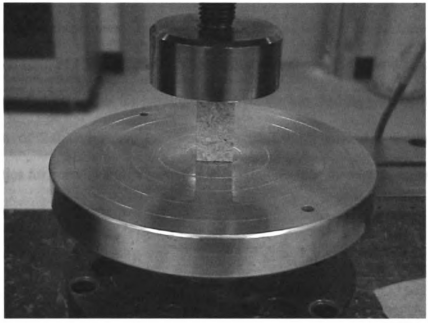

Figure 4.3 Compression test set-up on INSTRON test machine

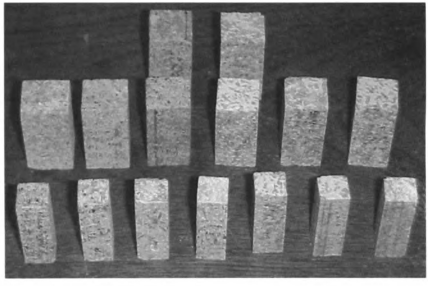

Figure 4.3 Compression specimens

4.3.2 Failure modes

Figure 4.5 shows the failure modes of specimens with an aspect ratio of 2.0 and a cement/wood ratio of 1.5 loaded parallel and perpendicular to the fiber directions. Figure 4.6 shows the failure modes for parallel and perpendicular loading on specimens with an aspect ratio of 2.0 and a cement/wood ratio of 1.0. Figure 4.7 shows the failure characteristics for parallel and perpendicular loading on specimens with an aspect ratio of 3.0 and a cement/wood ratio of 1.5.

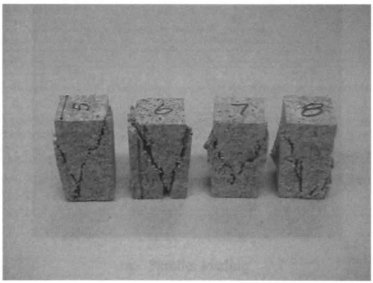

a. Parallel loading

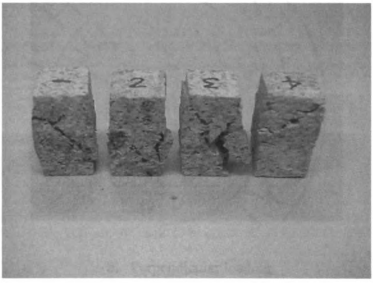

b. Perpendicular loading

Figure 4.5 Failure modes (h/d =2.0, cement/wood ratio = 1.5)

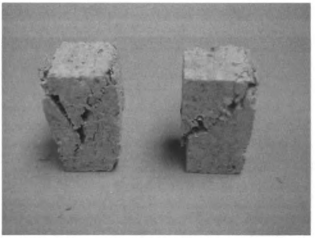

a. Parallel loading

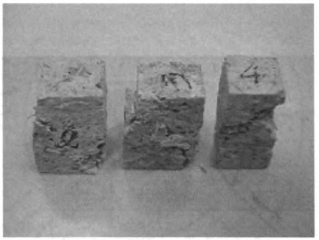

b. Perpendicular loading

Figure 4.6 Failure modes (h/d =2.0, cement/wood ratio = 1.0)

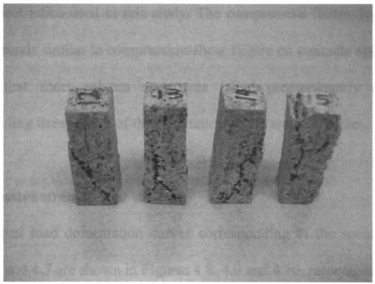

a. Parallel loading

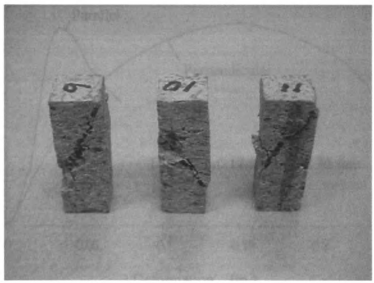

b. Perpendicular loading

Figure 4.7 Failure modes (h/d =3.0, cement/wood ratio = 1.5)

The failure modes on all samples were independent of the cement to wood ratios and column aspect ratios used in this study. The compressive failure typically occurred along diagonal bands similar to compression-shear failure on concrete specimens. It may be concluded that short column specimens failed predominantly in shear under compressive loading irrespective of the orientation of the wood particles.

4.3.3 Compressive strength and stiffness

The typical load deformation curves corresponding to the specimens shown in Figures 4.5, 4.6 and 4.7 are shown in Figures 4.8, 4.9 and 4.10, respectively.

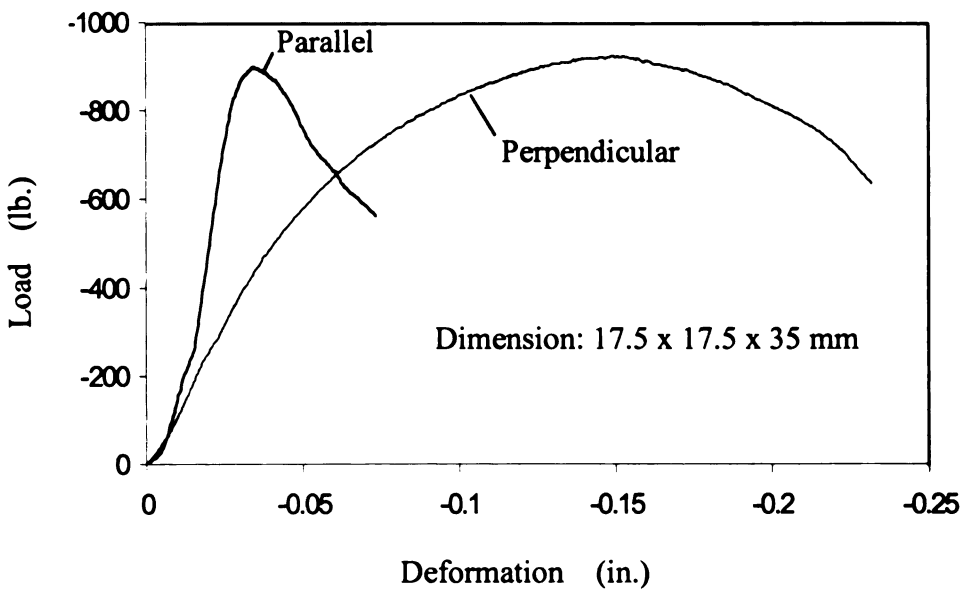

Figure 4.8 Load-deformation curve (h/d = 2.0, cement/wood = 1.5)

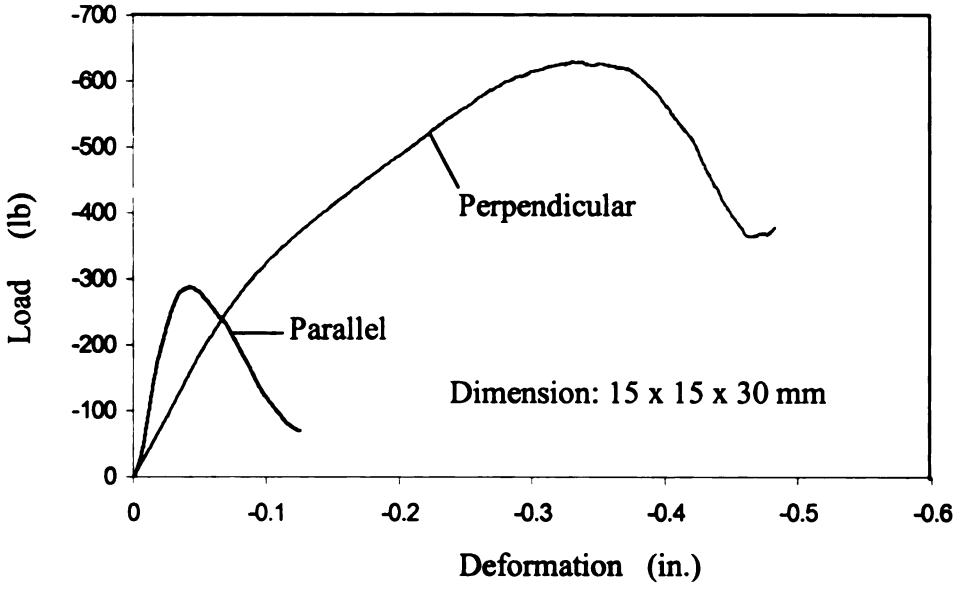

Figure 4.9 Load deformation curves (h/d = 2.0, cement/wood =1.0)

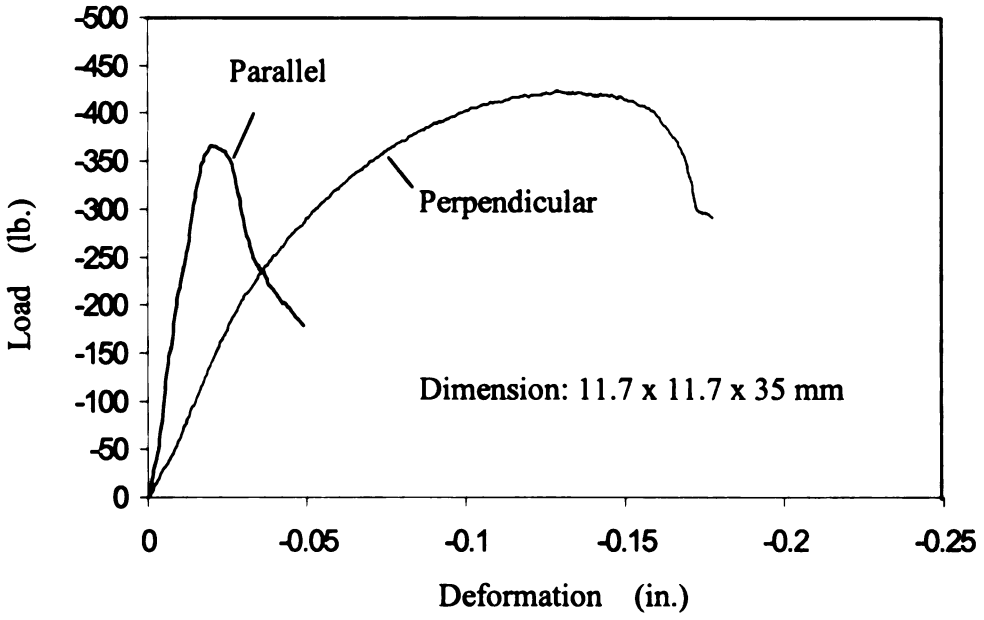

Figure 4.10 Load deformation curves (h/d = 3.0, cement/wood =1.5)

The load-deformation curves obtained in the tests display significant nonlinearity, and indicate that the wood-cement particleboard has the capability to absorb energy. Further, the mechanical properties are not isotropic and indicate directional dependencies. The directional properties are due to the alignment of wood particles caused by pressing during the manufacturing process.

Three significant observations are made:

(1) Under compression WCPB is much stiffer in the direction parallel to the particle fiber than in the perpendicular direction;

(2) The deformation of the specimens in the direction perpendicular to particle orientation is much larger than in the parallel direction;

(3) For an h/d ratio of 2.0, the compressive strength of specimens with cement to wood ratio of 1.5 was higher than that of specimens with a cement/wood ratio of 1.0 for both loading directions.

The compressive properties of WCPB and normal concrete are shown in Table 4.2. The compressive strength of WCPC was comparable to that of normal concrete, but the strains at maximum stress and at failure were much larger than that of normal concrete. The values in Table 4.2 indicate that the highest strength for WCPB occurred when the cement/wood ratio was 1.5, the specimen aspect ratio (h/d) was 2.0, and the loading direction was parallel to the fiber direction. For this case the compressive strength of WCPB is comparable to that of normal concrete and the strain at peak stress is ten times larger than that for concrete.

Table 4.2 Compressive Strength and Strain at Peak Stress for WCPB and Normal Concrete

Material	*h/d*	C/W	Loading Direction	Mean		Std. Dev	
				Strength	Strain	Strength	Strain
WCPB	2.0	1.5	//	2600	0.023	243	0.002
			⊥	2511	0.123	221	0.019
WCPB	2.0	1.0	//	713	0.041	67	0.005
			⊥	1808	0.284	192	0.032
WCPB	3.0	1.5	//	1650	0.013	154	0.002
			⊥	2060	0.094	189	0.013
Concrete	–	–	–	3000	0.002	–	–

Note: h/d=aspect ratio; C/W=cement/wood ratio; // = parallel to wood fiber direction; ⊥ =Perpendicular to wood fiber direction; Strength=compressive strength; Strain=strain at peak stress; Concrete=normal concrete.

The compressive strength for specimens loaded perpendicular to the fiber direction was smaller than that for specimens loaded parallel to the fiber direction in some cases and larger for other cases. The strain at peak stress was much larger when specimens were loaded perpendicular to the fiber direction than when they were loaded parallel to the fiber direction and 45 to 140 times larger than for normal concrete. The difference in properties for columns with aspect ratios of 2.0 and 3.0 may be attributed to the likelihood of eccentric loading for the longer specimens.

The ability of WCPB to sustain large plastic deformations compared to normal concrete implies that it has a strong potential to dissipate energy.

Table 4.3 shows the mean and standard deviation of the stiffness of the wood-cement particleboard under compression load. The stiffnesses of the WCPB are three to four times higher when loaded parallel to the fiber direction than when loaded perpendicular to the fiber direction. Both stiffnesses are three to four times larger for a cement/wood ratio of 1.5 compared to those for a cement/wood ratio of 1.0.

Table 4.3 Stiffness of Wood-Cement Particleboard

Material	h/d	C/W	Loading Direction	Mean	St. Dev
WCPB	2.0	1.5	//	1178	96
			⊥	400	23
WCPB	2.0	1.0	//	402	34
			⊥	110	13

Notes: // = parallel to wood fiber direction; ⊥ = perpendicular to wood fiber direction, h/d=aspect ratio; C/W=cement wood ratio

4.3.4 Toughness

Toughness is a measure of the energy absorbed per unit area of material and is usually defined as the area under the load-deformation curve. ASTM C1018 is often used to calculate toughness indices. ASTM C1018 defines a set of toughness indices for fiber reinforced concrete, which are defined as the area under the load-deformation curve up to the deformations of 3, 5.5 and 10.5 times the deformation at first crack divided by the area under load-deformation curve up to the first crack. In the concrete industry, the toughness index of plain concrete is 1.0 and the toughness index of steel fiber reinforced concrete is about 5.0.

In this study the ASTM C1018 toughness index (I_5) is used to define the compressive toughness of wood-cement particleboard. The toughness index (I_5) is defined by the following equation:

$$I_5 = \frac{Area\ \ under\ \ the\ \ load - deformation\ \ curve\ \ up\ \ to\ \ 3\delta}{Area\ \ under\ \ the\ \ load - deformation\ \ up\ \ to\ \ \delta} \tag{4.1}$$

where, δ is the axial deformation up to the first crack.

Table 4.4 shows the calculated toughness index I_5 for WCPB with two cement/wood ratios under uniaxial compression. The calculated toughness index (I_5) of the WCPB is about 7.0. The toughness index I_5 is close to a constant irrespective of the loading direction because the defined 3δ area under the load-deformation curve can not cover the values of peak stress and strain at peak stress due to peak stress being too large.

Table 4.4 Compressive Toughness of Wood-Cement Particleboard

Material	C/W	Toughness I_5	
		Mean	St. Dev
WCPB	1.5	6.99	0.41
WCPB	1.0	7.03	0.37

Figure 4.11 appears to indicate that the energy dissipation ability of the WCPB perpendicular to the fiber direction is higher than that in the direction parallel to the fiber

direction. However, the toughness index I_5 was close to 7.0 irrespective of the loading direction.

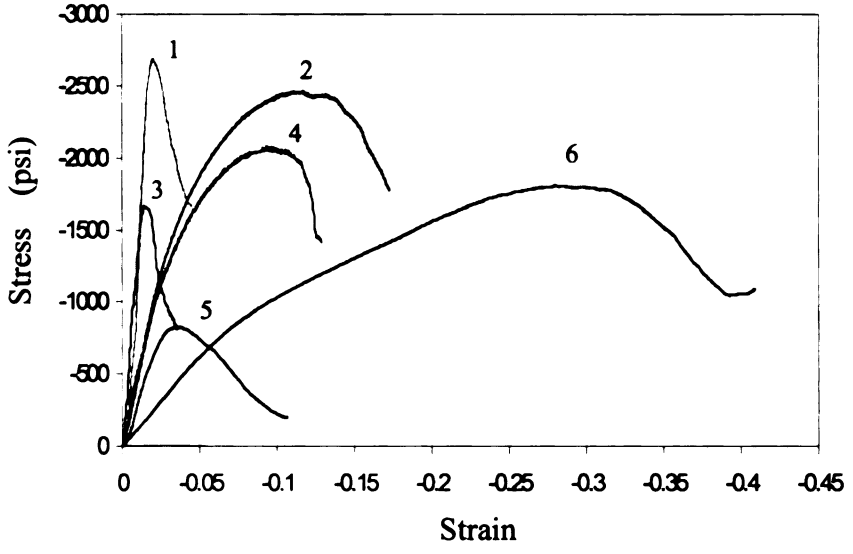

(1) Parallel, C/w =1.5, h/d = 2.0; (2) Perpendicular, C/w =1.5, h/d = 2.0.
(3) Parallel, C/w =1.5, h/d = 3.0. (4) Perpendicular, C/w =1.5, h/d = 3.0.
(5) Parallel, C/w =1.0, h/d = 2.0. (6) Perpendicular, C/w =1.0, h/d = 2.0.

Figure 4.11 Stress-strain relationships of the wood-cement particleboard

At the 95% level of confidence, the compressive strength, stiffness and toughness index of wood-cement particleboards with two different cement/wood ratios are shown in Figures 4.12 to 4.16.

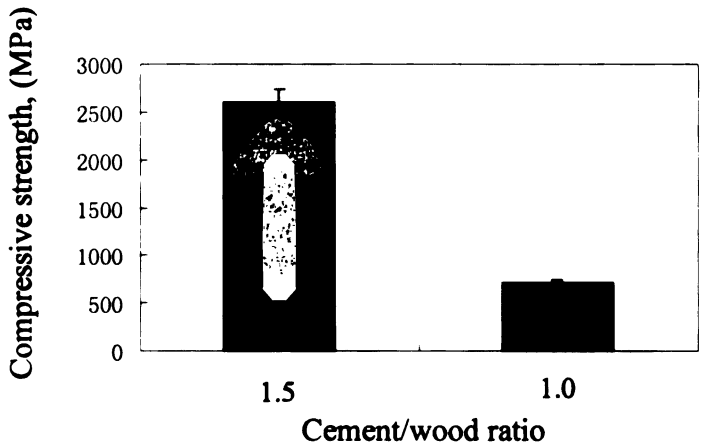

Figure 4.12 Compressive strength vs. cement/wood ratio (loading parallel to fiber)

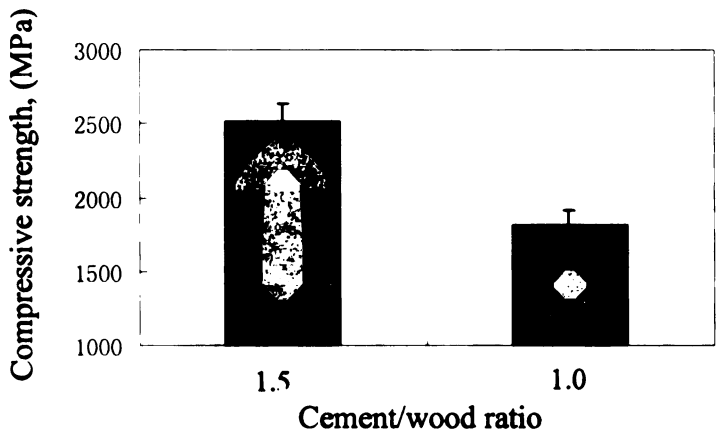

Figure 4.13 Compressive strength vs. cement/wood ratio (loading perpendicular to fiber)

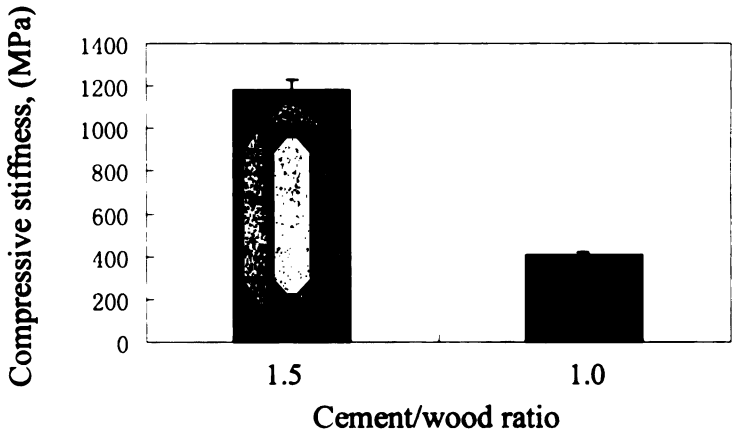

Figure 4.14 Compressive stiffness vs. cement/wood ratio (loading parallel to fiber)

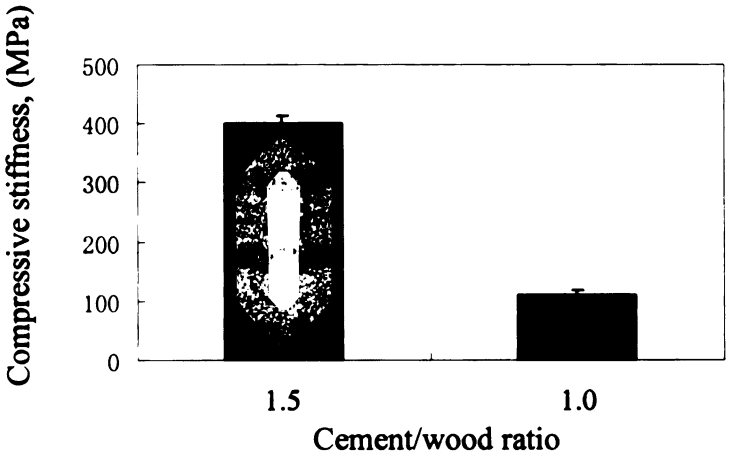

Figure 4.15 Compressive stiffness vs. cement/wood ratio (loading perpendicular to fiber)

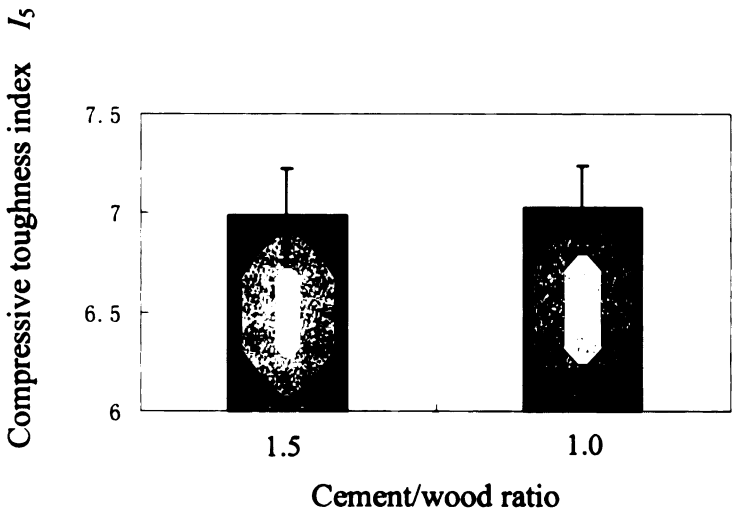

Figure 4.16 Compressive toughness index I_5 vs. cement/wood ratio (irrespective of loading direction)

4.4 Summary

Compressive tests conducted on WCPB show signifficant inelastic behavior. the composite specimen fails in shear under compressive loading parallel to or perpendicular to the wood fiber direction. Composites with a cement/wood ratio of 1.5 exhibited a compressive strength comparable to that of normal concrete, but the strain at peak load was ten to forty five times larger than the strain at peak load for normal concrete depending on the direction of the compressive loading. The ability of the composites to sustain such large plastic deformations suggests that WCPB has a strong potential to dissipate energy. The toughness index I_5 for the composites with either a cement/wood ratio of 1.5 or 1.0 was about 7.0, which is seven times larger than that of normal concrete.

This study suggests that CCA-treated wood removed from service can be used for manufacturing wood-cement particleboard for use in applications where compressive strength and energy dissipation are desirable properties.

CHAPTER 5

IMPACT TESTS ON WOOD-CEMENT PARTICLEBOARD

5.1 Introduction

Information about the impact response and energy dissipation of wood cement particle composites is needed if these composites are employed as structural members that may sustain impact loads. While the energy dissipation of wood-cement particle composites have been evaluated by measuring flexural and compressive toughness (Wolfe, 1996 and Hsu, 1995), no work appears to have been done using direct impact tests.

In this study, a falling ball impact test on wood-cement particleboard was conducted to investigate the impact response and energy dissipation behavior of the composite. In order to compare its response with those of more traditional building materials, such as wood and concrete, impact tests on concrete and on a wood board resting on concrete were also conducted.

These impact tests were evaluated by measuring the acceleration of a steel ball during impact. A high-precision accelerometer was employed in the impact test to record the acceleration of the steel ball when it impacted different materials.

A total of fifteen tests were conducted in this research for a steel ball impacting on the following surfaces: (1) wood-cement particleboard resting on concrete block, (2) wood board resting on concrete block, and (3) concrete block.

In addition to the direct falling ball impact tests, multi-stress tests on wood-cement composite tubes were conducted as well. One of the purposes of this test was to

investigate the material behavior of the wood-cement particleboard under a multi-stress state. Another was to investigate the effect of assuming the WCPB as an elasto-plastic isotropic material by comparing test results with the results of finite element simulation that use the isotropic material model presented in Chapter 6. The compressive tests were conducted using an MTS compression machine.

5.2 Falling Ball Impact Test

5.2.1 Impact test design

The falling ball impact test was designed to investigate the impact characteristics of WCPB. An accelerometer was mounted in the steel ball for recording the impact response of the ball as it impacted different materials. Three different materials were used: WCPB resting on a concrete block, wood board (wood grain parallel to horizontal plan) resting on a concrete block, and a plain concrete block.

The wood cement particleboard had a dimension of 120 x 120 x 35 mm (length x width x thickness) and a cement/wood ratio of 1.5. The wood board had a dimension of 120 x 120 x 35 mm and was made of CCA-treated southern yellow pine (the same kind of wood spices for the wood particles in the wood-cement particleboard). The concrete had a dimension of 150 x 150 x 150 mm and was made of normal concrete with a compressive strength of $f_c^{'}$ = 4000 psi. The steel ball was released from rest at a height, H, of 152 mm (or 6 inches) above the impact surface.

Figure 5.1 shows schematics of the impact tests. The test matrix detailing the number of specimens and specimen dimensions are given in Table 5.1.

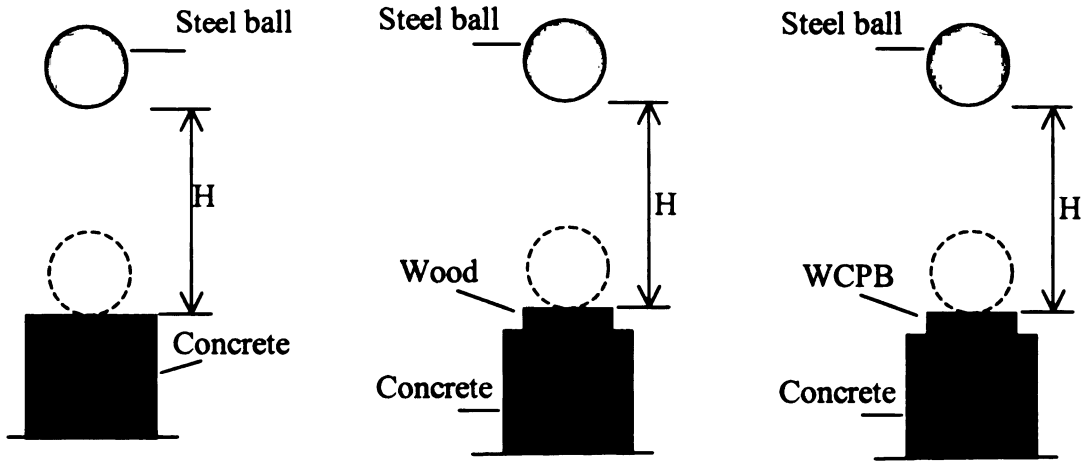

a. Impact on concrete b. Impact on wood on concrete c. Impact on WCPB on concrete

Figure 5.1 Schematics of impact test

Table 5.1 Test Matrix for Impact Test

	Concrete	Wood on concrete	WCPB on Concrete
Numbers of Test Specimens	5	5	5
Dimensions, mm	150 x 150 x 150 (concrete)	120 x 120 x 35 (wood)	120 x 120 x 35 (WCPB)

5.2.2 Design of impact device

In order to conduct the impact test, a test device was designed and manufactured. The impact test device includes two parts: one is an impact steel ball mounted with an accelerometer, and the other is an electro-magnetic release mechanism that released the ball. Figure 5.2 is the release mechanism for the impact test.

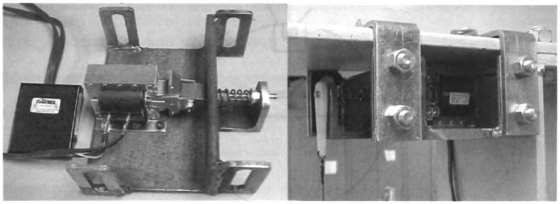

Figure 5.2 Release mechanism

The impact ball selected was a solid steel ball with a diameter of 107 mm and a weight of 5.0 kg. In order to record the acceleration of the steel ball during the impact, an accelerometer was mounted in the steel ball. A schematic of the steel ball with the mounted accelerometer is shown in Figure 5.3.

The accelerometer was recessed into the steel ball to protect it from damage during impact. Figure 5.4 shows photographs of the ball and mount.

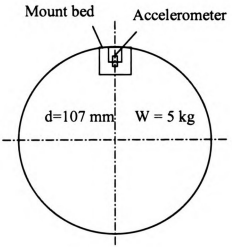

Figure 5.3 Schematic of the impact ball

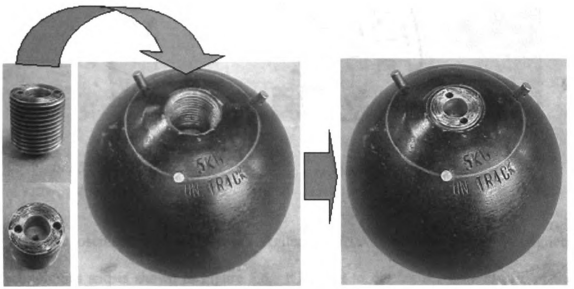

(a) (b) (c)

Mount Impact ball with threaded hole Impact ball with mount

Figure 5.4 Photographs of impact ball assembly

5.2.3 Impact data recording devices

The impact data was recorded using an accelerometer and oscilloscope. A model 353B12 piezoelectric accelerometer made by PCB Piezotronics, Inc was used. The accelerometer can measure the shock exposure experienced by space vehicles and cargo during stage separation. It may also be used to determine maximum impact acceleration levels experienced by vehicles and crash dummies. The accelerometer is a high frequency, quartz shear ICP accelerometer with a measurement range of $\pm$ 1000g ($\pm$ 4905 m/s^2). In addition, the accelerometer's size (Hex $\times$ height) is 7.1 x 14.7 (mm) and its weight is 1.5 gm (0.05 oz). Figure 5.5 shows a photo of the accelerometer.

Figure 5.5 353B12 accelerometer

Figure 5.6 Oscilloscope

The oscilloscope used was an Agilent 54620A instrument made by Agilent Technologies and is shown in Figure 5.6. It is used to display the time history of the acceleration and record the test data. The oscilloscope had the capability of storing recorded data on a computer floppy disk.

5.2.4 Impact test set up and results

The impact test on wood-cement particleboard resting on a concrete block was conducted for the purpose of determining the impact characteristics of the composite. Figure 5.7 shows the set-up for the impact test.

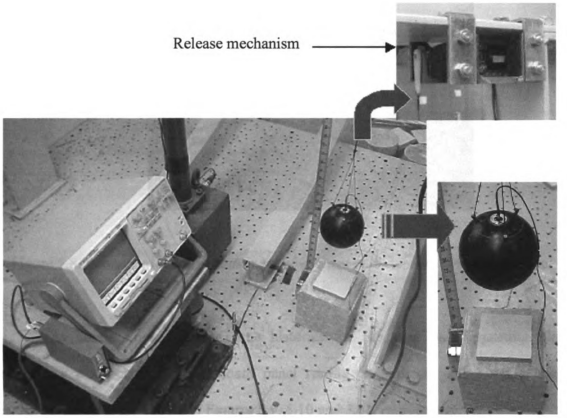

Figure 5.7 Impact test setup

Figure 5.8 shows the permanent deformation in the particleboard subsequent to impact by the steel ball. As shown in Figure 5.8, the impact caused an indentation of about 1.5 mm at the center of the impact area. Because the board's deformation is permanent, a plastic deformation occurs in the wood-cement particleboard due to the

impact of falling steel ball. The impact did not produce a crack at the bottom of the board.

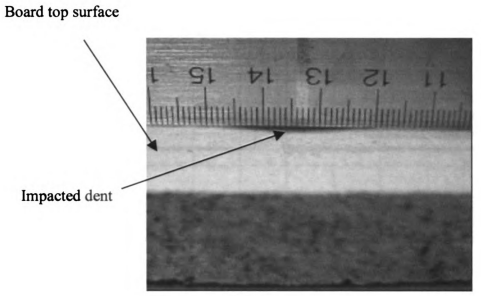

Figure 5.8. Permanent deformations in wood-cement particleboard following impact

The accelerometer voltage time histories for the steel ball impacting plain concrete, a wood-cement particleboard panel resting on concrete and a wood board resting on concrete are shown in Figures 5.9, 5.10 and 5.11, respectively.

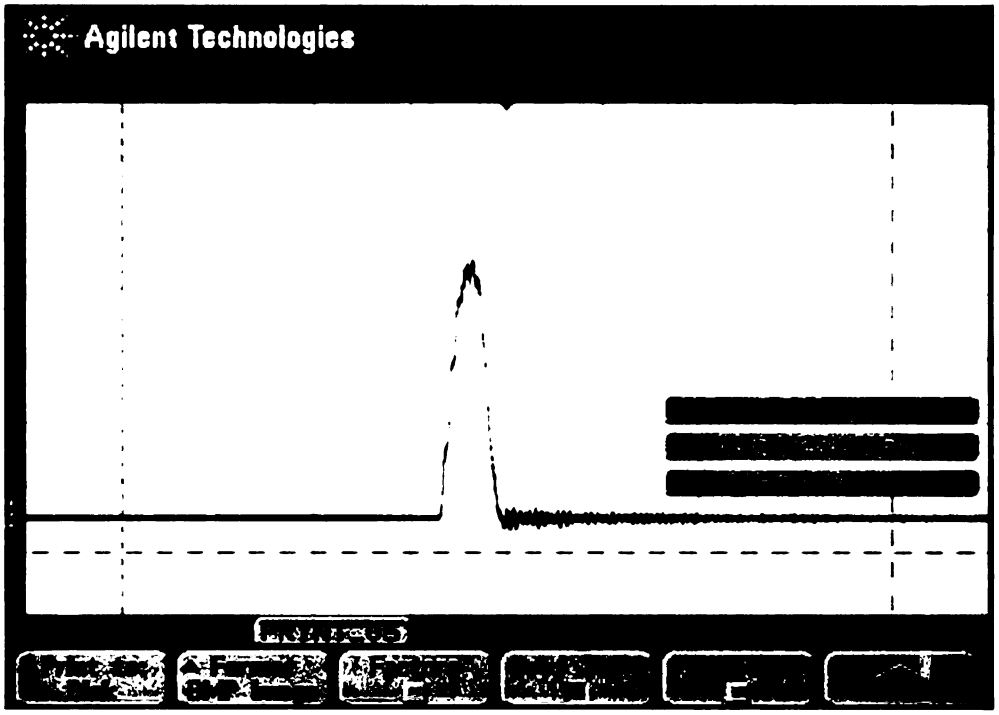

Figure 5.9 Voltage time history for impact on concrete

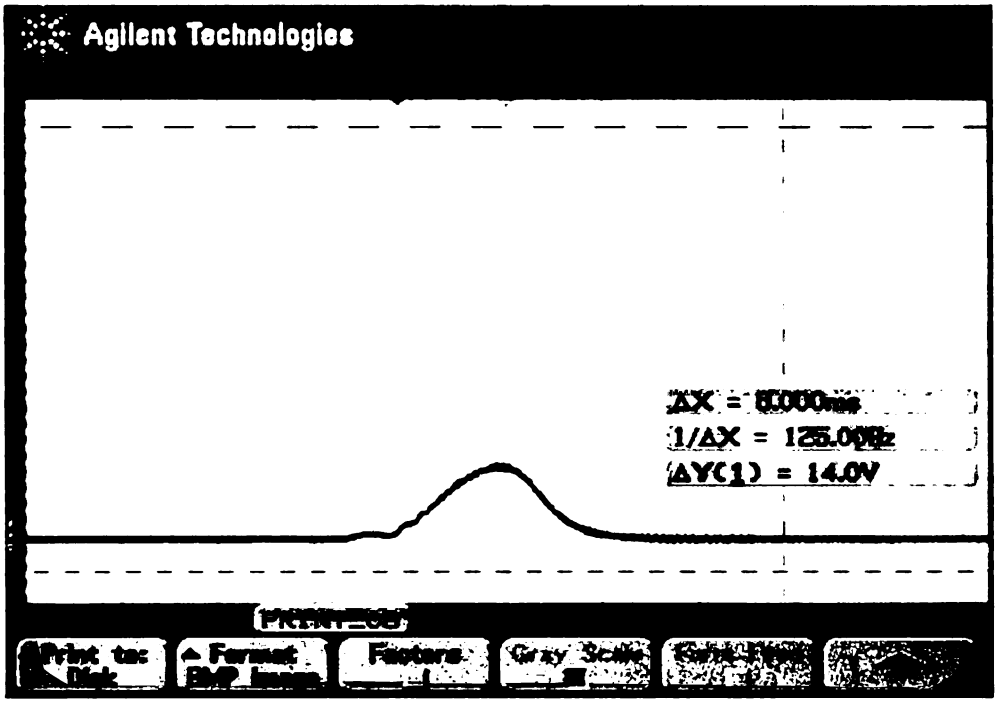

Figure 5.10 Voltage time history for impact WCPB resting on concrete

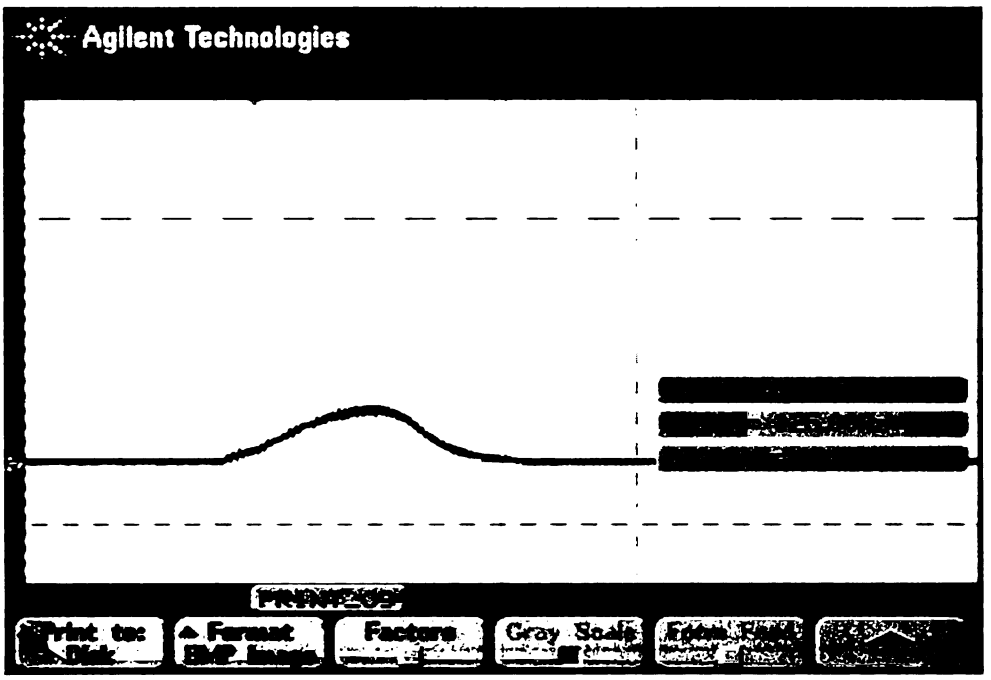

Figure 5.11 Voltage time history for impact on wood board resting on concrete

The conversion from voltage to acceleration is,

$$10.18 \text{ mV} = 1.00 \text{ g}$$

where $g = 9.81 \text{ m/s}^2$.

For the case of wood-cement particleboard resting on concrete, the accelerometer time histories are shown in Figure 5.12.

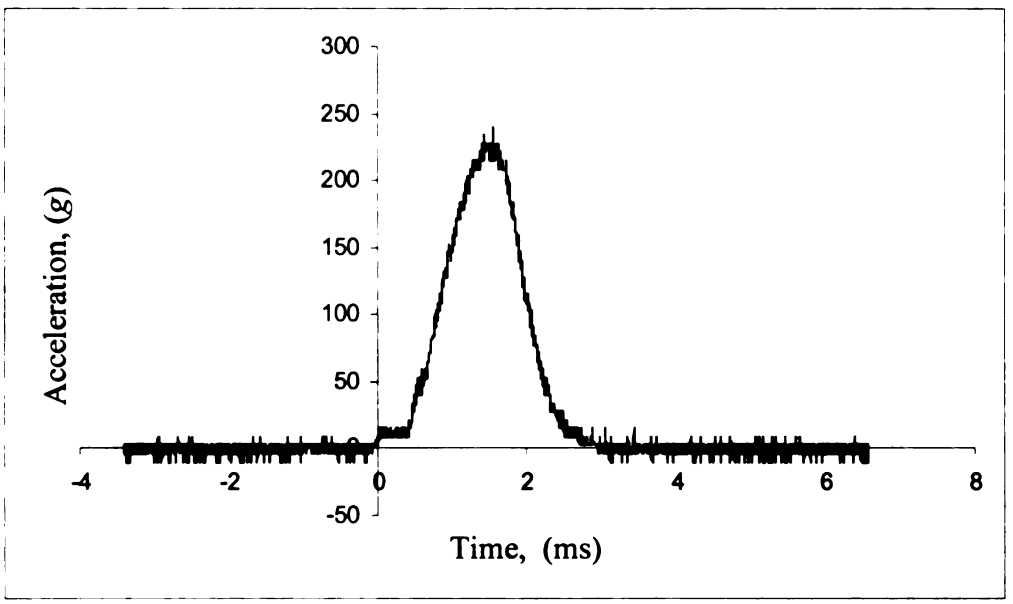

Figure 5.12 Acceleration time history of steel ball (WCPB on concrete)

The velocity time histories were computed from acceleration time histories through integration. The time was assumed to be zero at initial impact when the acceleration exceeded that due to gravity. Since the ball was released from rest from a height of six inches (152.4 mm) above the impact target, the velocity of the ball, V, at initial impact can be computed using the conservation of energy:

$$\frac{1}{2}mv_0^2 = mgH$$

Solving for v_0 yields

$$v_0 = \sqrt{2gH} = 17.2 \text{ (m/second)}$$

where m is the mass of the steel ball, g is the acceleration under gravity, and H =152 .4 mm. The velocity time histories are obtained through

$$v(t) = v_0 + \int_0^t a(t)dt\ ,\quad t \geq 0$$

where v_0 =17.2 m/s

The velocity time history corresponding to the acceleration time history in Figure 5.12 is shown in Figure 5.13.

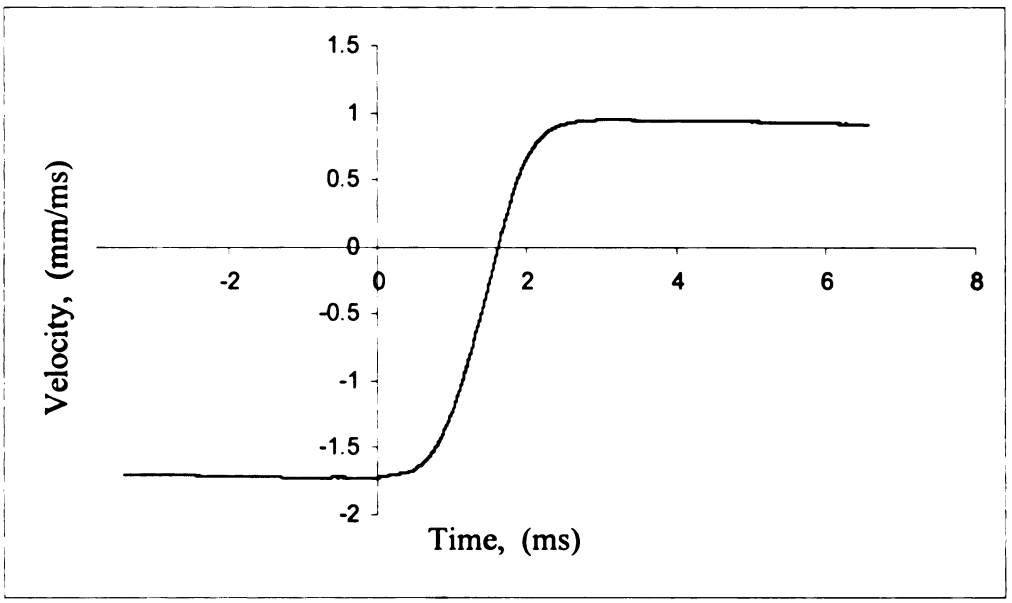

Figure 5.13 Velocity time history of the steel ball (WCPB on concrete)

Similarly, the displacement time histories of the steel ball were obtained by integration of the velocity time histories. Defining the displacement at the top of the impact surface to be zero, the displacement time histories can be obtained by the following equation.

$$d(t) = \int_0^t v(t)dt, \quad with \quad d(0) = 0$$

The displacement time history corresponding to the velocity time history in Figure 5.13 is shown in Figure 5.14.

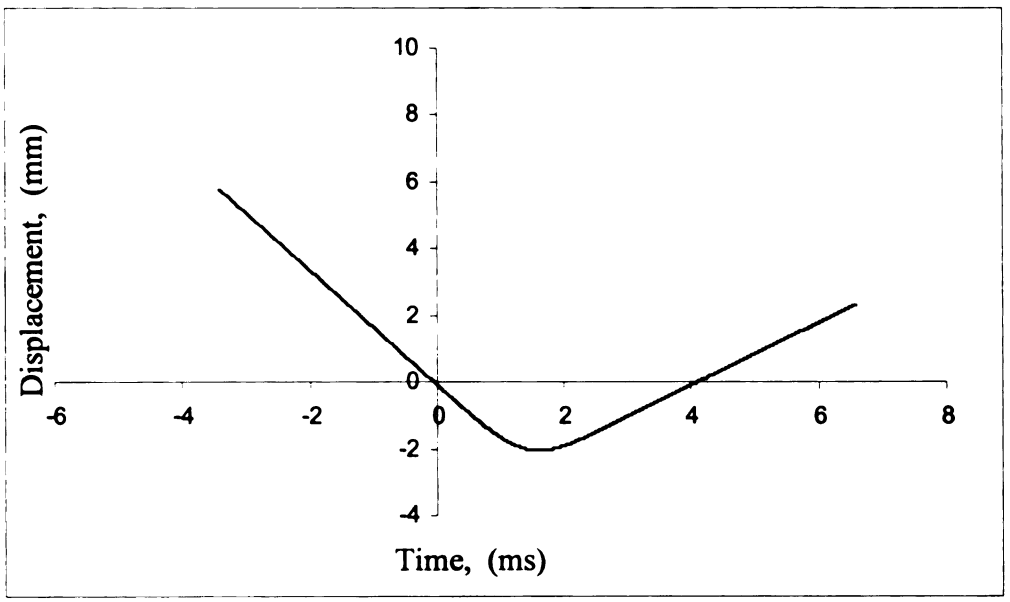

Figure 5.14 Displacement time history of the steel ball (WCPB on concrete)

Figure 5.15 compares the acceleration time histories of the steel ball impacting on wood-cement particleboard resting on concrete, concrete and wood board resting on concrete.

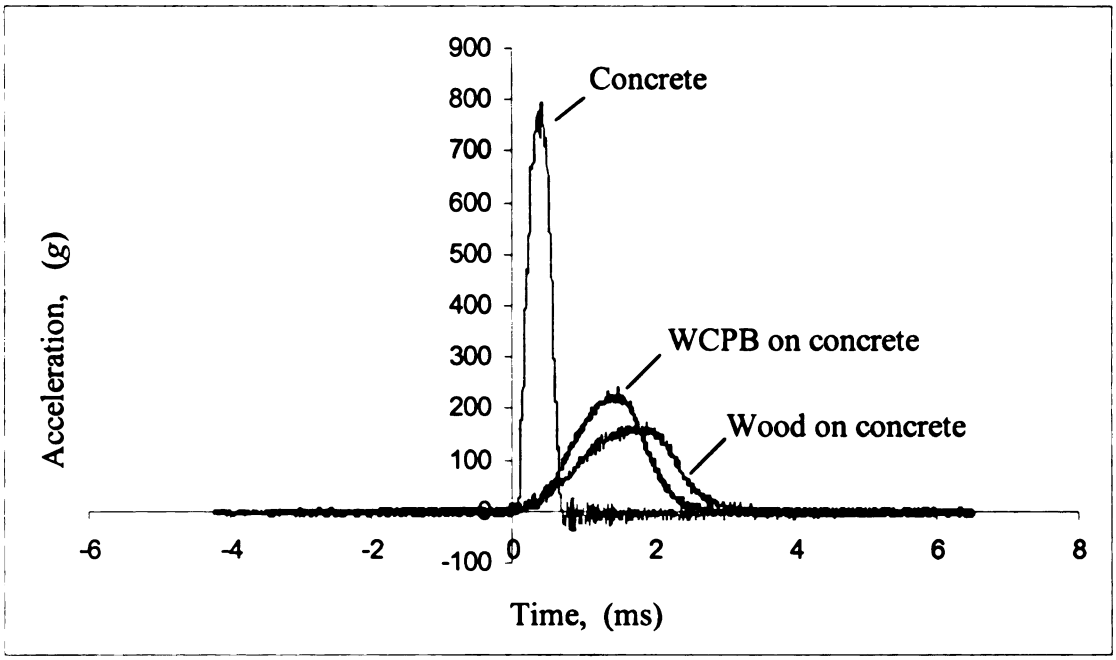

Figure 5.15 Acceleration time histories of steel ball impacting different surfaces

In Figures 5.15, the maximum acceleration of 800g occurs when the steel ball impacts concrete. The peak acceleration for impact on WCPB is 220g and that for impact on the wood board is 180g. The deceleration forces on the steel ball due to impact on the WCPB and the wood board are close, while the deceleration force for impact on concrete is about four times greater. The wood-cement particleboard layer reduces the impact acceleration, and hence the maximum impact deceleration force, by about 72%.

Figure 5.16 and Figure 5.17 showed the velocity and displacement time histories of the steel ball for the three different cases shown in Figure 5.1. In Figure 5.16, the peak rebound velocities of the steel ball for impact on concrete, WCPB and wood are 1.2, 0.9 and 0.78 (mm/ms), respectively. Therefore, the wood-cement particleboard layer reduces the peak rebound velocity by 25%. In Figure 5.17, the peak negative displacements (maximum deformation of specimen due to impact) for impact on concrete, WCPB and wood are 0.6, 1.6 and 2.0 (mm), respectively. It is the large deformation of wood and WCPB that results in the reductions in peak acceleration and rebound velocity of the steel ball.

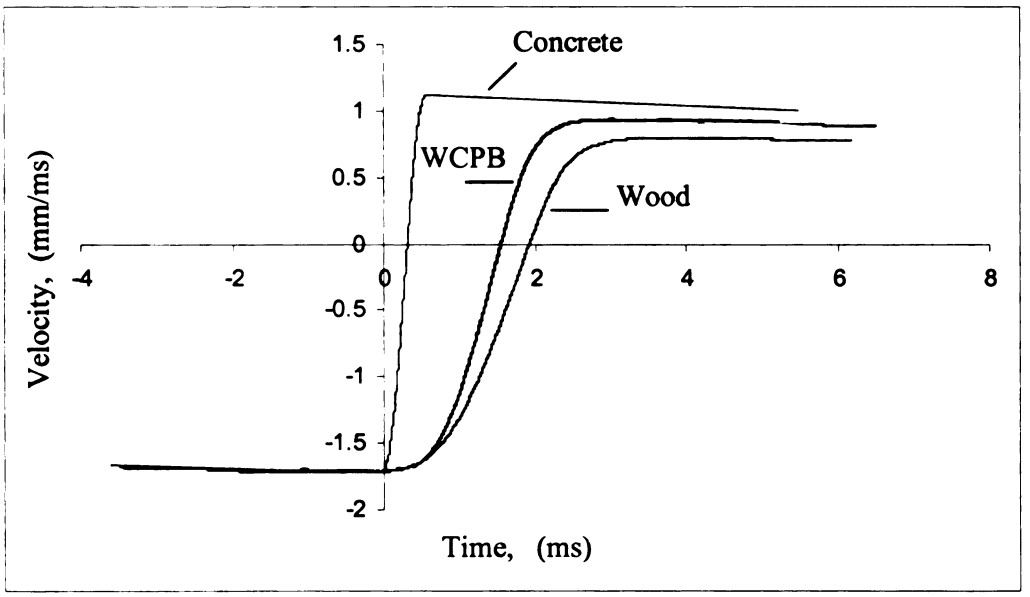

Figure 5.16 Velocity time histories of steel ball

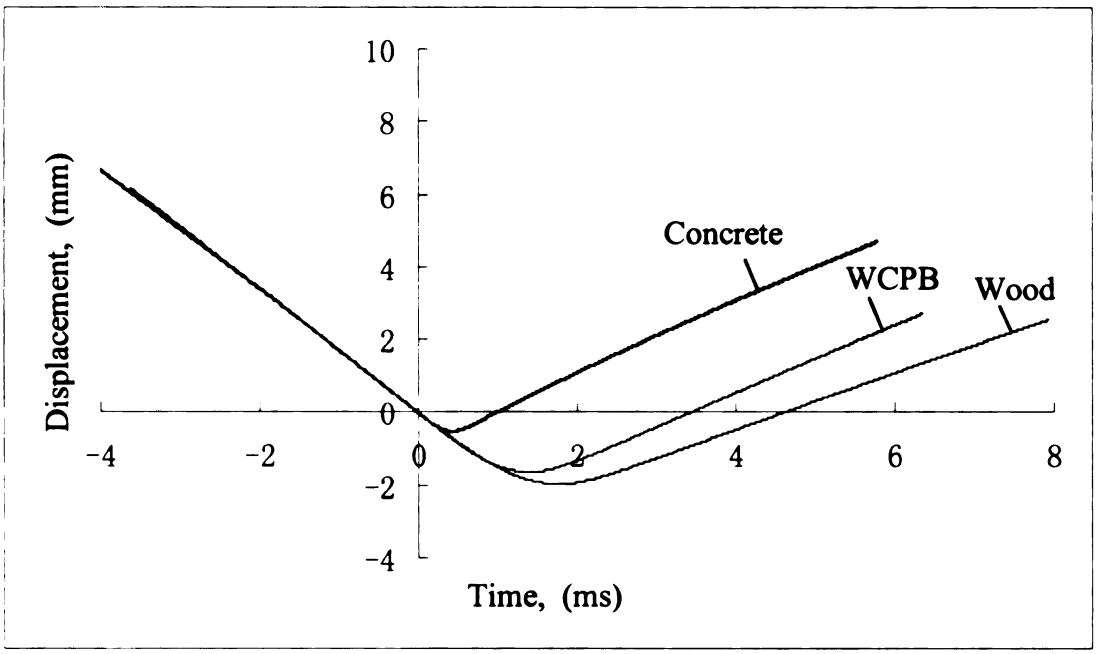

Figure 5.17 Displacement time histories of steel ball

5.3 Multi-Stress Test on Wood-Cement Particle Tube

The multi-stress test was conducted by applying a compressive load on a wood-cement composite ring. The purpose of this test was to verify the accuracy of simulations (described later) to predict the response of wood-cement particleboard tubes under impact. The motivation for using tubes is presented in Chapter 7.

In this research, the multi-stress test on the wood-cement particleboard ring was conducted to investigate the mechanical response of the ring. The WCPB ring was cut from a flat board with an outer diameter of 110 mm, inner diameter of 60 mm and thickness of 35 mm. The cement/wood ratio of the composite tube was 1.5.

Figure 5.18 shows the geometry of the test specimen. Two test specimens were manufactured and tested. The ring was cut from a flat 35 mm thick WCPB. The fibers therefore randomly oriented in the plane of the ring.

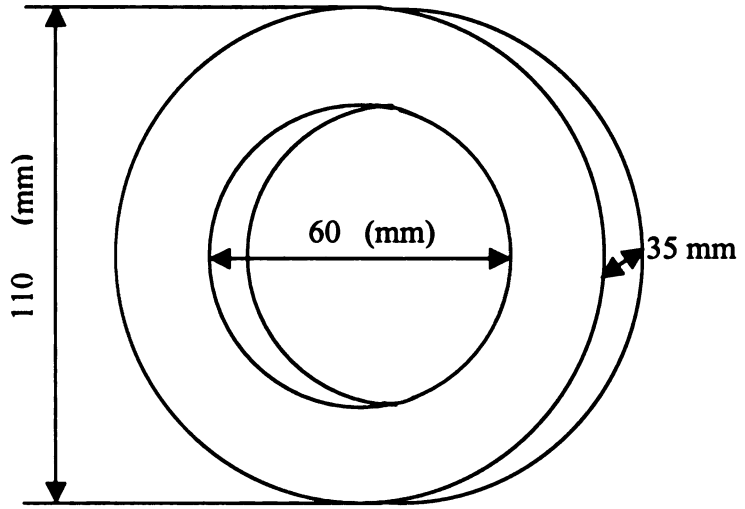

Figure 5.18 Geometry of specimen

5.3.1 Test results and analysis

The compressive loading was applied using an MTS machine with a loading speed of 0.01 mm/second. Two displacement measurements were recorded at the top of the specimen's external and internal circles as shown in Figure 5.19. The movement of the loading crosshead of the MTS machine was used as the displacement of the top of the test specimen. The loading direction was parallel to the cross section of the tube. The load-deformation curve was obtained in this test. The compressive test setup was shown in Figure 5.19.

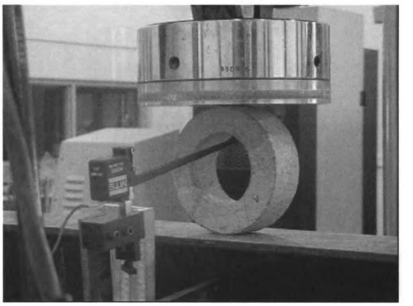

Figure 5.19 Compression test setup

The failure mode of the compression test is shown in Figure 5.20. The WCPB ring showed strong inelastic behavior. Even though the ring cracked and its shape deformed from a circle to an ellipse, it did not collapse.

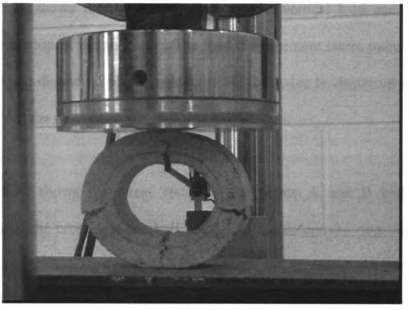

Figure 5.20 Compressive failure of WCPB ring

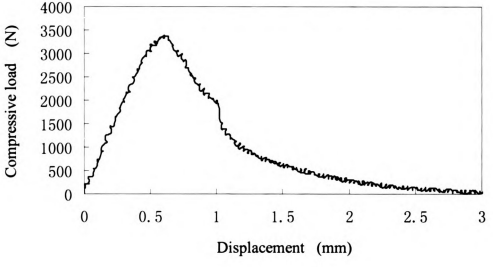

Figure 5.21 Load-displacement curve for multi-stress test on WCPB ring

Figure 5.21 shows the relationship between the vertical load and the vertical displacement at the top of the specimen. The load-displacement curve indicates that the ring displays elastic-degrading plastic behavior. The behavior is elastic up to a load of 2800 N after which the ring undergoes stiffness degradation.

Figure 5.22 shows the stress states at the points A and B and the stress distributions along the cross sections I, II and III in the composite ring under vertical compressive load. The stress distributions explain the failure cracks observed in Figure 5.20. Figure 5.22 shows that the composite ring is in a multi-stress state under vertical compression loading.

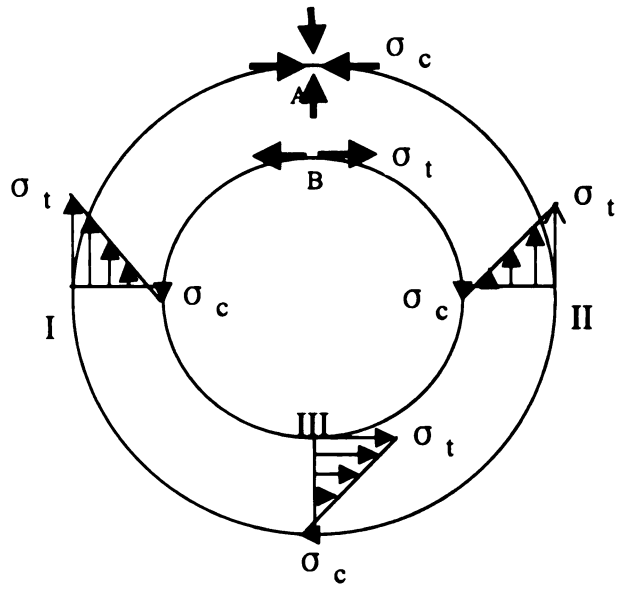

Figure 5.22 Stress state and stress distribution

5.4 Summary

Results from a falling ball impact test shows that wood-cement particleboard possesses good energy dissipation characteristics. The reduction in the impact force when the steel ball impacts WCPB resting on concrete is similar to that for impact on a wood board resting on concrete. Compared with the steel ball impacting a concrete block, the wood-cement particleboard resting on concrete reduced the impact acceleration of the steel ball, and hence the maximum impact deceleration force, by about 72%. The ability of the WCPB to reduce such a large portion of the impact deceleration force suggests that WCPB has a strong potential to dissipate energy.

The multi-stress test conducted on wood-cement particleboard ring samples showed that the rings display elastic-degrading plastic behavior similar to the behavior described in Section 3.3.3 for flexural specimens.

CHAPTER 6

VALIDATION OF MATERIAL MODEL FOR WOOD-CEMENT PARTICLEBOARD

6.1 Introduction

Finite element simulation of the falling ball impact test was performed to validate the ability of the material models in LS-DYNA to adequately represent wood-cement particleboard and concrete. If the simulations is successful, then preliminary studies on the impact of a vehicle with a concrete crash barrier enhanced with wood-cement particleboard panels can be performed using finite element simulation.

6.2 Finite Element Modeling of Falling Ball Impact Test

One of the important tasks in finite element simulation is finite element modeling. The quality of modeling directly affects to the accuracy of the results of the finite element simulation. The quality of modeling depends on many features, such as the power and flexibility of the modeling software, element modeling, material modeling, contact modeling and so on.

6.2.1 Modeling software

In the simulation study, four commercial software packages were used. LS-DYNA (Hallquist, 1999) is used for the impact analysis. The description of LS-DYNA was presented in Section 2.13. HyperMesh (Altair Engineering, 1999) was used as a

preprocessor to develop the finite element model. HyperGraphic (Atair Engineering, 1999) and LS-POST (LSTC, 2002) were used for post-processing. LS-DYNA and LS-POST are the products of Livermore Software Technology Corporation. HyperMesh and HyperGraphic are the products of Altair Engineering, Inc.

6.2.2 Element modeling

The steel ball, wood-cement particleboard and concrete were modeled with 8-node hexahedron solid elements.

6.2.3 Material modeling

In nonlinear finite element analysis of vehicle-barrier crashes, the principal challenge is the capability of the material constitutive models to represent a realistic response of the barrier under impact loading. In this study, concrete, wood-cement particleboard and steel were modeled with the material models available in LS-DYNA.

6.2.3.1 Modeling concrete

LS-DYNA offers several concrete material models, Material Model 16 (MAT_PSEUDO_TENSOR) is a model with the minimum required input data (Hallquist, 1999).

Material Model 16 (MAT_PSEUDO_TENSOR) is a pseudo-tensor geological model with an option for reinforcement. The model offers two major modes: a simple pressure-dependent Mohr-Coulomb yield surface with the Tresca limit, and two "yield versus pressure" functions with the capability to transit from one curve to another. The

latter one is used with the damage scale option as suggested in the User Manual (Hallquist, 1999). The equation of state (EOS) type 8 is used, which describes the volumetric response of the material. In this study, two-yield surface versus pressure criteria were employed for modeling the concrete.

Material Model 16 is based on the stress-strain relation of concrete under hydrostatic compression and a two yield surface limit. LS-DYNA uses a tri-linear relation between hydrostatic stress and volumetric strain to model the concrete behavior under hydrostatic compression. Figure 6.1 depicts the stress-strain relation adopted in LS-DYNA.

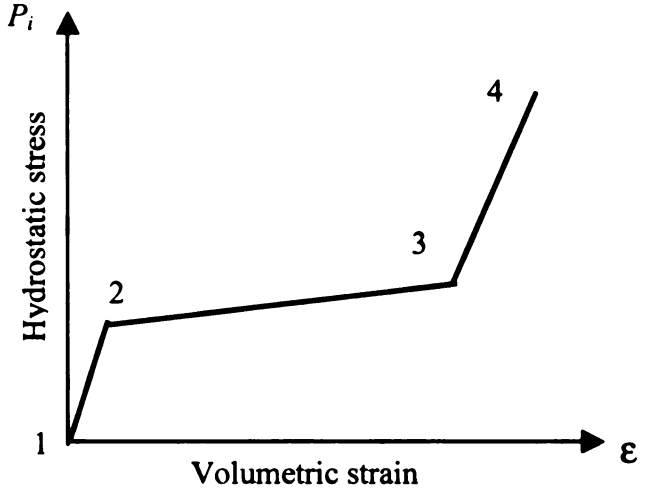

Figure 6.1 Hydrostatic stress vs. volumetric strain of concrete (schwer, 2001)

The following algorithm for generating the default EOS (Equation of State) parameters is used to determine the pressure and volume strain pairs, and an associated unloading bulk modulus for each of the four points comprising the pressure-volume curve (Shewer, 2002).

Table 6.1 Equation of State Algorithm for Generic Concrete (Shewer, 2002).

Point	Bulk Unloading K_{Ui}	Pressure P_i	Volume Strain ε_{vi}
1	$E/[3(1-2\nu)]$	0	0
2	$120f_c'$	$0.2f_c'$	$-P_2/K_{U1}$
3	$300f_c'$	$P_2-K_{U2}(\varepsilon_{v3}-\varepsilon_{v2})$	-0.068
4		$P_3-K_{U3}(\varepsilon_{v4}-\varepsilon_{v3})$	-0.10

The bulk unloading moduli are further modified to assure that the largest unloading modulus is associated with the last point of the curve:

$$\begin{aligned} K_{U4} &= \max(K_{U1}, K_{U3}) \\ K_{U3} &= K_{U4} \\ K_{U2} &= K_{U1} \end{aligned} \tag{6.1}$$

and then only the elastic K_{U1} and largest unloading moduli K_{U4} are retained in the generated EOS.

The elastic modulus of concrete was estimated from the formula provided by the American Concrete Institute. The estimate of Young's modulus for concrete, for a normal weight density of 145 lbf/ft^3, is given by the formula

$$E = 57{,}000\sqrt{f_c'}\ psi \tag{6.2}$$

and typical values of Poisson's ratio for concrete range from 0.15 to 0.2. In this study, a Poisson ratio of 0.2 was used (Nilson, 1991).

LS-DYNA also uses the two-yield surface limit shown in Figure 6.2 as a failure criteria. In Figure 6.2, the lower curve represents the initial yield surface and the upper curve represents the evolution of the yield surface due to concrete hardening.

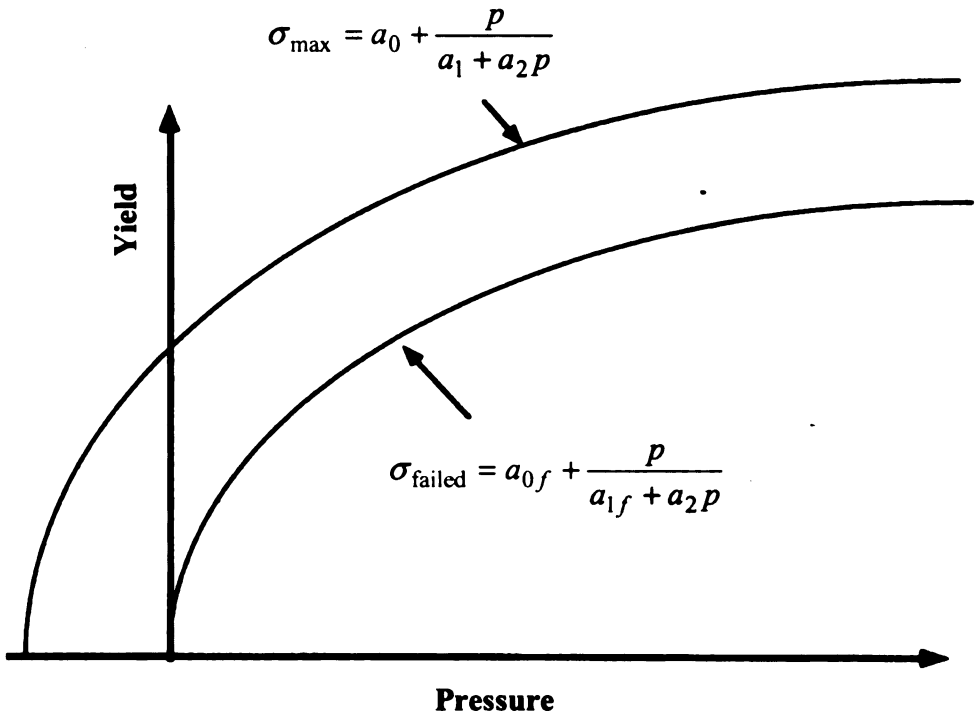

Figure 6.2 Yield stress vs. mean stress for concrete under hydrostatic compression

The input parameters of the concrete material used in this study are given in Table 6.2.

Table 6.2 Concrete Material Parameters

Density	2.4 (g/cm^3)
Young's Modulus	21526 (MPa)
Poisson's Ratio	0.2
Compressive Strength	20 (MPa)

6.2.3.2 Modeling wood-cement particleboard

Wood-cement particleboard is modeled as an isotropic material due to the small size of the wood particles. This simplifying assumption is used even though wood cement particleboard has directional properties.

Material Model 24 (MAT_PIECEWISE_LINEAR_PLASTICITY) was selected to model wood-cement particleboard. Material Model 24 is suited for elasto-plastic material with an arbitrary stress-strain curve or tabulated stress-strain data (Hallquist, 1999).

In this material model, the stress-strain pairs are taken from test data and failure is characterized by a maximum plastic strain limit. The stress-strain curve is defined by the effective stress and effective plastic strain. The effective plastic strain is a true plastic strain equal to the total strain minus the elastic strain, while the effective stress is the true stress corresponding to the effective plastic strain.

Figure 6.3 shows a typical piecewise linear curve of effective stress vs. effective plastic strain. The piecewise linear curve defines the yield stress versus the effective plastic strain. A nonzero yield stress is defined when the plastic strain is zero.

Figure 6.3 Effective stress vs. effective plastic strain curve (Hallquist, 1999).

The engineering stress-strain curve does not give a true indication of the deformation characteristics of a material because it is based entirely on the original dimensions of the specimen, and these dimensions change continuously during the test.

The true stress σ is expressed in terms of engineering stress by

$$\sigma = s(e+1) \tag{6.3}$$

The true strain ε may be determined from the engineering or conventional strain e by

$$\varepsilon = \ln(e+1) \tag{6.4}$$

To find the curve of true stress and true plastic strain, three steps were taken.

First, derive engineering stresses and strains,

Engineering stress: $s = \frac{P}{A_0}$ (6.5)

Engineering strain: $e = \frac{L - L_0}{L_0}$ (6.6)

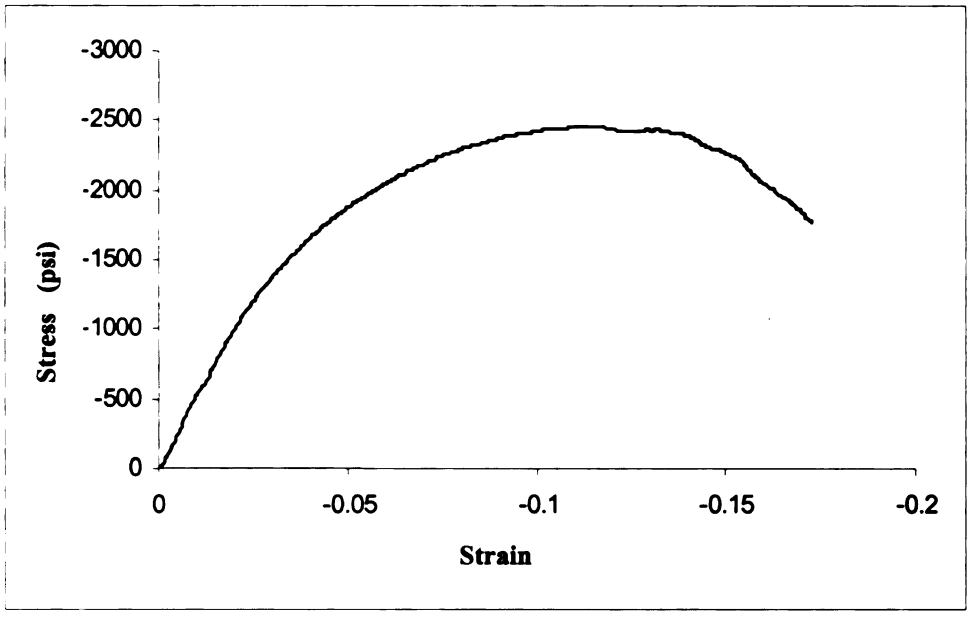

Figure 6.4 Engineering stress vs. engineering strain (WCPB)

Second, calculate the plastic strain,

Plastic strain: Plastic strain e_p = total strain (e) – elastic strain (e_e)

i.e. $e_p = \frac{L - L_0}{L_0} - \frac{s_y}{E} = \frac{L - L_0}{L_0} - \frac{P_y}{A_0 E}$ (6.7)

where e_p = plastic strain, s_y = yield stress, P_y = yield load, A_0 = original cross section area, L_0 = original length, and L = current length.

Third, using equation 6.3 and 6.4, calculate the effective stress (true stress) and effective plastic strain (true plastic strain) and make sure a nonzero yield stress is defined when the plastic strain is zero. Figure 6.5 shows the relation between effective stress and effective plastic strain.

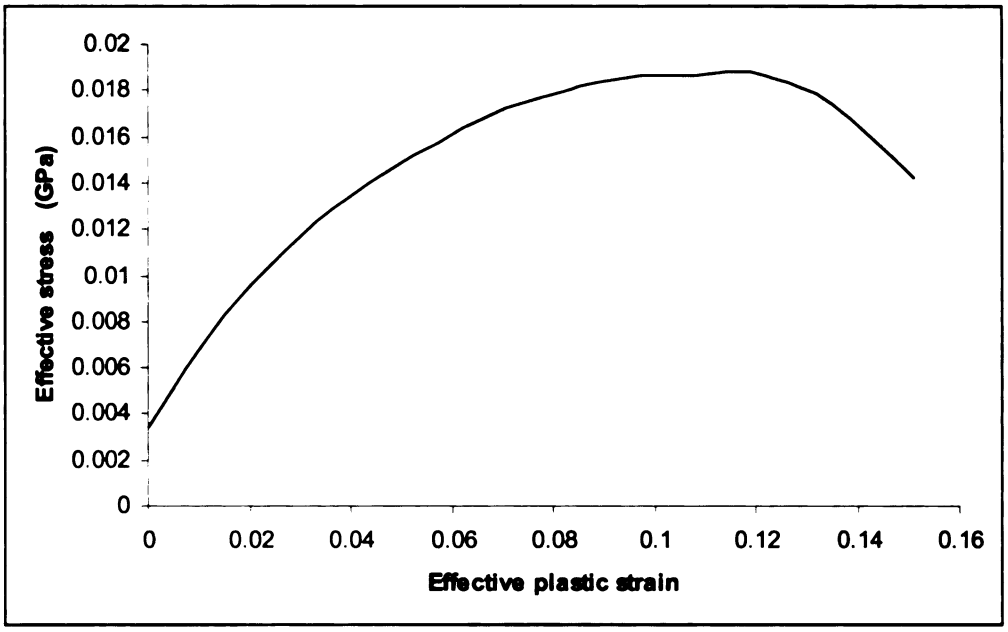

Figure 6.5 Effective stress vs. effective plastic strain (WCPB)

Table 6.3 shows the input data required for the material model of wood-cement particleboard in this simulation.

Table 6.3 WCPB Material Data

Density	1.044 (g/cm^3)
Young's Modulus*	400 (MPa)
Poisson's Ratio	0.2
Load curve	Shown in Figure 6.5
Yield stress (compressive)	17.2 (MPa)
Tensile cut off stress	11.2 (MPa)

* Young's Modulus is in the direction perpendicular to the board thickness.

6.2.3.3 Modeling steel

Steel material is often modeled with elastic, kinematic plastic or piecewise linear plasticity models. When the steel ball impacts the concrete block from 6 inches above the concrete, the maxiumum stress on the steel ball is well below the yield stress. Therefore, Material Model 1 (MAT_ELASTIC) was used to model the steel ball. The Materail Model 1 (MAT_ELASTIC) is a linear isotropic elastic material model (Hallquist, 1999). The material properties of the steel ball are listed in Table 6.4.

Table 6.4 Material Data for Steel Ball

Density	7.85	(g/cm^3)
Young's Modulus	210,000	(MPa)
Poisson's Ratio	0.2	
Yield Strength	200	(MPa)

6.2.4 Contact modeling

The contact-surface algorithm in LS-DYNA is a penalty-based method. In the falling ball impact simulation, there is one kind of contact interaction: steel ball to the surface of the particleboard for the steel ball impacting the particleboard panel resting on a concrete block, or steel ball to the surface of concrete for the steel ball directly impacting the concrete block. The contact algorithms are set as follows:

- For the steel ball impacting the particleboard panel resting on a concrete block: 1). Set the particleboard's top surface as the master surface and the surface of steel ball as a slave surface; 2) Set the top surface of the concrete block as master surface and the bottom surface of the particleboard as the slave surface. The

nodes on the slave surface cannot penetrate through the master surface. In LS-DYNA, the Surface to Surface contact type was used.

- For the steel ball directly impacting the concrete block, set the top surface of concrete block as the master surface and the surface of the steel ball as a slave surface. The nodes on the slave surface cannot penetrate through the master surface. In LS-DYNA, the Surface to Surface contact type was used.

6.2.5 Boundary conditions

In the impact tests, the impact ball falls freely from a height of six inches (152.4 mm) above the impact target. Therefore, the initial velocity of the ball just prior to impact is 17.2 m/s. In addition, the constraint condition imposed on the concrete block is that the the nodes on the bottom of the concrete block are fixed as shown in Figure 6.6.

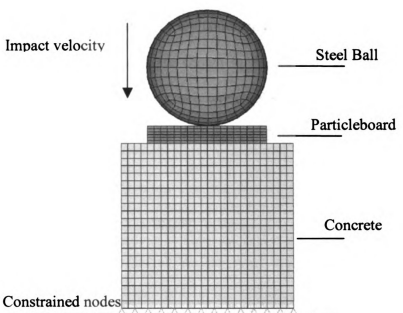

Figure 6.6 FE model and boundary conditions

6.2.6 Database output node

In order to compare the simulation results with the test results, in the simulation model the results were output at a node at the exact location of the accelerometer mounted within the steel ball. The output node location is shown in Figure 6.7.

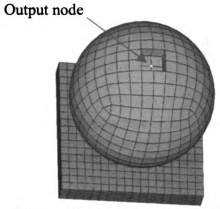

Figure 6.7 Output node location

6.2.7 Impact simulation and result anslysis

Two types of impact simulations were conducted as described above. The finite element models for these simulations are shown in Figure 6.8. The simulations were carried out on a multi-processor Sun Unix workstation located in the Division of Engineering Computing Services in the College of Engineering at Michigan State University.

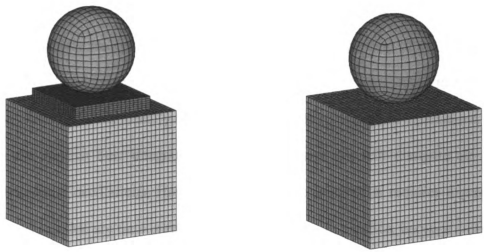

a. Ball impacting particleboard resting concrete b. Ball impacting concrete

Figure 6.8 Finite element models

All the following test and simulation results, such as accelerations, velocities and displacements, are in the vertical Z direction. Figure 6.9 shows the acceleration time histories of the steel ball from the impact test and simulation for impact on the concrete block. Figure 6.9 shows that the simualtion results have a very good agreement with the impact test results except that there is about a 7% difference in peak the acceleration between the test and simulation. The simulation results indicate that Mat_Pseudo_Tensor model can be effectively applied to model concrete material.

Figure 6.10 shows the acceleration time histories of steel ball from the impact test results and simulation for impact on WCPB resting on a concrete block. The figure shows that the simulation result matches the test result quite well, especially from the impact point to the peak acceleration. But, in the simulation results, the accelerations following the peak acceleration display spurious oscillations.

The spurious oscillations represent high frequency motions that the analysis model cannot acurately resolve and are mainly created by the algorithm of the analysis as well as the viscosity of the material. The explicit central difference method that is used in LS-DYNA does not automatically dissipate high frequency numerical oscillations. It is possible to use implicit time integration in LS-DYNA and this will dissipate the high frequency numerical oscillations. However, implicit time integration requires expensive iterative procedures that are time consuming and expensive. In practice, because a certain degree of spurious oscollation is not debilitating, employing explicit analysis and enforcing an artificial damping control to smooth the oscillations may be a good chice.

In this falling ball problem, an explict analysis is applied and the spurious oscillations were controlled with the LS-DYNA control command Control-Bulk-Viscosity. The parameters used in the control command were the LS-DYNA recommended default values related to sound wave propagation in general elasto-plastic materials. In Figure 6.10, the spurious oscillations are limited and the simulation results match the test results quite well.

In Figure 6.9, Figure 6.10, Figure 6.11 and Figure 6.12, $t = 0$ represents the moment the steel ball first touches the specimen's top surface. The measured acceleration time history was shifted in accordance with this. In Figure 6.12, the zero point in the displacement axis was defined at the specimen's top surface. Negative displacement represents the deformations of the particleboard after the steel ball hits the board's top surface in the downward direction.

Figure 6.11 and Figure 6.12 show the velocity and displacement time histories from the impact test and simulation for impact on the WCPB resting on a concrete block,

respectively. The simulation results match the results from the impact test quite well and demonstrate that the nonlinear finite element analysis code LS-DYNA can effective simulate the impact test on the wood-cement particleboard and that the wood–cement particleboard and concrete can be modeled reasonably by the LS-DYNA elasto-plastic material model (MAT_PIECEWISE_LINEAR_PLASTICITY) and geological material model (MAT_PSEUDO_TENSOR), respectively.

The conditions at t = 0 are therefore

$$a(0) = g, \quad v(0) = -17.2 \text{ m/s}, \quad d(0) = 0.$$

where a = acceleration, v = velocity, and d = displacement.

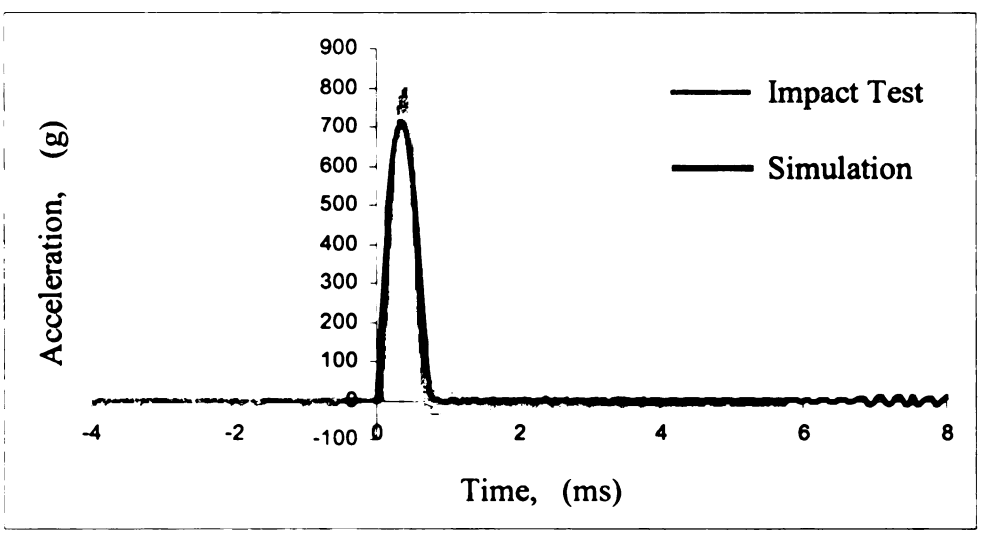

Figure 6.9 Acceleration time histories from impact test and simulation for impact on the concrete block

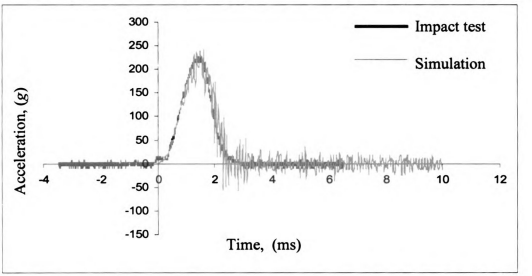

Figure 6.10 Acceleration time histories from impact test and simulation for impact on WCPB resting on a concrete block

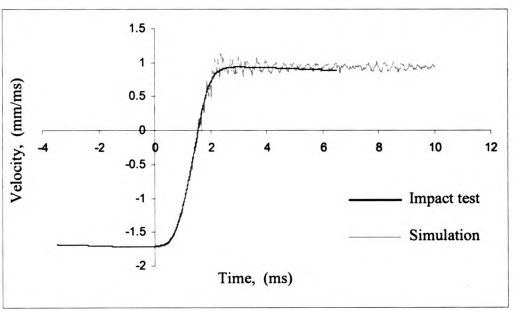

Figure 6.11 Velocity time histories from impact test and simulation (WCPB)

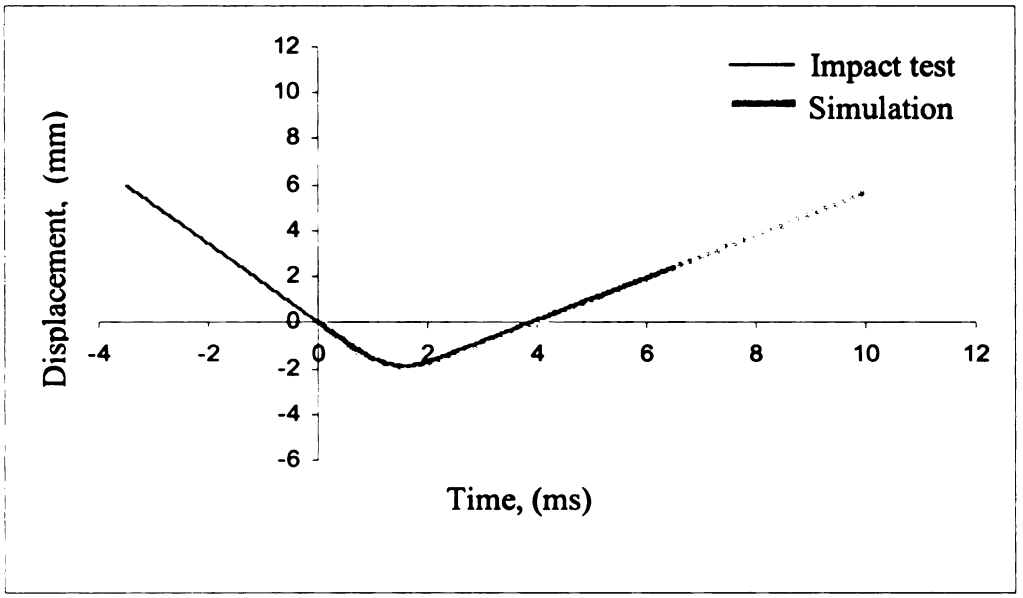

Figure 6.12 Displacement time histories from impact test and simulation (WCPB)

6.3 Finite Element Modeling of Multi-Stress Test

In order to verify that the material model in LS-DYNA can be used to model wood-cement particleboard that is subjected to a multi-stress state, the finite element simulation of the multi-stress test on the WCPB tube was conducted. The software of LS-DYNA, Hypermesh, and LS-POST were used for simulation, preprocessing and post-processing, respectively.

6.3.1 Element modeling

The wood-cement particleboard tube, loading cross head and supporting plate of the loading machine were modeled using 8-node solid elements. The finite element model is shown in Figure 6.13.

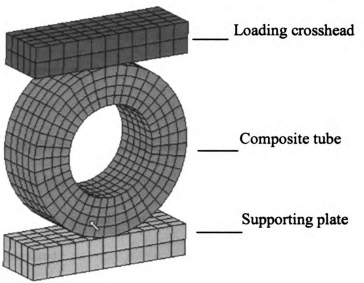

Figure 6.13 Finite element model

6.3.2 Material modeling

The wood-cement particleboard tube was modeled with Material Model 24 (MAT_PIECEWISE_LINEAR_PLASTICITY). The loading crosshead and supporting plate of the loading machine were modeled with Material Model 1 (MAT_ELASTIC).

6.3.3 Contact modeling

In the multi-stress test simulation, two contact interactions occurr between the loading machine and the testing specimen. As the composite tube deforms, the top and bottom surfaces of the composite tube contact with the surface of the loading crosshead and the surface of the supporting plate, respectively. The contact algorithms are set as follows:

- Set the top surface of the composite tube as the slave surface and the surface of the crosshead as the master surface. The nodes on the slave surface cannot penetrate through the master surface. In LS-DYNA, the Surface to Surface contact type was used.
- Set the bottom surface of the composite tube as the slave surface and the surface of the supporting plate as the master surface. The nodes on the slave surface cannot penetrate through the master surface. In LS-DYNA, the Surface to Surface contact type was used.

6.3.4 Boundary conditions

In this simulation, there are two different boundary conditions consisting of the loading velocity and support conditions. The velocity condition was set to the loading speed of 0.01 mm/second, and fixity was imposed on the nodes along the bottom of the supporting plate. The boundary conditions are shown in Figure 6.14.

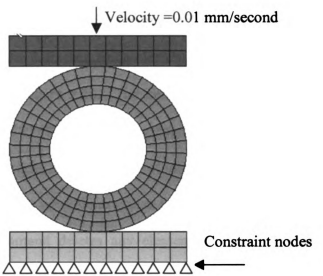

Figure 6.14 Boundary conditions

6.3.5 Database output node

In order to compare the simulation results with the test results, the simulation results were output at the node on the top surface of the tube that has initial contact with the crosshead. The output node location is shown in Figure 6.15.

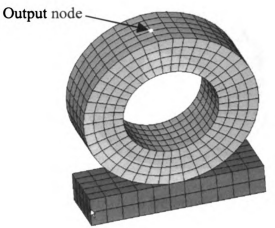

Figure 6.15 Location of output node

6.3.6 Multi-stress test simulation

Figure 6.16 shows the largest deformation of the finite element model in the simulation. The shape of the deformed finite element model is close to the shape of the deformed test specimen in Figure 5.20. The deformed finite element model does not show cracks. Because LS-DYNA uses a Lagrangian formulation in which the mesh moves with the material, cracks are generally not introduced in the finite element model without special treatment. It is possible to utilize the DELETE command to make cracks occur. The DELETE command deletes any elements in which elemental stresses or strains exceed specified limits. However, in this research the focus was on the deformed shape and the load-displacement curve of the finite element model, and the DELETE

command was not employed in the simulation. It should be noted that the analysis properly accounts for failure of the material (i.e., cracks) by reducing the stiffness of failed elements. Therefore, although cracks are not visible, the analysis properly accounts for their presence.

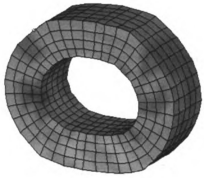

Figure 6.16 Deformed FE model

Figure 6.17 shows the load-displacement curves obtained from the compressive test and the simulation. The simulation results match the compressive test results quite well. The simulation results indicate that the elasto-plastic material model (MAT_PIECEWISE_LINEAR_PLASTICITY) adequately models the wood-cement particleboard under a multi-stress state even though the material is truly orthotropic.

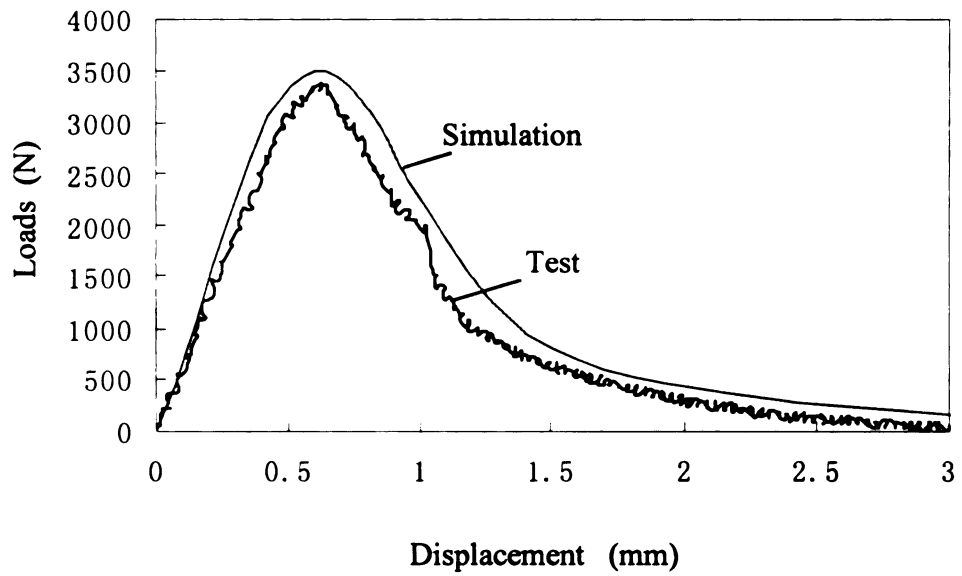

Figure 6.17 Load–displacement curves from test and simulation

6.4 Summary

The nonlinear, explicit, three-dimensional finite element analysis code LS-DYNA was applied to simulate a falling ball impacting a wood-cement particleboard resting on concrete block and a concrete block as well as the multi-stress test on a composite tube.

The agreement between simulation results and experiments indicate that the nonlinear finite element analysis code, LS-DYNA, could be successfully used to simulate impact on wood-cement particleboard. The simulation results also indicated that the LS-DYNA material models MAT_PIECEWISE_LINEAR_PLASTICITY and MAT_PSEUDO_TENSOR can be effectively employed to model wood-cement particle board and concrete, respectively. The simulation result of the multi-stress test indicates that although the WCPB is an orthotropic material, the isotropic plasticity model in LS-DYNA is able to provide very good results.

CHAPTER 7

FINITE ELEMENT SIMULATION OF VEHICLE CRASHING ON CONCRETE BARRIER ENHANCED WITH WCPB

7.1 Introduction

Concrete crash barriers are designed to prevent vehicle passengers from injury and provide certifiable levels of vehicle containment. However, accident data shows that a large number of deaths still occur as a result of vehicles impacting concrete barriers. To improve roadside saftey it may be feasible to install energy absorbing devices to enhance the impact characteristics of existing concrete barriers so as to reduce injury to passengers.

An enhanced barrier should be designed to absorb as much impact energy as possible so as to minimize the deceleration forces on vehicles in the case of vehicle impact and at same time maintain the integrity of the barrier. One approach is to install cushioning material on the side surface of concrete barriers. However, this kind of material should be durable and cost effective. Wood-cement particleboard is durable, cost effective and its use in high volume is favorable to the environment. The potential of using ECPB as cushioning material on concrete crash barriers is investigated in this chapter.

The nonlinear, explicit, three dimensional finite element analysis code LS-DYNA was used to perform crash simulation of vehicle against a concrete barrier enhanced with wood-cement particleboard elements. The impact deceleration force was taken to be the key parameter related to occupant injury. The geometry of WCPB elements that was

attached to the sides of concrete crash barriers were varied to minimize the impact forces on the vehicle so as to reduce the risk of occupant injury during the crash. Three different wood-cement particleboard element geometries were considered: a flat board, a wave shape and bundles of tubes.

7.2 Simulation Test Design and Evaluation Criteria

7.2.1 Concrete barrier

A vertical concrete barrier was selected to conduct crash impact simulations. The compressive strength was taken to be 4000 psi. The barrier had a height of 1066 mm, a width of 190 mm and a length of 5000 mm. The longitudinal reinforcements consisted of six steel bars with a diameter of 15 mm, and the vertical stirrups were made of steel bars with a diameter of 8 mm at a spacing of 400 mm along the barrier's longitudinal direction. Figure 7.1 shows the geometry of the concrete barrier and steel reinforcement.

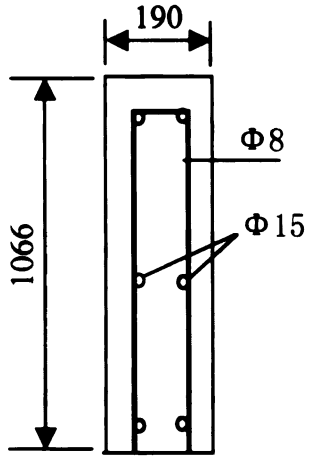

Figure 7.1 Geometry of the concrete barrier and steel reinforcement

7.2.2 Enhanced concrete barrier

The enhanced barrier contains a wood-cement particleboard facade installed on the side surface of the existing concrete barrier where impacts occur. Figure 7.2 shows the enhanced vertical concrete barrier with a flat wood-cement particleboard facade. The enhanced concrete barrier is expected absorb more impact energy and reduce the impact deceleration force on vehicles during impact.

As both wood-cement particleboard and concrete belong to the family of cement-bonded composites, they have compatible properties and can be easily bonded with cement if necessary. However, it is proposed that the wood-cement particleboard facade be fastened using metal fasteners on the side surface of the concrete barriers. This installation will enable facades damaged by vehicle impacts to be replaced easily.

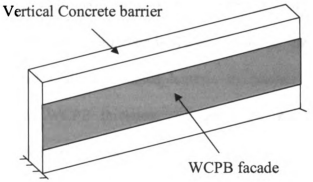

Figure 7.2 Enhanced vertical concrete barrier

Three types of wood-cement particleboard facades were investigated. These consisted of a flat facade, a wave shape and bundled tubes. Figure 7.3 shows the cross the section of particleboard facades.

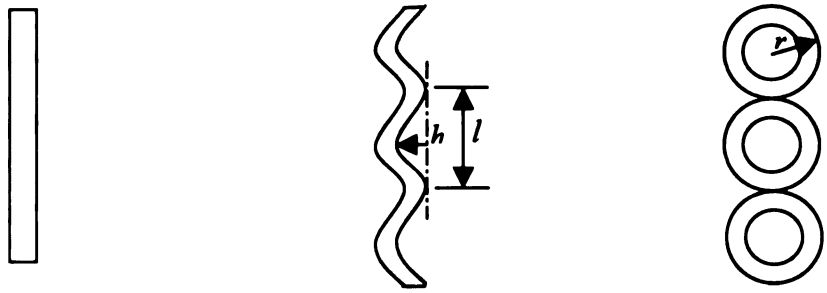

a. Flat b. Wave shape c. Bundled tubes

Figure 7.3 Cross section of particleboard facades

7.2.3 Simulation test matrix

In this study, frontal crash impact simulations were investigated. In order to find a suitable solution for using wood-cement particleboard facades to improve the impact characteristics of the existing concrete barrier, five different WCPB facades were investigated. The vehicle impact speed was 30 mph or 13.4 mm/ms and the total simulation time was set to 100 milliseconds. Table 7.1 shows the simulation matrix for the frontal crash impact studies presented herein. A number of other studies were performed for different WCPB thickness and geometric parameters, and the ones presented here yielded the best results.

Table 7.1 Physical Properties of WCPB Facades

WCPB Shape	Flat	Double wave	Triple wave	Triple-tube bundle	Four-tube bundle
Thickness (mm)	35	35	25	25	25
Geometric parameters (mm)		l=225 h=60	l=225 h=60	r =112	r =76

7.2.4 Evaluation conditions and criteria

The simulation conditions follow the guidelines in the National Car Assessment Program (NCAP) and the National Cooperative Highway Research Program Report 350 (NCHRP350). As NCAP recommends, the safety features of a vehicle were evaluated by a frontal crash on a rigid barrier at a velocity of 30 mph. The crashing vehicle model was the 820C that was recommended by NCHRP350. The 820C model represents a small car with a weight of 820 kg.

The evaluation criteria used in these simulations are based on the acceleration of the vehicle during impact. The immediate causes of injury or death in traffic accidents are numerous, such as broken glass, fire, crushing of the vehicle, hurling of the passenger against the car, etc. However, a primary cause of injury is the acceleration a passenger experiences. The acceleration criteria used in this chapter are recommended in Information About Automobile Accidents (2003) and the Federal Motor Vehicle Safety Standard (FMVSS 214, 2000):

- People can sustain an acceleration of 20*g* without injury.
- People can tolerate accelerations up to 80*g* without serious injury.
- Pelvic acceleration should be less than 130*g* for a survivable injury.

7.3 Finite Element Modeling

The most difficult task in finite element simulation is finite element modeling. The quality of modeling directly affects the accuracy of the results of the finite element simulation. The quality of the modeling depends on many elements, such as software, element modeling, material modeling and so on.

In this simulation study, four commercial software packages were used. LS-DYNA was used for crash analysis, HyperMesh was used as a preprocessor to develop the finite element model, and HyperGraph and LS-POST were used for post-processing.

7.3.1 Element modeling

The wood-cement particleboard and concrete were modeled with solid elements, and the steel reinforcement inside the concrete barrier was modeled with beam elements. The extremities of the beam elements were merged with the nodes of the solid elements. Thus, the reinforcement cannot debond from the concrete. In addition, it was assumed that no frictional sliding occurs between the particleboard and the concrete surface. The corner nodes of the elements for the particleboard were merged with the nodes of the elements for concrete. Figures 7.4 and Figure 7.5 show the element connections. Figure 7.6 shows the mesh for the steel bar inside the concrete barrier.

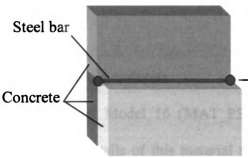

Figure 7.4 Concrete and steel bar elements

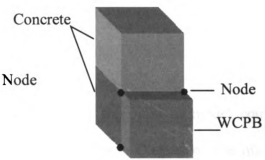

Figure 7.5 WCPB and concrete elements

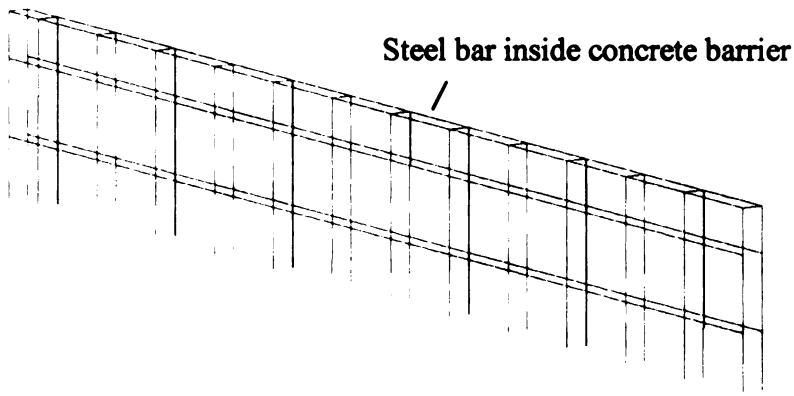

Figure 7.6 Steel reinforcement meshed with beam elements

7.3.2 Material modeling

In nonlinear finite element analysis of vehicle-barrier crashes, the principal challenge is the capability of the material constitutive models to represent a realistic response of the barrier under impact loading. In this study, concrete, wood-cement particleboard and steel bars were modeled with the material models available in LS-DYNA.

7.3.2.1 Modeling concrete

Material Model 16 (MAT_PSEUDO_TENSOR) was used to model concrete material. The details of this material model were described in Chapter 6. The material parameters for the concrete are shown in Table 7.2

Table 7.2 Concrete Material Parameters

Density	2.4 (g/cm3)
Young's Modulus	21526 (MPa)
Poisson's Ratio	0.2
Compressive Strength	20 (MPa)

7.3.2.2 Modeling wood-cement particleboard

Material Model 24 (MAT_PIECEWISE_LINEAR_PLASTICITY) was selected to model the WCPB. As described in Chapter 6, the WCPB was assumed to be an isotropic material, which is an approximation. For elements in tension, failure was controlled with the modulus of rupture (or tensile strength). For elements in compression, the failure was controlled with the compressive strength. All input data for the wood-cement particleboard were exactly the same as the values used in Chapter 6 and are reported in Table 7.3.

Table 7.3 WCPB Material Data

Density	1.044	(g/cm3)
Young's Modulus	400	(MPa)
Poisson's Ratio	0.2	
Yield stress (compressive)	17.2	(MPa)
Tensile cut off (MOR)	11.0	(MPa)

* Young's Modulus is in the direction perpendicular to board thickness.

7.3.2.3 Modeling steel

Steel material is often modeled with elastic, kinematic plastic or piecewise linear plasticity models. Preliminary simulations in this study indicated that the maximum stress in the steel bars inside the concrete barrier was significantly lower than the yield stress. Therefore, Material Model 1 (MAT_ELASTIC) was used to model the steel reinforcement. Material Model 1 (MAT_ELASTIC) is a linear isotropic elastic material model (Hallguist, 1999). The material properties of the steel bar are listed in Table 7.4.

Table 7.4 Steel Bar Material Data

Density	7.85	(g/cm3)
Young's Modulus	210,000	(MPa)
Poisson's Ratio	0.2	
Yield Strength	200	(MPa)

7.3.3 Contact modeling

The contact-surface algorithm in LS-DYNA is a penalty-based method as described in Chapter 6. In vehicle crash simulation, the contact interactions are much more complicated than in the falling ball impact problem modeled in Chapter 6.

In vehicle crash simulations, there are three kinds of contact interactions: vehicle body to barrier surface, vehicle tires to the ground surface, and vehicle self contact (component to component and component self contact due to folding). The contact algorithms were set as follows:

- For the contact interactions between vehicle and barrier surface, set barrier surface as master surface and vehicle surface at impacting side as a slave surface. The nodes on the slave surface cannot penetrate through the master surface. In LS-DYNA, use the Surface to Surface contact type.
- For the contact between vehicle tires and the ground surface, set the ground surface as master surface, and the nodes on the tires as slave nodes. Use the Node to Surface contact type.
- For vehicle self contact, specify that nodes on one component of the vehicle cannot penetrate through any other components of the vehicle. Use the Single Surface (self contact) contact type.

7.3.4 Vehicle model

In this simulation study, a 1975 Honda Civic vehicle model (820C) was selected to conduct crash simulation. The 820C model was released to the public by the National Crash Analysis Center (NCAC). The 820C model has a weight of 820 kg and 5400 elements including shell elements, beam elements and solid elements. This vehicle model was built for frontal crash impact and angle impact. The Federal Highway Administration has approved the model for use in small vehicle traffic crash simulation studies. Figure 7.7 is the finite element model of the vehicle.

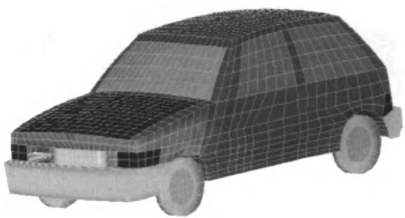

Figure 7.7 Finite element model of the1975 Honda Civic (820C)

7.3.5 Center of gravity of vehicle

In most car vehicles, the center of gravity (CG) of the car is located between the two frontal seats and about 100 to 300 mm above vehicle's floor. In this vehicle model,

its center of gravity is between the two frontal seats and 273 mm above the vehicle's floor or 578 mm above the ground.

In order to record the vehicle's impact response, an accelerometer was mounted at the center of gravity of the vehicle. Accelerations, velocities and displacements of the vehicle were output from the accelerometer. Figure 7.8 shows the location of the center of gravity and accelerometer.

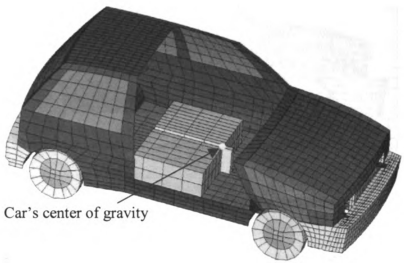

Figure 7.8 CG and accelerometer location

7.3.6 Boundary conditions

Two kinds of boundary conditions were imposed in the crash simulation. One boundary condition is the impact velocity of the vehicle. In this frontal crash impact simulation, the impact velocity of the vehicle was 30 mph or 13.4 mm/ms. The impact velocity was imposed on all nodes of the crash vehicle.

Another boundary condition is the constraint condition imposed on the concrete barrier and the ground. The bottom of the concrete barrier and the ground are fixed. Therefore, all nodes at the bottom of the concrete barrier and on the ground elements were fixed in x, y and z directions. Figure 7.9 shows the boundary condition.

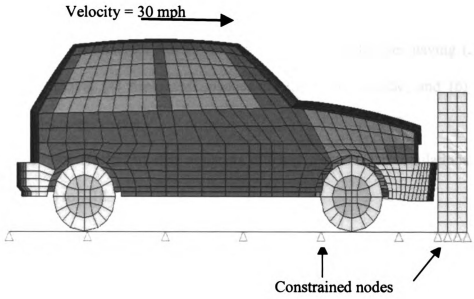

Figure 7.9 Boundary conditions of the FE model

7.4 Finite Element Simulation

As shown in Table 7.1, six different types of frontal vehicle-barrier crash simulations were conducted. In each crash event, the deceleration force on the vehicle during impact is the most important because this correlates with the severity of occupant injuries. To significantly reduce the deceleration force on the vehicle, the wood-cement particleboard elements must dissipate a large amount of impact energy by undergoing large deformations. Concrete barriers enhanced with wood-cement particleboard

elements having different geometric configurations were studied to determine which configuration is most effective in reducing impact forces.

7.4.1 Frontal crash set up

Six different types of frontal crash simulations with different enhanced barriers were conducted using LS-DYNA. These included crash on (1) a plain concrete barrier and crashes on the concrete barrier enhanced with WCPB facades having (2) flat, (3) double-wave shape, (4) triple-wave shape, (5) triple-tube bundle, and (6) four–tube bundle facade, respectively.

The finite element models of the six different frontal crash simulations are shown in Figures 7.10 to 7.15.

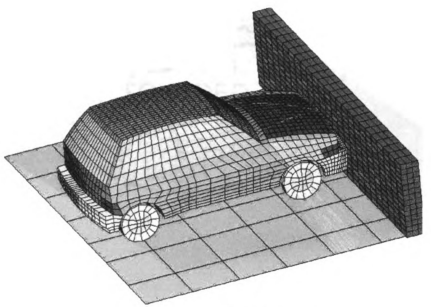

Figure 7.10 Concrete barrier

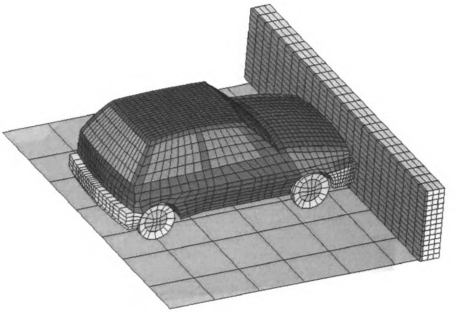

Figure 7.11 Concrete barrier with flat WCPB facade

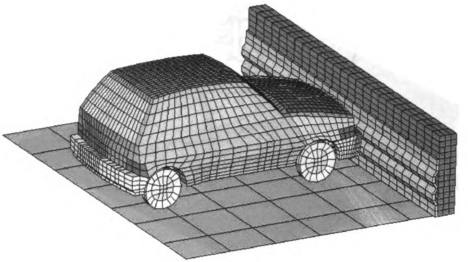

Figure 7.12 Concrete barrier with double-wave WCPB facade

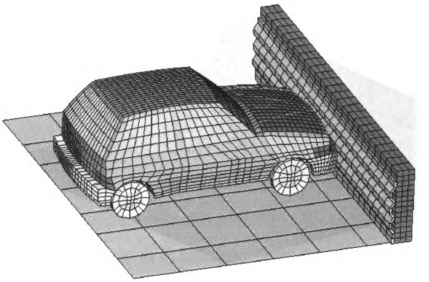

Figure 7.13 Concrete barrier with triple-wave WCPB facade

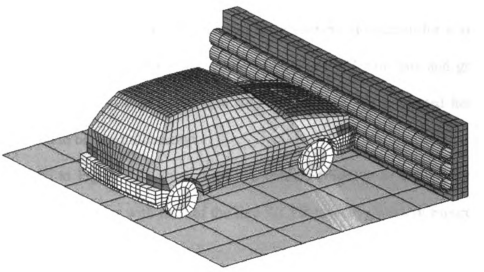

Figure 7.14 Concrete barrier with triple-tube bundle WCPB facade

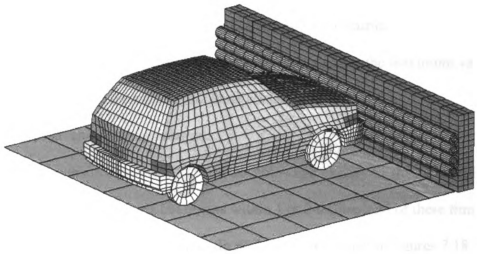

Figure 7.15 Concrete barrier with four-tube bundle WCPB facade

7.4.2 Simulation results

The nonlinear, explicit, three-dimensional finite element simulation for a vehicle barrier crash creates two major types of outputs that include XY pair data and graphic images of vehicle-barrier crash at every time step. For the analysis presented here the time step was taken to be one millisecond.

Figure 7.16 to Figure 7.21 show the 820C vehicle crashing on a plain concrete barrier, and a concrete barrier with each of the five WCPB facades shown in Figure 7.11 to 7.15.

Each figure shows snapshots at five different time steps: t = 0, 10, 30, 70 and 100 (ms). The crash characteristics at each of these time steps are as follows:

t = 0 ms: time step just before the vehicle impact the barrier.

t = 10 ms: time at which the frontal bumper is deformed to its maximum level and just before the vehicle's frontal head contacts with the barrier.

t = 30 ms: time at which the vehicle's deceleration force reaches the maximum value.

t = 70 ms: time at which the vehicle just loses contact with the barrier.

t = 100 ms: time at end of the simulation.

The characteristics described above do not occur exactly at the indicated times (t=10, 30 and 70 ms) for all cases but occurs within 1 or 2 millisecond of these times.

It should be noted that the facades do not appear deformed in Figures 7.18 to 7.21 because the cross section of the facades and barriers shown are outside the impact region.

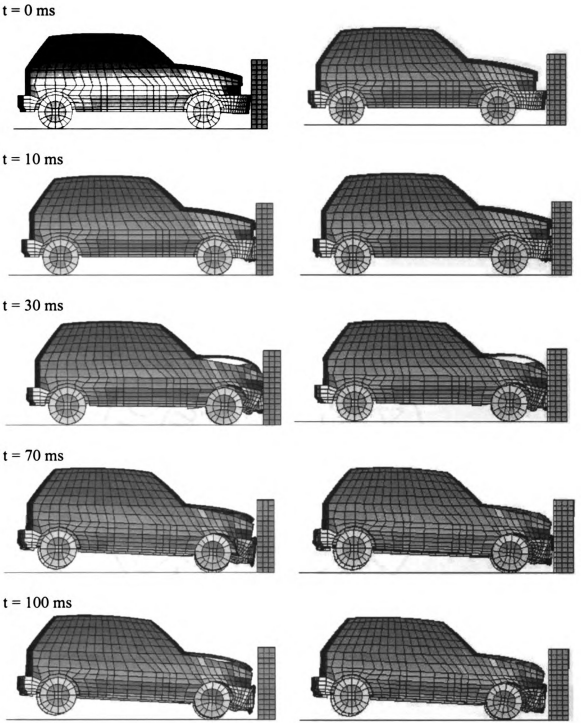

Figure 7.16 Crash on concrete barrier

Figure 7.17 Crash on flat WCPB facade

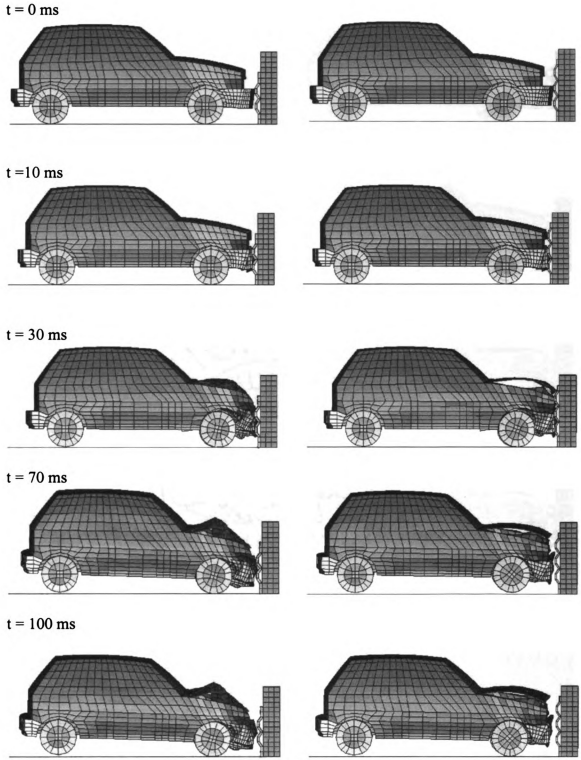

Figure 7.18 Crash on double-wave WCPB facade

Figure 7.19 Crash on triple-wave WCPB facade

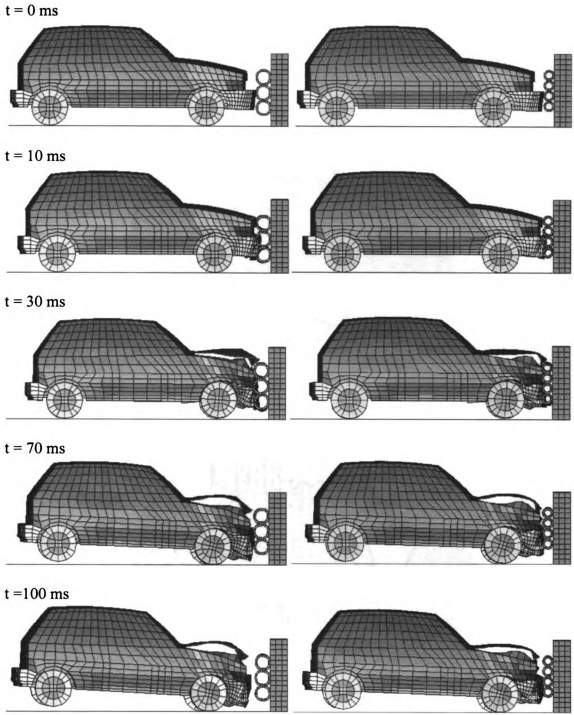

Figure 7.20 Crash on triple-tube WCPB facade

Figure 7.21 Crash on four-tube WCPB facade

Figure 7.22 to Figure 7.27 show the damage on the vehicle at t = 70 ms for impact against different barriers.

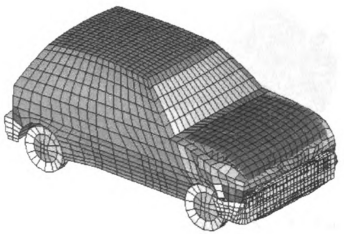

Figure 7.22 Vehicle damage after crash on concrete barrier (at t = 70 ms)

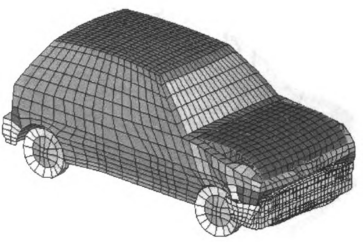

Figure 7.23 Vehicle damage after crash on flat WCPB facade (at t = 70 ms)

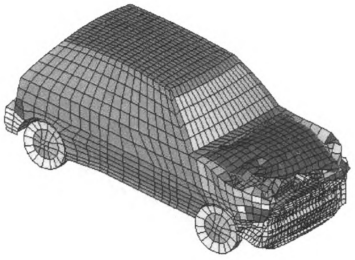

Figure 7.24 Vehicle damage after crash on double-wave WCPB facade (at t = 70 ms)

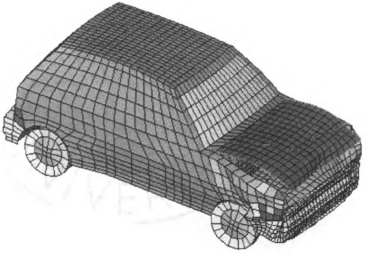

Figure 7.25 Vehicle damage after crash on triple-wave WCPB facade (at 70 ms)

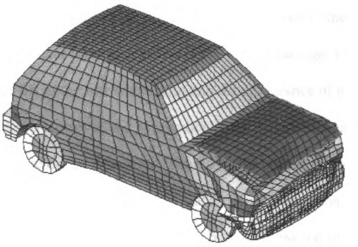

Figure 7.26 Vehicle damage after crash on triple-tube WCPB facade (at t = 70 ms)

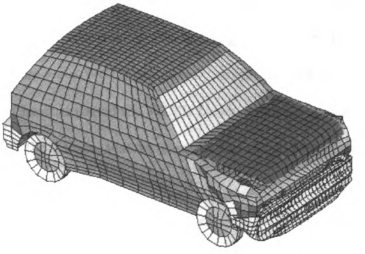

Figure 7.27 Vehicle damage after crash on four-tube WCPB facade (at t = 70 ms)

These figures show the damage to the vehicle for each different crash case. These are two noticeable characteristics in Figure 7.16 to 7.27: one is the upward lift of the vehicle's rear lift; another is the appearance of the vehicle damage. The simulation results show that upward lift of the rear wheel ends and the appearance of external damage vary from one to another. However, the appearance of the external damage is clearly related to the barrier's geometric configuration. The flatter the contact surface of the barrier, the better the vehicle looks after impact. For good energy absorption, the facade's height should cover the height from the bottom of the bumper to the top of the vehicle's frontal head.

The plain concrete barrier and concrete barrier with the flat WCPB façade provide similar damage to the vehicle after impact than the other four types of facades. The appearance of the damaged vehicle was the worst for the concrete barrier enhanced with double-wave WCPB facade (Figure 7.18 and Figure 7.24). This was because the height of the WCPB panel was smaller than the height of the vehicle's frontal head. In Figure 7.18, the double-wave WCPB facade only covers the bumper. The lower part of the vehicle's frontal head impacted the WCPB facade, whereas the upper part impacted the concrete part of the barrier, thereby causing the worst damage appearance to the vehicle's head.

The acceleration, velocity and displacement time histories at the center of gravity of the crashing vehicle for the six different barrier types described in Table 7.1 are shown in Figure 7.28, Figure 7.29 and Figure 7.30, respectively.

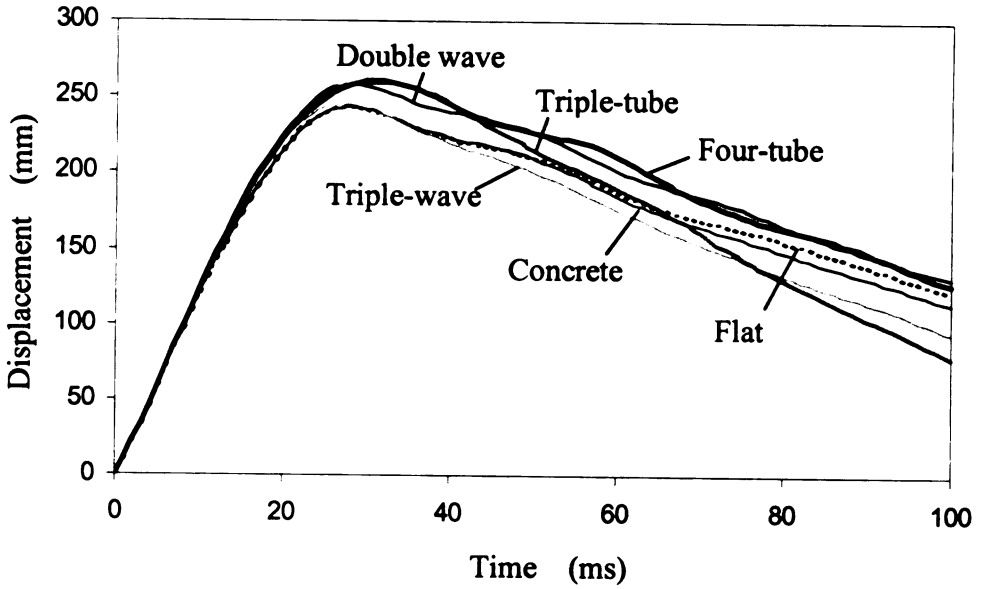

Figure 7.28 Displacement time histories of vehicle

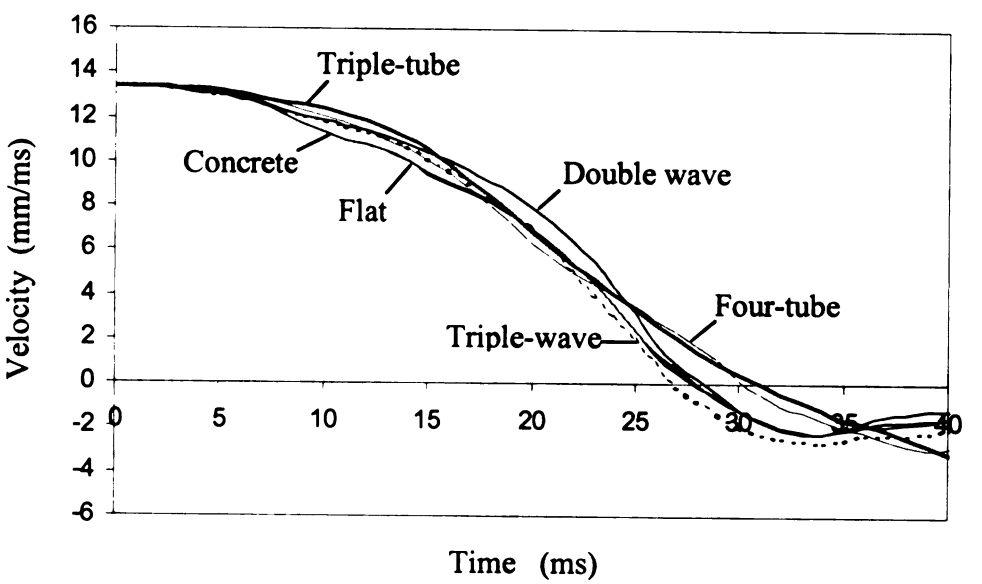

Figure 7.29 Velocity time histories of vehicle

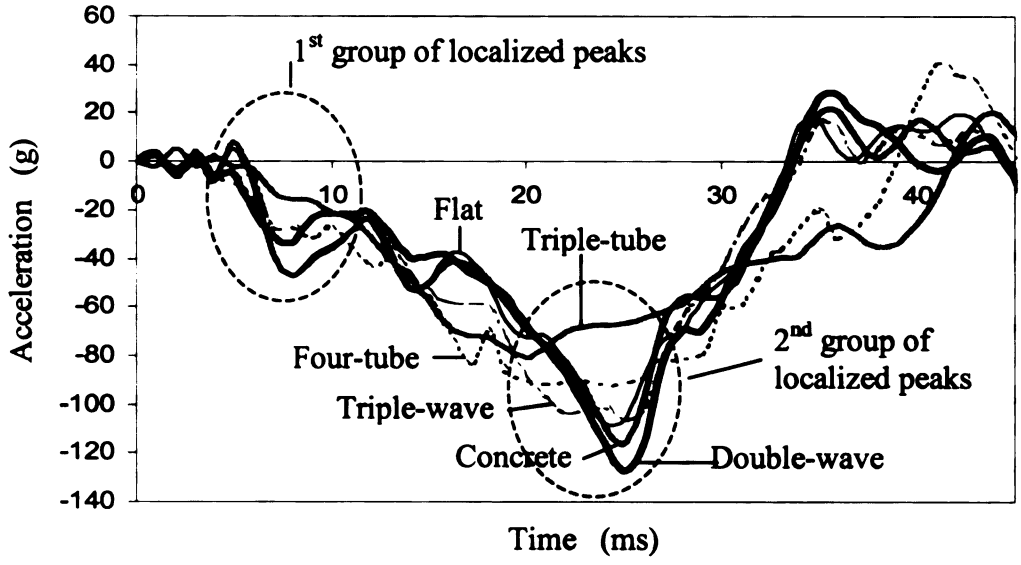

Figure 7.30 Acceleration time histories of vehicle

In Figure 7.28, the largest displacement occurs for impact on the triple-tube and four-tube facades, and the smallest displacement occurs for impact on the plain concrete barrier and the flat WCPB facade. In Figure 7.29, the vehicle impacting the tube facades required more time to reach zero velocity than that in the other four cases. This indicates that the tube facades experienced larger deformation, dissipated more impact energy, and were more effective in moderating the impact forces on the vehicle.

The vehicle decelerations during impact are shown in Figure 7.30. Localized peaks appear in two groups: when the vehicle's bumper contacts the barrier and when the full vehicle head contacts the barrier.

In the first group of localized peaks (between 5 and 10 ms), the deceleration for impact on the concrete barrier reaches the maximum value at a time of about 8.5 milliseconds. The deceleration for impact on the flat WCPB facade is essentially identical to that for impact on the concrete barrier. For the double-wave and triple-wave facades,

the accelerations are essentially identical in the first group of localized peaks, and the maximum values are 70% lower than that for impact on the concrete barrier. For impact on the tube facades, there is no obvious maximum in the first group.

In the second group of localized peaks (between 22 and 26 ms), the maximum decelerations for the flat, triple-wave, four-tube and triple-tube facades were reduced by 7%, 9%, 20% and 30%, respectively, compared to the maximum deceleration for the concrete barriers. For impact on the double-wave facade, however, the maximum deceleration increased by 8% compared to that for impact on the concrete barrier. It is evident that the geometric configuration of the particleboard facade has a significant influence on the energy absorbing behavior of the enhanced barrier. The simulation results show that with a good geometric configuration of the particleboard facade it is possible to reduce the peak deceleration by 30%.

The presence of a bumper on the vehicle makes its impact on the flat WCPB facade somewhat different from the impact of the steel ball studied in Chapter 5. The steel ball was quite rigid and even a flat WCPB facade was able to reduce the maximum deceleration compared to impact on plain concrete. However, in the vehicle the bumper absorbs most of the energy, especially during the early phase of the impact. This is why in the first group of localized peaks, which represents collision of the bumper, the maximum accelerations for impact on the flat WCPB facade and the plain concrete barrier are essentially identical. In the second group of localized peaks, which represent collision of the more rigid frontal head of the vehicle, there is a slight reduction in the maximum deceleration for impact on the flat WCPB facade compared to impact on the

plain concrete barrier. However, the decrease of 7% is still much smaller than the 72% reduction observed for the steel ball in Section 5.2.

The results indicate that the triple-tube facade absorbs the most energy amongst the configurations considered and consequently generates the lowest deceleration forces that the vehicle passengers have to withstand during impact. The triple-tube facade is most effective because it deforms the most as shown in Figure 7.31.

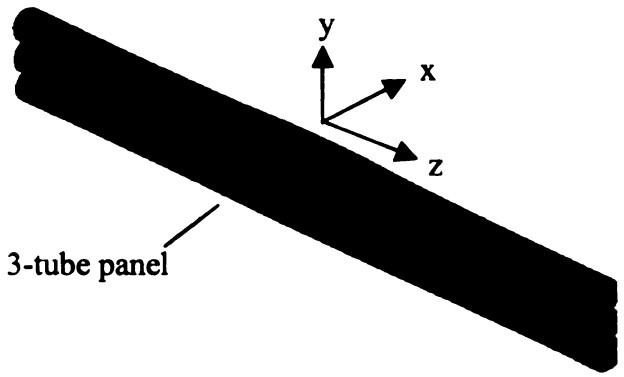

Figure 7.31 Deformation of triple-tube facade after impact

As mentioned in Section 7.2.4, passengers in vehicles can tolerate a maximum acceleration of 80g during impact without serious injury. The deceleration on passengers should be smaller than the deceleration of the vehicle during impact because there is relative movement between the vehicle and passengers. In this simulation, for the vehicle impacting the three-tube facade the deceleration was 80*g* and the passengers inside this vehicle should therefore experience decelerations smaller than 80*g* and not be subjected to serious injury.

7.4.3 Comparison of WCPB, concrete and steel triple-tube facades

To further investigate the contribution of the shape and material of the tube facade in reducing the impact acceleration, crash simulations onto a concrete barrier enhanced with a triple-tube facades made of steel and concrete were conducted. The geometry of the concrete triple-tube facade was the same as that of the WCPB triple-tube facade. For the steel triple-tube facade, two cases were studied with each tube having the same outer diameter as that of the WCPB tube but with thicknesses of 3 mm and 5 mm. Figure 7.32 to Figure 7.35 show the crash images at the largest tube deformation for each case. As evident, in these figures, the WCPB facade has modest deformation (maximum displacement in vehicle moving direction = 32 mm), the concrete tube facade has very little deformation due to its rigidity (maximum displacement in vehicle moving direction = 1.2 mm), and the 3 mm thick steel tubes have very large deformation because of its high flexibility (maximum displacement in vehicle moving direction = 220 mm), and the 5 mm thick steel tubes deform more than the WCPB tubes but less than 3mm thick steel tubes (maximum displacement in vehicle moving direction = 123 mm).

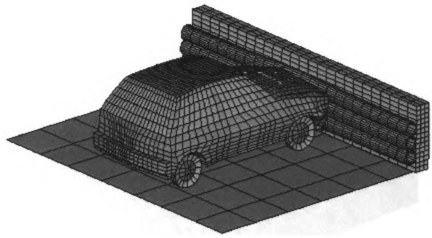

Figure 7.32 Vehicle crashing on WCPB triple-tube facade

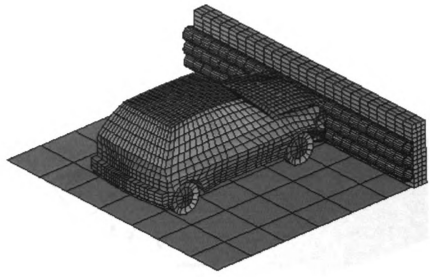

Figure 7.33 Vehicle crashing on concrete triple-tube facade

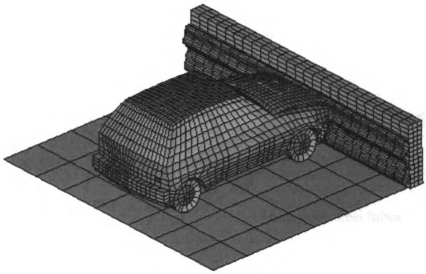

Figure 7.34 Vehicle crashing on 3 mm thick steel triple-tube facade

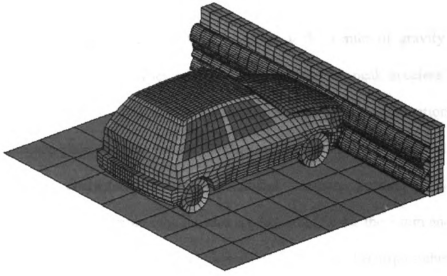

Figure 7.35 Vehicle crashing on 5 mm thick steel triple-tube facade

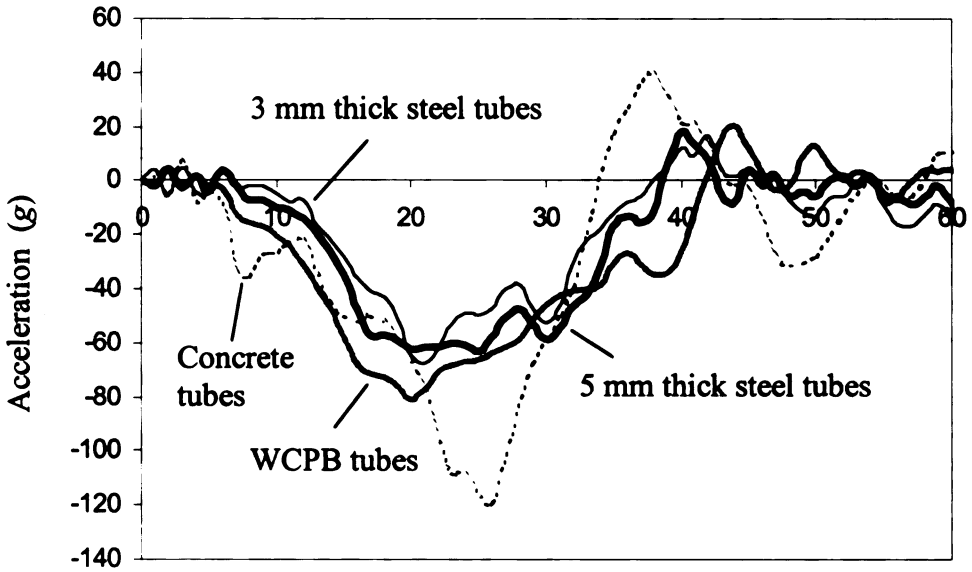

Figure 7.36 Acceleration time histories of vehicle for four triple-tube facades

Figure 7.36 shows the acceleration time histories at the center of gravity of the crashing vehicle for the various types of triple-tube facades, the peak acceleration for concrete triple-tube facade is 120*g*, which is almost the same as the acceleration of the vehicle that impacts a plain concrete barrier. Therefore, the concrete tube facade does not improve the impact characteristics of the modified concrete barrier. The peak accelerations for the two steel triple-tube facades are 65*g* and 68*g* for the 5 mm and 3 mm thicknesses, and are lower than the peak acceleration for the WCPB triple-tube façade (80*g*). While steel performs better than WCPB, the WCPB performs adequately, is cheaper, and its use promotes environmental conservation. Figure 7.36 indicates that both the shape as well as the energy absorption characteristics of the material affect the performance of the facade.

7.5 Summary

Large deformation, dynamic nonlinear finite element analysis was used to evaluate the performance of a concrete barrier enhanced with five different wood-cement particleboard facades subjected to vehicle impact.

The results of the analysis indicate that it is possible to improve the energy absorption capability of a concrete crash barrier by adding appropriately configured wood-cement particleboard facades. The simulation results indicate that the triple-tube facade reduces the deceleration forces on the vehicle the most. For a frontal impact of a Honda Civic vehicle traveling at 30 mph, the triple-tube WCPB facade reduces the vehicle deceleration during impact to 80*g* compared to 120*g* when no facade is used. Occupants of vehicles sustain serious injuries when the deceleration during impact exceeds 80*g*. Therefore, the use of the triple-tube WCPB facade can prevent serious injury to vehicle occupants during a frontal impact at 30 mph.

Comparisons of the performance of WCPB, concrete and steel triple-tube facades indicate that although the steel tubes are most effective in reducing the deceleration forces, the WCPB tubes also perform quite well, while the concrete tubes are ineffective.

CHAPTER 8

CONCLUSIONS

8.1 Introduction

The work reported in this dissertation include a new manufacturing process for making high performance wood-cement particle composites, material characterization of the composites subjected to bending, compression and impact loading, and results of dynamic large deformation nonlinear finite element analysis for simulating impact tests on wood-cement particleboard and simulating a vehicle impacting a concrete barrier enhanced with wood-cement particleboard facades. Background information about wood-cement composites and computational simulation of a vehicle impacting traffic crash barriers also is provided. The most significant findings of this study as well as a discussion of experimental and analytical future research that will advance this research further are summarized in this chapter.

8.2 Development of Wood-Cement Particleboard

8.2.1 Manufacturing process

A new process for manufacturing wood-cement particleboard is presented and consists of pressure control and fully saturated curing to produce high-performance wood-cement particleboard. In particular, the fully saturated curing procedure improves the bonding between the irregular surface of wood particles and the cement matrix. As

a result, the bending strength of wood-cement particleboard reaches 11.7 MPa and is higher than the commonly accepted limit to 10 MPa (Wolfe, 1996).

8.2.2 Effect of cement/wood ratio to bending strength

Bending tests were performed to establish the relationship between bending strength and the cement/wood ratio. The particleboard with a cement/wood ratio of 1.5 yields the maximum bending strength (or modulus of rupture) and may be considered as the optimum cement/wood ratio. The results also indicate that the bending strength of WCPB increases as the cement/wood ratio increases from 1.0 to 1.5 and decreases when the cement/wood ratios increases further from 1.5 to 4.0.

The test results also indicate that the modulus of elasticity and density of the particleboard increases almost linearly as the cement/wood ratio increases.

The toughness index of 6.0 achieved from bending tests indicates that the wood-cement particleboard has a higher energy dissipation capacity compared to steel fiber reinforced concrete which has a toughness index of 5.0. Therefore, the wood–cement particleboard can be used when energy dissipation is desired.

8.2.3 Compressive properties

The compressive load-deformation curve of WCPB displays significant softening non-linearity indicating that the material has the capability to absorb energy. The material properties of WCPB are not isotropic but have directional dependencies due to the

orientation of the wood particles resulting from pressing during the manufacturing process. Short column specimens failed predominantly in shear under compressive loading irrespective of the orientation of the particles in the columns.

The test results indicated that WCPB with a cement/wood ratio of 1.5 exhibited a compressive strength comparable to that of normal concrete. However, the strain at peak load was ten to fifty times larger than that of normal concrete depending on the direction of the compressive loading. The ability to sustain such large deformations implies that WCPB can be used for applications where energy dissipation is desired.

A WCPB tube was also tested under compressive loading applied along a diameter. The test results indicated that the tube had a large plastic deformation. Under a multi-stress state the wood-cement particleboard can also be modeled as an elasto-plastic material.

8.2.4 Impact characteristics

A falling ball impact test was used to study the impact characteristics of WCPB. The falling ball impact test was performed on a plain concrete block, WCPB resting on the concrete block, and a wood board resting on the concrete block. The time histories of acceleration, velocity and displacement for impact on WCPB are much closer to the corresponding time histories for impact on the wood board rather than for impact on plain concrete. The wood-cement particleboard resting on concrete reduced the maximum impact deceleration force by about 72% compared to the deceleration force for impact on

concrete. The ability of the WCPB to reduce the impact deceleration force by such a large amount suggests that WCPB has a strong potential to dissipate energy.

8.3 Computational Simulations of Impact on Wood-Cement Particleboard

Simulation results indicate that the nonlinear finite element analysis code, LS-DYNA, can be successfully applied to simulate the mechanical tests on wood-cement particleboard. The simulation results agree very well with the results of both the impact test and multi-stress test.

The simulation results also indicate that the LS-DYNA material models could be effectively applied to model the concrete and wood-cement particleboard. The simulation results further indicated that the wood-cement particleboard displays elastic-degrading plastic behavior under a multi-stress state and assuming that the WCPB is an isotropic elasto-plastic material in finite element analysis produces reasonable results even though the real material has directional properties.

Dynamic nonlinear finite element analysis was applied for evaluating the designs of a concrete crash barrier enhanced with wood-cement particleboard facades subjected to vehicle impact. The results of the simulations indicate that it is possible to maximize the energy absorption ability of the system by selecting an appropriate geometric configuration for the wood-cement particleboard facade. The concrete barrier enhanced with triple-tube WCPB facade provides the highest level of crash energy absorption. The

geometry of the concrete barrier enhanced with the triple-tube wood-cement particleboard facade assures controllable deformations and reduces the potential injury to vehicle occupants.

8.4 Future Research

Future research, development, and applications of wood-cement particleboard are necessary in order for enhanced concrete crash barriers with WCPB facade to become a reality. The future works to study include the development of:

- Better protective coating system (fiber-resin coating or resin coating) for WCPB facade to strengthen its durability under freeze-thaw.
- Better material model to accurately characterize the material properties of wood-cement particleboard.
- Optimization of the geometric configuration of wood-cement particleboard facade used to enhance concrete crash barriers.
- Development of connection details for securing the WCPB facade to the concrete barriers.

Because of the complexity of the behavior of concrete barriers enhanced with the triple-tube WCPB facade, a field crash test of a vehicle impacting an enhanced concrete crash barrier is also recommended in the future research.

APPENDICES

APPENDIX A

AN 820C VEHICLE IMPACTING A CONCRETE BARRIER ENHANCED WITH A 3-TUBE WOOD-CEMENT COMPOSITE PANEL

This appendix presents the input file of an 820C vehicle impacting a concrete barrier enhanced with a 3-tube wood-cement particle panel. For simplification, the original 596 pages input file was simplified into current input file. The current input file only presents the major command syntax but eliminating most of the data related to Nodes and Elements. The input file is in keyword format in LS-DYNA Version 960 and generated using HyperMesh Version 5.1 and Text Editor as well.

```
*KEYWORD
*TITLE
820C VEH IMPACT SIMULATION WITH VERTICAL CONCRETE BARRIER ENHANCED
WITH WCPB
$$ HM_OUTPUT_DECK created 18:06:59 12-10-2003 by HyperMesh Version 5.1
$$ Generated using HyperMesh-Ls-dyna Template Version : 5.0-1
*CONTROL_TERMINATION
$$  ENDTIM    ENDCYC     DTMIN    ENDENG    ENDMAS
     100.0         0       0.0       0.0       0.0
*CONTROL_TIMESTEP
$$  DTINIT    TSSFAC      ISDO    TSLIMT     DT2MS      LCTM     ERODE
MSIST
       0.00.89999998         0       0.0  -0.00111         0         1         0
*CONTROL_SHELL
$$  WRPANG    ITRIST     IRNXX    ISTUPD    THEORY       BWC     MITER
PROJ
      45.0         2        -1         0         2         2         1         0
*CONTROL_HOURGLASS
$$       IHQ        QH
         5       0.1
*CONTROL_BULK_VISCOSITY
$$        Q2        Q1
       1.5      0.06
*CONTROL_CONTACT
$$  SLSFAC   RWPNAL    ISLCHK    SHLTHK    PENOPT    THKCHG    ORIEN
ENMASS
       0.1       0.0         2         0         1         0         1
```

```
$$  USRSTR    USRFRC      NSBCS     INTERM      XPENE      SSTHK       ECDT
TIEDPRJ
         0         0          0          0        0.0          0          0          0
*CONTROL_PARALLEL
$$     NCPU    NUMRHS       ACCU
         4         0          1
*CONTROL_COUPLING
$$  UNLENG     UNTIME     UNFORC      TIMIDL      FLIPX      FLIPY      FLIPZ
SUBCYL
       1.0       1.0        0.0        0.0          0          0          0          1
*CONTROL_OUTPUT
$$    NPOPT    NEECHO    NREFUP    IACCOP     OPIFS    IPNINT    IKEDIT
         1         3          0          0        0.0          0        100          0
*CONTROL_ENERGY
$$     HGEN      RWEN     SLNTEN      RYLEN
         2         2          2          2
$$DATABASE_OPTION -- Control Cards for ASCII output
*DATABASE_NODOUT
       1.0
*DATABASE_GLSTAT
       1.0
*DATABASE_MATSUM
       1.0
*DATABASE_RBDOUT
       1.0
*DATABASE_BINARY_D3PLOT
$$ DT/CYCL      LCDT      BEAM      NPLTC
       2.0         0         0          0
*DATABASE_BINARY_D3THDT
$$ DT/CYCL      LCID
       2.0         0
*DATABASE_BINARY_D3DUMP
$$ DT/CYCL
   40000.0
*DATABASE_BINARY_RUNRSF
$$ DT/CYCL
   10000.0
*NODE
       1  671.5082385485 -767.1162518609266.499999970496
      ...
*MAT_ELASTIC
```

```
$HMNAME MATS       1MAT1_1
          11.0120E-07     200.0      0.33       0.0       0.0       0.0
*MAT_ELASTIC
$HMNAME MATS       3MAT1_3
          38.1280E-06     200.0      0.33       0.0       0.0       0.0
*MAT_ELASTIC
$HMNAME MATS       4MAT1_4
          42.2000E-06      80.0      0.33       0.0       0.0       0.0
*MAT_ELASTIC
$HMNAME MATS       5MAT1_5
          52.2000E-06      80.0      0.33       0.0       0.0       0.0
*MAT_ELASTIC
$HMNAME MATS       6MAT1_6
          68.1140E-06     200.0      0.33       0.0       0.0       0.0
*MAT_ELASTIC
$HMNAME MATS       8MAT1_8
          81.8970E-06     200.0      0.33       0.0       0.0       0.0
*MAT_ELASTIC
$HMNAME MATS      20MAT1_20
         207.8600E-06     200.0      0.33       0.0       0.0       0.0
*MAT_ELASTIC
$HMNAME MATS      21MAT1_21
         217.8600E-06     200.0      0.33       0.0       0.0       0.0
*MAT_ELASTIC
$HMNAME MATS      22MAT1_22
         227.8600E-06     200.0      0.33       0.0       0.0       0.0
*MAT_ELASTIC
$HMNAME MATS      24MAT1_24
         241.0120E-07     200.0      0.33       0.0       0.0       0.0
*MAT_ELASTIC
$HMNAME MATS      26MAT1_26
         262.7780E-08     200.0      0.33       0.0       0.0       0.0
*MAT_PLASTIC_KINEMATIC
$HMNAME MATS       2MAT3_2
          27.8600E-06     200.0      0.33     0.207       2.0       0.0
         0.0       0.0       0.0         0
*MAT_PLASTIC_KINEMATIC
$HMNAME MATS       7MAT3_7
          77.8600E-06     200.0      0.33     0.207       2.0       0.0
         0.0       0.0       0.0         0
*MAT_PLASTIC_KINEMATIC
```

```
$HMNAME MATS       9MAT3_9
        93.8000E-07      10.0      0.35     0.0207       0.1       0.0
        0.0       0.0       0.0         0
*MAT_PLASTIC_KINEMATIC
$HMNAME MATS       10MAT3_10
        105.6050E-07     200.0     0.33      0.207       2.0       0.0
        0.0       0.0       0.0         0
*MAT_PLASTIC_KINEMATIC
$HMNAME MATS       11MAT3_11
        117.8600E-06     200.0     0.33      0.207       2.0       0.0
        0.0       0.0       0.0         0
*MAT_PLASTIC_KINEMATIC
$HMNAME MATS       12MAT3_12
        127.8600E-06     200.0     0.33      0.207       2.0       0.0
        0.0       0.0       0.0         0
*MAT_PLASTIC_KINEMATIC
$HMNAME MATS       13MAT3_13
        135.7410E-07      30.0     0.33       0.02      0.03       0.0
        0.0       0.0       0.0         0
*MAT_PLASTIC_KINEMATIC
$HMNAME MATS       14MAT3_14
        147.8600E-06     200.0     0.33      0.207       2.0       0.0
        0.0       0.0       0.0         0
*MAT_PLASTIC_KINEMATIC
$HMNAME MATS       15MAT3_15
        157.8600E-06     200.0     0.33      0.207       2.0       0.0
        0.0       0.0       0.0         0
*MAT_PLASTIC_KINEMATIC
$HMNAME MATS       17MAT3_17
        177.8600E-06     200.0     0.33      0.207       2.0       0.0
        0.0       0.0       0.0         0
*MAT_PLASTIC_KINEMATIC
$HMNAME MATS       18MAT3_18
        187.8600E-06    2000.0     0.33       2.07       2.0       0.0
        0.0       0.0       0.0         0
*MAT_PLASTIC_KINEMATIC
$HMNAME MATS       19MAT3_19
        197.8600E-06     200.0     0.33      0.207       2.0       0.0
        0.0       0.0       0.0         0
*MAT_PLASTIC_KINEMATIC
$HMNAME MATS       23MAT3_23
```

```
        237.8600E-06      200.0       0.33      0.207       2.0         0.0
       0.0         0.0         0.0          0
*MAT_PLASTIC_KINEMATIC
$HMNAME MATS       25MAT3_25
        251.5720E-05      200.0       0.33      0.207       2.0         0.0
       0.0         0.0         0.0          0
*MAT_NULL
$HMNAME MATS       102NULL
        1024.0000E-07                                                  200.0       0.3
*MAT_RIGID
$HMNAME MATS       16MAT20_16
        161.4650E-06      200.0       0.33       0.0         0.0         0.0
       1.0          0           0
       0.0         0.0         0.0         0.0         0.0         0.0
*MAT_PIECEWISE_LINEAR_PLASTICITY
$HMNAME MATS       108board
        1081.0400E-06       0.37        0.3       0.017
                                    0           0
$$ HM Entries in Stress-Strain Curve =          8
    0.0034    0.0068    0.0096    0.0123    0.0146    0.0178    0.0188    0.0142
       0.0      0.01      0.02     0.033     0.0475    0.0808    0.1168     0.151
*MAT_RESULTANT_PLASTICITY
$HMNAME MATS       101MAT_BAR
        1017.8340E-06      200.0       0.33      0.207       0.0
*PART
$HMNAME COMPS          1Part1
$HMCOLOR COMPS          1          1
material type # 1   (elastic)
           1          1          1          0          0          0          0
*PART
$HMNAME COMPS          2Part2
$HMCOLOR COMPS          2          2
material type # 3 (Kinematic/Isotropic elastic-plastic)
           2          2          2          0          0          0          0
*PART
$HMNAME COMPS          3Part3
$HMCOLOR COMPS          3          3
material type # 1   (elastic)
           3          3          3          0          0          0          0
*PART
$HMNAME COMPS          4Part4
```

```
$HMCOLOR COMPS          4         4
material type # 1    (elastic)
          4         4         4         0         0         0         0
*PART
$HMNAME COMPS          5Part5
$HMCOLOR COMPS          5         5
material type # 1    (elastic)
          5         5         5         0         0         0         0
*PART
$HMNAME COMPS          6Part6
$HMCOLOR COMPS          6         6
material type # 1    (elastic)
          6         6         6         0         0         0         0
*PART
$HMNAME COMPS          7Part7
$HMCOLOR COMPS          7         7
material type # 3 (Kinematic/Isotropic elastic-plastic)
          7         7         7         0         0         0         0
*PART
$HMNAME COMPS          8Part8
$HMCOLOR COMPS          8         8
material type # 1    (elastic)
          8         8         8         0         0         0         0
*PART
$HMNAME COMPS          9Part9
$HMCOLOR COMPS          9         9
material type # 3 (Kinematic/Isotropic elastic-plastic)
          9         9         9         0         0         0         0
*PART
$HMNAME COMPS         10Part10
$HMCOLOR COMPS         10        10
material type # 3 (Kinematic/Isotropic elastic-plastic)
         10        10        10         0         0         0         0
*PART
$HMNAME COMPS         11Part11
$HMCOLOR COMPS         11        11
material type # 3 (Kinematic/Isotropic elastic-plastic)
         11        11        11         0         0         0         0
*PART
$HMNAME COMPS         12Part12
$HMCOLOR COMPS         12        12
```

material type # 3 (Kinematic/Isotropic elastic-plastic)

12 12 12 0 0 0 0

*PART

$HMNAME COMPS 13Part13

$HMCOLOR COMPS 13 13

material type # 3 (Kinematic/Isotropic elastic-plastic)

13 13 13 0 0 0 0

*PART

$HMNAME COMPS 14Part14

$HMCOLOR COMPS 14 14

material type # 3 (Kinematic/Isotropic elastic-plastic)

14 14 14 0 0 0 0

*PART

$HMNAME COMPS 15Part15

$HMCOLOR COMPS 15 15

material type # 3 (Kinematic/Isotropic elastic-plastic)

15 15 15 0 0 0 0

*PART

$HMNAME COMPS 16Part16

$HMCOLOR COMPS 16 1

material type # 20 (Rigid)

16 16 16 0 0 0 0

*PART

$HMNAME COMPS 17Part17

$HMCOLOR COMPS 17 1

material type # 3 (Kinematic/Isotropic elastic-plastic)

17 17 17 0 0 0 0

*PART

$HMNAME COMPS 18Part18

$HMCOLOR COMPS 18 2

material type # 3 (Kinematic/Isotropic elastic-plastic)

18 18 18 0 0 0 0

*PART

$HMNAME COMPS 19Part19

$HMCOLOR COMPS 19 3

material type # 3 (Kinematic/Isotropic elastic-plastic)

19 19 19 0 0 0 0

*PART

$HMNAME COMPS 20Part20

$HMCOLOR COMPS 20 4

material type # 1 (elastic)

```
        20          20          20          0          0          0          0
*PART
$HMNAME COMPS       21Part21
$HMCOLOR COMPS      21          5
material type # 1   (elastic)
        21          21          21          0          0          0          0
*PART
$HMNAME COMPS       22Part22
$HMCOLOR COMPS      22          6
material type # 1   (elastic)
        22          22          22          0          0          0          0
*PART
$HMNAME COMPS       23Part23
$HMCOLOR COMPS      23          7
material type # 3 (Kinematic/Isotropic elastic-plastic)
        23          23          23          0          0          0          0
*PART
$HMNAME COMPS       24Part24
$HMCOLOR COMPS      24          8
material type # 1   (elastic)
        24          24          24          0          0          0          0
*PART
$HMNAME COMPS       25Part25
$HMCOLOR COMPS      25          9
material type # 3 (Kinematic/Isotropic elastic-plastic)
        25          25          25          0          0          0          0
*PART
$HMNAME COMPS       26Part26
$HMCOLOR COMPS      26          10
material type # 1   (rigid)
        26          26          16          0          0          0          0
*PART
$HMNAME COMPS       101BAR1
$HMCOLOR COMPS      101         15
bar1
       101         101         101
*PART
$HMNAME COMPS       102BAR2
$HMCOLOR COMPS      102         15
bar2
       102         101         101
```

```
*PART
$HMNAME COMPS       103BAR3
$HMCOLOR COMPS       103         15
bar3
         103         101         101
*PART
$HMNAME COMPS       104BAR4
$HMCOLOR COMPS       104         15
bar4
         104         101         101
*PART
$HMNAME COMPS       105SURF_CROSS
$HMCOLOR COMPS       105          1
Barrier end surface
         105         102         102
*PART
$HMNAME COMPS       106SIDESURF
$HMCOLOR COMPS       106          9
Barrier side surface
         106         102         102
*PART
$HMNAME COMPS       107CONCRETE
$HMCOLOR COMPS       107          1
Concrete barrier
         107         103         103
*PART
$HMNAME COMPS       108board
$HMCOLOR COMPS       108         14
board
         108         103         108
*PART
$HMNAME COMPS       110contact2
$HMCOLOR COMPS       110          4

         110         102         102
*PART
$HMNAME COMPS       112contact1
$HMCOLOR COMPS       112          5

         112         102         102
*SECTION_BEAM
```

```
$HMNAME PROPS        18SectBeam18
        18          1        0.0        2.0        1.0        0.0
      75.0       75.0       71.0       71.0        0.0        0.0
       ...
*SECTION_SHELL
$HMNAME PROPS         2SectShll2
         2          2        0.0          3        0.0        0.0          0
       1.0        1.0        1.0        1.0        0.0
       ...
*SECTION_SOLID
$HMNAME PROPS         1SectSld1
         1          1          4
       ...
*INITIAL_VELOCITY
$HMNAME LOADCOLS          1Velocity
$HMCOLOR LOADCOLS         1          1
         7          0
      13.4        0.0        0.0        0.0        0.0        0.0
$$ Base Accelerations and Angular Velocities
*LOAD_BODY_Z
$HMNAME LOADCOLS          3LoadBody_3
$HMCOLOR LOADCOLS         3          1
         1        0.0          0
*ELEMENT_BEAM
   43317       18        1        8        7
   43318       18        8        9        7        0        0        0        0        0
      ...
*ELEMENT_SHELL_THICKNESS
        9        2      108      111      123      121
              1.54             1.54             1.54             1.54
      ...
*SET_PART_LIST
$HMSET
$HMNAME SETS          1set_part
         1
         1        2        3        4        5        6        7        8
         9       10       11       12       13       14       15       16
        17       18       19       20       21       22       23       24
        25
*SET_PART_LIST
$HMSET
```

```
$HMNAME SETS          2set_part.1
          2
           1         2         3         4         5         6         7         8
           9        10        11        12        13        14        15        16
          17        18        19        20        21        22        23        24
          25
*SET_NODE_LIST
$HMSET
$HMNAME SETS          6Set_6
          6
        4300      4302      4304      4330      4332      4334      4351      4353
        4355      4369      4371      4373      4390      4392      4394      4420
        4422      4424      4450      4452      4454      4471      4473      4475
        4489      4491      4493      4510      4512      4514      4540      4542
        4544      4570      4572      4574      4600      4602      4604      4621
        4623      4625      4642      4644      4646      4660      4662      4664
        4678      4680      4682      4699      4701      4703      4720      4722
        4724      4741      4743      4745
*SET_SEGMENT
$HMNAME CSURFS          6setSegment_6
$HMCOLOR CSURFS          6         6
          6
*CONTACT_NODES_TO_SURFACE
$HMNAME GROUPS          13car_tube
$HMCOLOR GROUPS          13         1
          10         8         4         0

*CONTACT_AUTOMATIC_SINGLE_SURFACE_TITLE
$HMNAME GROUPS          5singlesurface
$HMCOLOR GROUPS          5         2
          5singlesurface
          2                   2                   0         0
       0.15     0.031       0.0       0.0       0.0         0       0.01.0000E+20
        1.0       1.0                             1.0       1.0       1.0       1.0
*RIGIDWALL_PLANAR
$HMNAME GROUPS          6rigid
$HMCOLOR GROUPS          6         12
          6
 452.93851-567.67354        -1.0 452.93851-567.67354         0.0
*BOUNDARY_SPC_NODE
$HMNAME LOADCOLS          2NodalConstraints.1
```

```
$HMCOLOR LOADCOLS          2          5
       5297          0          1          1          1          1          1          1
       ...
*DATABASE_HISTORY_NODE
$HMNAME OUTPUTBLOCKS          1nodeth
   2788110    2788108    2787921    2787919
*DEFINE_CURVE
$HMNAME CURVES          1LoadCurve1
$HMCOLOR CURVES          1          1
$HMCURVE       1       1 LoadCurve1
            1          0        1.0        1.0        0.0        0.0          0
                     0.0                   0.0
                     3.0                0.00981
                   400.0                0.00981
$$          UNSUPPORTED CARDS - STARTS
*MAT_PSEUDO_TENSOR
103        2.4E-06      8.971        0.2
0.02       -1.0         0.0          0.0          0.0          0.0          0.0          0.0
0.0        0.0          0.0



$$          UNSUPPORTED CARDS - ENDS
*END
```

APPENDIX B

A STEEL BALL IMPACTING ON WOOD-CEMENT PARTICLEBOARD OVERLAYING A CONCRETE BLOCK

This appendix presents the input file of a steel ball impacting a wood-cement particleboard overlaying a concrete block. For simplification, the original 477 pages input file was simplified into the current demonstration file. The current file only presents the major command syntax but eliminating most of the data related to Nodes and Elements. The input file is in keyword format in LS-DYNA Version 960 and generated using HyperMesh Version 5.1 and Text Editor as well.

```
*KEYWORD
$$ HM_OUTPUT_DECK created 02:33:56 05-26-2003 by HyperMesh Version 5.1
$$ Generated using HyperMesh-Ls-dyna Template Version : 5. 1
*CONTROL_TERMINATION
$$  ENDTIM    ENDCYC     DTMIN    ENDENG    ENDMAS
      10.0         0       0.0       0.0       0.0
*CONTROL_TIMESTEP
$$  DTINIT    TSSFAC      ISDO    TSLIMT     DT2MS      LCTM
ERODE     MSIST
       0.00.89999998         0       0.0       0.0         0         1         0
*CONTROL_SHELL
$$  WRPANG    ITRIST     IRNXX    ISTUPD    THEORY       BWC     MITER      PROJ
      45.0         2        -1         0         2         2         1         0
*CONTROL_HOURGLASS
$$       IHQ        QH
         5       0.1
*CONTROL_BULK_VISCOSITY
$$        Q2        Q1
       1.5      0.06
*CONTROL_CONTACT
$$  SLSFAC    RWPNAL    ISLCHK    SHLTHK    PENOPT    THKCHG    ORIEN
ENMASS
       0.1       0.0         2         0         1         0         1
$$  USRSTR    USRFRC     NSBCS    INTERM     XPENE     SSTHK      ECDT
TIEDPRJ
```

```
         0         0         0         0       0.0         0         0         0
*CONTROL_PARALLEL
$$     NCPU     NUMRHS       ACCU
         4         0         1
*CONTROL_COUPLING
$$  UNLENG    UNTIME    UNFORC    TIMIDL     FLIPX     FLIPY     FLIPZ
SUBCYL
       1.0       1.0       0.0       0.0         0         0         0         1
*CONTROL_OUTPUT
$$    NPOPT    NEECHO    NREFUP    IACCOP     OPIFS    IPNINT    IKEDIT
         1         3         0         0       0.0         0       100         0
*CONTROL_ENERGY
$$      HGEN      RWEN    SLNTEN      RYLEN
         2         2         2         2
$$DATABASE_OPTION -- Control Cards for ASCII output
*DATABASE_NODOUT
       0.02
*DATABASE_GLSTAT
       0.02
*DATABASE_MATSUM
       0.02
*DATABASE_RBDOUT
       0.02
*DATABASE_BINARY_D3PLOT
$$ DT/CYCL      LCDT      BEAM      NPLTC
       1.0         0         0         0
*DATABASE_BINARY_D3THDT
$$ DT/CYCL      LCID
       2.0         0
*DATABASE_BINARY_D3DUMP
$$ DT/CYCL
   40000.0
*DATABASE_BINARY_RUNRSF
$$ DT/CYCL
   10000.0
*NODE
       23.2759301877E-15            -53.5           -0.503
       ...
*MAT_PLASTIC_KINEMATIC
$HMNAME MATS       1sphere
         17.9000E-06     210.0      0.28     0.351       3.4       0.0
```

```
        0.0         0.0         0.0
*MAT_NULL
$HMNAME MATS        3Null
          38.4000E-07                                                  200.0         0.3
*MAT_PIECEWISE_LINEAR_PLASTICITY
$HMNAME MATS        2board
          21.0400E-06       0.37        0.3       0.017
                                  1           0
$$ HM Entries in Stress-Strain Curve =            0


*PART
$HMNAME COMPS       1sphere
$HMCOLOR COMPS       1          4

          1           1           1
*PART
$HMNAME COMPS       2board
$HMCOLOR COMPS       2          2

          2           2           2
*PART
$HMNAME COMPS       3concrete
$HMCOLOR COMPS       3          8

          3           3           4
*PART
$HMNAME COMPS       4sphere_face
$HMCOLOR COMPS       4          9

          4           4           3
*PART
$HMNAME COMPS       5board_face
$HMCOLOR COMPS       5          7

          5           5           3
*SECTION_SHELL
$HMNAME PROPS       4sphere_face
          4           2       0.833           2         0.0         0.0           0
        0.1         0.1         0.1         0.1         0.0
$HMNAME PROPS       5board_face
```

```
         5          2      0.833          2        0.0        0.0          0
       0.1        0.1        0.1        0.1        0.0
*SECTION_SOLID
$HMNAME PROPS        1sphere
         1          1          4
$HMNAME PROPS        2board
         2          1          4
$HMNAME PROPS        3concrete
         3          1          4
*ELEMENT_SHELL
   11586          4       2375       2373       2374       2374
   11585          4       2222       2262       2263       2263
   11584          4       2254       2221       2255       2255
   11583          4       2095       2092       2118       2118
*ELEMENT_SHELL
   11978          4       2288       2306       2295       2278
   11977          4       2282       2275       2294       2297
   ...
*ELEMENT_SOLID
    1420          1       1359        165        172        207        207        207        207        207
    1476          1       1401        356        315        357        357        357        357        357
    ...
*CONTACT_AUTOMATIC_SURFACE_TO_SURFACE
$HMNAME GROUPS        1surftosurf
$HMCOLOR GROUPS        1          1
         4          5          3          3          0          0
       0.0        0.0        0.0        0.0        0.0          0        0.01.0000E+20
       1.0        1.0                              1.0        1.0        1.0        1.0
*BOUNDARY_SPC_NODE
$HMNAME LOADCOLS        1spc
$HMCOLOR LOADCOLS        1         14
       8462          0          1          1          1          1          1          1
*INITIAL_VELOCITY_NODE
$HMNAME LOADCOLS        2velocity
$HMCOLOR LOADCOLS        2         10
       2699        0.0        0.0      -1.72
       2698        0.0        0.0      -1.72
       ...
*DATABASE_HISTORY_NODE
$HMNAME OUTPUTBLOCKS        1NOUT
        399        558       2295
```

```
*DEFINE_CURVE
$HMNAME CURVES         1curve1
$HMCOLOR CURVES        1        1
$HMCURVE      1     0 curve1
          1          0        1.0        1.0        0.0        0.0          0
                   0.0                 0.0034
                0.0102                 0.0067
                0.0206                 0.0095
          ......
$$          UNSUPPORTED CARDS - STARTS
*MAT_PSEUDO_TENSOR
4          2.4E-06     8.971      0.2
0.02       -1.0        0.0        0.0        0.0        0.0        0.0        0.0
0.0        0.0         0.0
$$          UNSUPPORTED CARDS - ENDS
*END
```

BIBLIOGRAPHY

BIBLIOGRAPH

Altair Engineering Inc. 1999. HyperMesh User Manual.

Altair Engineering Inc. 1999. HyperGraphics Usser Mannual.

American National Standards, Particleboard, 1993.

American Society for Testing and Materials, ASTM D 1037-78, 1996, Standard method of evaluating the properties of wood-based fiber and particle panel materials.

Balaguru, P. N. and Shah, S. P., 1992, "Fiber-Reinforced Cement Composites", McGraw-Hill, Inc.

Bathe, K., 1996, "Finite Element Procedures", Prentice-Hall, Inc.

Bison-Werke Bahre and Greten GMBH & Co. KG, 1977, "Cement-bonded particleboard plant integrated with low-cost housing production unit".

Blankenhor, P.R. 1994, "Compressive strength of hardwood-cement composites", Forest Products Journal, Vol. 44, No. 4, pp. 59-62.

Bligh, Roger, 2002. "Project shows predictive use of computer simulation." Texas Transportation Researcher.

Bodig, Jozsef and Jayne, B. A. 1982, "Mechanics of Wood and Wood Composites", Van Nostrand Reinhold Company Inc. New York, N.Y.

Bresler, B. and Pister, K.S., 1958. "Strength of Concrete under Combined Stresses." Journal of the American Concrete Institute, 55(20), 321-345.

CETRIS, 2005, Web publication at http: //www.cetris.com.

Chen, W. F. and Saleeb, A. F., 1982, "Constitutive Equations for Engineering Materials: Volume 1, Elasticity and Modeling", John Wiley & Son, Inc.

Chen, W. F., and Han, D. J., "Part IV: Concrete Plasticity." Plasticity for Structural Engineers. New York: Springer-Verlag New York Inc.

Cook, R. D., Malkus, D. S. and Plesha, M. E., 1989. "Concept and Applications of Finite Element Analysis". Third edition, John Wiley & Sons, Inc.

Cooper, P.A. 1994. "Disposal of treated wood removed from service: The issues in environmental considerations in manufacture, use, and disposal of preservative-treated wood," Forest Products Society(Madison, Wisconsin), pp. 85-90.

Coutts, R.S.P.,1986 "Sticks and Stones", Forest Products Newsletter, CSIRO Division of Chemical and Wood Technology (Australia), Vol.2, No.1, January, pp. 1-4 D1037-78.

Desai, C. S. and Siriwardane, H. J., 1984, "Constitutive Laws for Engineering Materials with Emphasis on Geologic Materials", Prentice Hall, Inc. New Jersey.

Dinwoodies, J.H. et al, 1991 "The long-term performance of cement bonded particleboard" Proceedings of inorganic bonded wood and fiber composite materials. Forest Product Society, Madison, Wisconsin.

Drucker, D. C. and W. Prager, 1952, Soil Mechanics and Plastic Analysis of Limit Design, Quart. Applied Mathematics, Vol.10, No.2, pp. 157-165.

Du Bois, Paul A., 1999, "Crashworthiness Engineering Course Notes."

Eltomation Web Publication, http: //www. eltomation.nl.

Environmental Building News, 1997, "Disposal: The Achilles' Heel of CCA-Treated Wood", Vol. 6, No.3, March.

Environmental Building News, 1998, "Wood-Chip And Cement Wall Form", Vol. 7, No. 3, March.

Environmental Building News. 1992. "Wood-fiber Cement Blocks", Vol. 1, No. 3.

Fact Sheet, 2002, "Wood: A strategy for Developing Recycling Market in Ireland", Environmental Protection Agency, Ireland.

Falk, R. H., 1994, "Housing Products From Recycled Wood", Proceedings of the First International Conference of CIB TG 16, Nov. 6-9, Tampa, Florida, USA.

Federal Motor Vehicle Safety Standards (FMVSS), 2000, No. 214. USA.

Ferguson, P. M.; Breen, J. E. and Jirsa, J. O., 1988, "Reinforced Concrete Fundamentals", Fifth edition, John Wiley & Son, Inc.

Fuwape, Joeseph Adeola, 1995,"The effect of wood/cement ratio on the strength properties of cement-bonded particleboard from spruce", Journal of Tropical Forest Products.

Gertjansen, R.O., et al. 1988. "Assessment of preservative-treated aspen waferboard after 5 years of field exposure. Forest Products Journal, 39(4).

Hallguist, John O., 1999, LS-DYNA Theoretical Manual, Livermore Software Technology Corporation.

Hallguist, John O., 1999, LS-DYNA User Manual, Livermore Software Technology Corporation.

Hallquist, J. O. and Benson, D. J., 1989, "DYNA3D – Explicit Finite Element Program for Impact Calculations", Proceedings of symposium of Crashworthiness and Occupant Protection in Transportation Systems, ASME Annual Meeting, AMD Vol. 106.

Haygreen, J.G. and Bowyer J.L., 1989, Forest Products and Wood Science, an Introduction, Second Edition, Iowa State University Press /AMES.

Health Canada, 2003, "Fact Sheet on Chromated Copper Arsenate (CCA) Treated Wood".

Hsieh, S.S., E.C. Ting and W.F. Chen. "A plasticity-Fracture Model for Concrete." International Journal of Solids and Structures, 18(3), 181-197.

Hsu, W.E. 1994, "Cement-bonded particleboard from recycled CCA-treated and virgin wood", Proceedings of Inorganic-Bonded Wood and Fiber Composites Materials, University of Idaho, Moscow, Idaho, 4: 49-56. John Wiley & Sons, Inc. http://www.nbc10.com/money/2197698/detail.html.

HyperMesh. 2000. Finite Element Analysis Software, Altair Engineering Inc. Version 5.1.

HyperGraphics. 2000. Data Processing Software, Altair Engineering Inc. Version 5.1.

Information about automobile accidents, 2003. http://www.physics.ubc.ca/~outreach/phys420/p420_96/danny.

Johnson, J. P., and Skynar, M., 1989, "Automotive Crash Analysis Using the Explicit Integration Finite Element Method", Proceedings of symposium of Crashworthiness and Occupant Protection in transportation Systems, ASME Annual Meeting, AMD Vol. 106.

Karam, G.N. et al, 1992, "Evaluation of commercial wood-cement composites for sandwich-panel facing," J. of Materials in Commercial Engineering 6(1).

Kupfer, H., Hilsdorf, H. K. and Rusch, H.,1969. "Behavior of concrete under biaxial stresses." ACI *Journal* 66(8).

Kurfiel, Fred and Moslemi, A.A., 1995, "Wood panel makers consider cement-fiber to boost profits", Sept. Wood Technology.

Laws, V., 1983, "On the mixture rule for strength of fiber reinforced cements," Journal of Material Science Letters, 2, , pp. 527-531.

Lee, W.C., 1985, "Effect of cement/wood ratio on bending properties of cement-bonded southern pine excelsior board," Wood and Fiber Science, 17(3), pp. 361-364.

Little, R. W., 1999, "Elasticity." Dover Publications, Inc., Mineola, New York.

Livermore Software Technology Corporation (LSTC). 2002. LS-POST User manual.

LS-DYNA Version: 960. 2000. Finite element analysis software. Livermore Software Technology Corporation.

LS-POST. 2000. Data processing software. Livermore Software Technology Corporation.

Mackerle, J., 2003. "Finite Element Crash Simulations and Impact-Induced Injuries: An addendum. A Bibliography (1998-2002)." The Shock and Vibration Digest, July.

Marer, P.J. and Grimes, M. 1992. Wood Preservation. University of California Statewide integrated pest management project. Division of Agriculture and Natural Res. Pub. 3335.

Marra, G. G. 1972, "The future of engineered wood materials." Quest 9(4): 1-8.

McDevitt, C. F., 2003, "Basics of Concrete barriers." http://www.tfhtc.gov/pubrds/marpr00/concrete.htm.

Mehta, P. Kumar and Monteiro, Paula J. M., 1986, "Concrete: structure, properties and materials", second edition, Prentice Hall, Inc. New Jersey.

Micklewright, J. T. 1993. Wood Preserveation Statistics, 1991. American Preserver's Association. Woodstock, MD.

Miller, D.P., 1987, "Wood-cement composites: Interactions of wood components with Portland cement", Doctoral Dissertation, University of Idaho.

Milligan, Ann, 2004, "Cement and wood-wool combine to improve Philippine housing", Partners in Research for Development, No. 14. Australia.

Moslemi, A.A. and Hamel, M.P. 1989, "Fiber and particleboards bonded with inorganic binders", Forest Products Research Society, Madison, WI.

Moslemi, A.A. and Pfister, S.C. 1987, "The influence of cement/wood ratio and cement type on bending strength and dimensional stability of wood-cement composite panel", Wood and Fiber Science, 19(2), pp. 165-175.

Moslemi, A.A., 1974, Particleboard Volume 2. Southern Illinois University Press, Carbondale IL.

NBC newsletter, 2003, "CCA Pressure-Treated Wood",

NCHRP Report 350: Recommended Procedures for safety Performance Evaluation of Highway Features. TRB, National Research Council, Washington. D.C. 1993.

Neithalath, N., Weiss, J. and Olek, J., 2003. "Acoustic Performance and Damping Behavior of Cellulose-Cement Composites." from 1284 School of Civil Engineering, Purdue University.

Nilson, H., 1991, "Design of Concrete Structures," 11th edition, McGraw-Hill Inc.

RBAC Newsletter, 2002. "Recycling Woods: Value-Added Opportunities for Recycled Wood". Recycling Business Assistance Center, A cooperative effort of the N. C. Department of Environment and Natural Resources and the N. C. Department of Commerce. Summer.

Nilsson, Larsgunnar, et al, 1998, "Simulation of truck and car impacting a roadside barrier," Proceedings of 5th LS-DYNA International Conference.

Ottosen, N.S. 1977. "A failure criterion of concrete." ASCE Journal of Engineering Mechanics. 103 (EM4), pp. 527-535.

Oyagade, A.O. 1990, "Effect of cement/wood ratio on the relationship between cement bonded particleboard density and bending properties", Journal of Tropical Forest Science 2(2), pp. 211-219.

Personal email communication with Dr. Len Shewer, 2002, "Algorithm of generating concrete bulk modulus in LS-DYNA."

Plaxcico, C.A., 1997, "Simulation of a vehicle impacting a modified thrie-beam guardrail". Transportation Research Record 1599.

Prestemon, D.R. 1976, "Preliminary evaluation of a wood-cement composite." Forest Products Journal, Vol. 26, No.2.

Reddy, J. N., 1993. "An Introduction of the finite element method." Second edition, McGraw-Hill, Inc.

Roadside Hazards, 2001, Insurance Institute for Highway Safety.

Sarja, A., 1988, "Wood fiber reinforced concrete", Natural Fiber Reinforced Cement and Concrete, Edited by R.N. Swamy, blackie and Sons Publication, pp. 63-91.

Schmidt, R. 1994, "Increased wood-cement compatibility of chromate-treated wood." Forest Products Journal, 44(7/8): 44-46.

Schwer, Len, 2001, "Laboratory Tests for Characterizing Geo-materials", Lecture notes for Geomaterials subjected to impact loads.

Schwer, Len, 2002, Personal email communication.

Shojaati, M., 2003. "Correlation between injury risk and impact severity index ASI." Swiss Transportation Research Conference.

Simatupang, M.H., 1990. "Properties and durability of rapid curing cement-bonded particleboard, Manufactured by addition of carbonation," Proceeding 2nd International Symposium on Vegetable Plants and Their Fibers as Building Materials, Sept. Salvator, Bahia, Brazil. pp. 239-247.

Sorfa, P. 1984, "Properties of wood-cement composites." Journal of Applied Polymer Science, Applied Polymer Sym. 40, pp. 209-216.

Stalker, I. N. 1993. Disposal of treated wood after service. Proceeding CWPA: 159-174.

Suzuki, K. 1993. "Field evaluation of composite products, six years in service. In: Protection of wood-based composite products." Forest Products Society (Madison, Wisconsin).

Tasuji, M.E., Slate, F.O., Nilsion, A.H., 1978, "Stress-strain response and fracture of concrete in biaxial loading," ACI Journal, Vol. 75, 306-312.

U.S. Consumer Products Safety Commission (COSC), 2002, Qestions and Answers about CCA-Treated Wood, http://www.cpsc.gov/.

Venta, George J., 1997, "Gypsum fiberboard: a high performance specialty board." Proceedings of inorganic bonded wood and fiber composite materials. Forest Product Society.

Vesenjak, M and Ren, Z., 2003. "Improving the Road Safety with Computational Simulations". 4th European LS-DYNA Users Conference.

Vick, C.B., R. C. DeGreoot and J. Yongquist. 1990. "Compatibility of nonacidic waterbone preservatives with phenol-formaldehyde adhesive. Forest Products Journal, 40 (2).

Willam, K.J., and E.P. Warnke. 1975. "Constitutive Model for the triaxial Behavior of Concrete." IABSE19. Proceedings of the IABSE Seminar on Concrete Structure Subjected to Triaxial Stresses, Bergamo, Italy, May, IABSE.

Wolfe, Ronald W., 1997, "The use of recycled wood and paper in building applications," Proceedings No.7286, Forest Products Society.

Wolfe, Ronald W., 1999, "Durability and strength of cement bonded wood particle composites made from construction waste," Forest Products Journal, 49(2):24-31.

Won, Jong-Pil, 1995. "Accelerated processing of high performance wood cement composites", Doctoral dissertation, Michigan State University

Yonten, Karma, et al, 2002, "An evaluation of constitutive models of concrete in LS-DYNA finite element code," 15th ASCE Mechanics Conference.

Zaouk, Abdullatif K, et al, 1995, "Evaluation of a multipurpose pickup truck model using full-scale crash data with application to highway barrier impacts," FHWA/NHTSA National Crash Analysis Center Report.

Zhou, Y. and Kamdem, D.P. 2001. "Effect of cement/wood ratio on the properties of cement-bonded particleboard using CCA-treated wood removed from service." Forest Products Journa.